MID INFRARED CHIROPTICAL SPECTROSCOPY IN CHIRAL PLASMONIC METAMATERIALS

Oriol Roig Vilaseca

Submitted in fulfilment of the requirements for the

MSc by Research, MSc (Res)

1st Supervisor: Prof. Malcolm Kadodwala

2nd supervisor: Prof. Adrian Lapthorn

School of Chemistry

College of Science and Engineering

University of Glasgow

31st of May 2021

CONTENTS

ACKNOWLEDGMENTS

This work wouldn´t have been possible without the immense help and support of Professor Malcolm Kadodwala. As my supervisor, he has provided me with the counsel and advice whenever needed, and for that I am grateful.

I have to specially mention as well Dr. Affar Karimullah. He has been crucial in all referred to fabrication and simulation parts in my work, as well as being constantly somebody I could rely on.

Then, I would like to thank all the members of Prof. Kadodwala group, former and today's. Dr Calum Jack, Dr Ryan Tullius, Marion Rodier, Katie McKay, Dr Christopher Kelly, Cameron Gilroy, Mariona Hernández, Esther Argüelles, Martin Kartau, and all other people involved in this project.

I am grateful as well to Professor Adrian Lapthorn, for his continuous advice during all this process. This applies as well to all the staff at the School of Chemistry of the university of Glasgow.

Special thanks to the staff and technicians at the James Watt Nanofabrication Centre. Their advice has been of utmost importance when doing my fabrication there of the nano and microstructures used.

Finally, I want to appreciate the important help that has been Dr. Mario Jiménez, from Prof. Klass Wynne group. Without him, and the entire group as a whole all the work with the FTIR would not had been possible. They helped me in better understanding the functioning and resultant spectra taken by this spectrometer.

Living abroad during nearly four years is not an easy thing, so I am grateful to everyone that helped me during this time: friends and colleagues that I met during my life in Glasgow. To all of them, many thanks.

I cannot finish without thanking the unconditional support I received by my family.

AUTHOR'S DECLARATION

I declare that, except where explicit reference is made to the contribution of others, this work is the result of my own work and has not been submitted for any other degree at the University of Glasgow, or any other institution.

Oriol Roig Vilaseca

May 2021

THESIS OVERVIEW

This work is constituted in four chapters.

On the first one, all the relevant theory is explained; this is the theory on which all the experimental work explained in the other three chapters is based on. It covers the concepts of chirality, plasmons and plasmonics or metamaterials. Another big theory topic covered is the explanation of symmetry, a concept that will be crucial in the last chapter of results. When talking about symmetry, we discuss the term in its broader sense, but also we enter the specificities of it, such as discussing point groups or operations of symmetry that can be applied to molecules or objects. To be more specific, we will discuss how these terms can be applied to the structures we work within the two last chapters: shuriken shapes.

The second and third chapters explain in a detailed way the fabrication of the microstructures used and the experimental set up for the last chapter, which present the obtained results.

The second chapter then explains in a very detailed way the whole fabrication process, how we start by creating the design and preparing the substrate and end by having the lithographed structures. There are also considered the factors that affect this fabrication and comments and analysis on the final structures.

The third chapter is dedicated to the experimental set up for the experiments done in the last chapters. Explanation of the spectrometer used, how it operates, and how we managed the sample to obtain the results are all included there.

Finally, the most important set of results are found in the fourth chapter. This is presented as a paper we wrote regarding the experimental results explained there. When doing the experiments, we found that the plasmonic peak we were working with was shifting with the incident angle of light, and we saw how a splitting appeared with it. We explored this further, and we ran computer simulations (using COMSOL software) to confirm the results. We experimented with cysteine to see how the shifting and an appearing dip, caused by the coupling between bright and dark modes, behave with the biomolecule adsorbed on the gold substrate. All the experiments and simulations are to be found there and an explanation for the results we found. After this chapter, there are the Appendices related to the results presented.

ABSTRACT

The present work explores plasmonic phenomena. It does so in the region of the mid infra – red light. We will explore how light interacts with matter, specifically with gold. This metal, due to its unique properties, allows a plasmonic resonance to arise, which can couple afterwards with the characteristic resonances of a biomolecule. In the case exposed here, this biomolecule will be the aminoacid cysteine.

The resonances that arise from the metal structures due to their interaction with light are referred to as being the 'bright' and 'dark' modes. When these two modes couple, we have an appearing dip, increasing in prominence with shifting angle of light incidence. Afterwards, when placing an adsorbed biomolecule, cysteine in the case exposed here, on top of this gold structure this modes couple with the amide resonance of cysteine, causing a shift in the spectra from the structure, comparable to the spectra of the structure without the aminoacid adsorbed.

After explaining the fundamental theory, we will explain the fabrication and experimental procedures. Regarding the fabrication, we focus on how we fabricated several different structures until we found the one that worked best for our purposes: the 1 μm structure. This size refers to the length arm-to-arm of the designed structure, a shuriken-shaped one. We will analyse each step for the fabrication to occur, starting from designing in the computer, to submitting the sample to the e-beam lithograph until having the array fabricated.

In the experimental chapter, which corresponds to a written paper, we examine how we conducted the experiments, both for the case of having the bare substrate or having the substrate with the cysteine adsorbed. We will see how we used the same procedure to take the spectra, the only difference in the experimental process being the previous steps of adsorbing the biomolecule onto the gold substrate.

Finally, the results will prove the possibility to characterize biomolecules, cysteine in our case, by use of plasmonic resonances and nanostructured gold shurikens. We will follow all the analytical process to get these results.

CHAPTER 1: THEORY

1.1 CHIRALITY

Chirality is a geometric property of an object: we call an object chiral if it is impossible to superimpose it onto its mirror image. Each of the components of this pair is called an enantiomer; an object that does not show chirality is achiral. Chirality can be assigned to all different kinds of objects, but probably, the most common example of chirality that can be found is in our bodies: the hands are chiral objects, as exemplified in Figure 1.

The chirality of a physical object cannot be parameterized. But, because light can also be chiral, the level of chirality in light can. This is done with quantity Lipkin described (Lipkin, 1964) that later Cohen and Tang described mathematically as the term optical chirality (Smart, 2011). The equation is as follows:

$$C = {[\varepsilon_0 E \cdot (\nabla \times E) + \mu_0^{-1} B \cdot (\nabla \times B)]}/{2} \quad (\text{eq. } 1)$$

In this equation, E and B's terms refer to the time-dependent electrical and magnetic field, respectively, while the terms ε_0 and μ_0 are the vacuum permittivity and permeability, respectively, of the medium we are analyzing and experimenting with on.

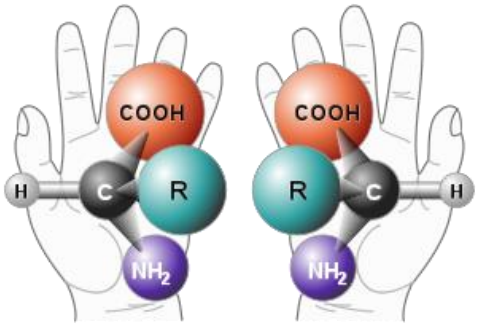

Figure 1. Image depicting the concept of chirality. It can be found both in molecules and in our hands.

1.2 CHIRALITY IN MOLECULES

Chirality can be found in biomolecules (molecules that play a role in any biological body) amongst many other different types of molecules. When talking about biomolecules, we can distinguish between D enantiomers and L enantiomers, depending on their handedness. A curious and interesting fact is that most amino acids that are generally naturally occurring are L – amino acids. That is the opposite situation as what happens with sugars: in general, naturally occurring sugars are mostly D – sugars. As a general rule, both enantiomers will have the same chemical and physical properties, only differing in one thing: their interaction with polarized light, being it plane or circularly polarized. This is referred to as the optical activity of the molecule, a chiroptical effect.

1.3 OPTICAL ACTIVITY

The geometrical chirality of a molecule or object is a prerequisite for exhibiting optical activity (Barron, 2004). Many molecules and biomolecules are chiral, as has been said previously. The defining characteristic of them is that they have remarkably strong optical chirality and optical activity (ibid.), which can then be measured and analyzed. One way to differentiate chiral molecules is by measuring their optical activity, as they interact differently with polarized light, the basis for the detection methods used in this field. The optical activity in chiral materials produces Optical Rotation (OR) when interacting with a beam of light, which can be detected using different techniques.

For instance, we have the Optical Rotatory Dispersion (ORD), which measures the number of degrees a solution of one enantiomer (for example, we can have a pure solution of D enantiomer) deviates a beam of plane-polarized light. The other enantiomer (the L enantiomer in this example) will turn the plane-polarized light to the same amount of degrees but in the other direction. To make it clear, if the D enantiomer solution made the plane-polarized light turn +3 degrees, the L enantiomer solution would turn the plane-polarized light -3 degrees.

Another way to measure the optical activity of biomolecules is by using the technique of Circular Dichroism. This technique is based on the fact that enantiomers absorb different amounts of left and right circularly polarized light (CPL). These differences are known as dissymmetries (Tang & Cohen, 2010).

This is a widely used method to detect the geometrical configuration of proteins as a technique based on the differential interaction of circularly polarized light (CPL). This method, though, can only see secondary and a small amount of tertiary (Fasman, 1996). Here is when superchiral fields, a concept that will be fully explained in the next section, play a crucial part: superchiral near fields of chiral plasmonic metamaterials are very sensitive to the tertiary structure and can even be able to detect the quaternary structure (ibid.). A nanostructured metamaterial can thrive this superchiral fields, so these kinds of materials can affect the CD of a chiral molecule dramatically due to the interaction between the mentioned metamaterial and the biomolecule (usually a protein) adsorbed, which interact forming then a complex and couple by different dipole and multipole Coulomb interactions (Geddes and Lakowicz, 2002), all initiated with the incident beam of light.

Both effects and techniques, ORD and CD, will be explained thoroughly in the following sections.

But, where does this optical activity come from? It arises from the fact that a chiral medium displays different n (refractive index) and k (extinction coefficient) for incident polarized light. When working with polarized light, then, the interaction of Left CPL and Right CPL with one chiral medium is different. Commonly, optical activity is measured with Linearly Polarized Light (LPL), which can be interpreted as a superposition of LH and RH CPL of the same amplitude (Jack, 2016).

We will now discuss the importance of n, the refractive index, and chirality. As has been said, this is the concept behind the rise of the phenomenon of OR. When linearly polarized light travels through a chiral medium, its two circular components travel at different velocities due to the refractive index. This differential amongst velocities makes the plane of polarized light rotate as the components come out of phase.

Mathematically, when a linearly polarized light beam of angular frequency $\omega = 2\pi c/\lambda$ goes in an optically active (chiral) medium at point z = 0, then at any instant E_{Left} and E_{Right} are at the same angle from the plane of propagation at the point z = 0. But at that exact instant, at some point z = l, in this active optical medium, the electrical field vectors of the light beam E_{Left} and E_{Right} are oriented at angles:

$$\theta_L = \frac{2\pi cl}{\lambda v_L} \quad (eq. 2)$$

$$\theta_R = \frac{2\pi cl}{\lambda v_R} \quad (eq. 3)$$

The terms υ_L and υ_R are the different velocities of the left and right components of the beam within the medium. The angle of rotation of this beam in the chiral medium, then, is:

$$\alpha = \frac{1}{2}(\theta_L + \theta_R) = \frac{\pi cl}{\lambda}\left(\frac{1}{v_L} - \frac{1}{v_R}\right) \quad (eq. 4)$$

But, because the refractive index (n) is n = c/v, the angle per unit length becomes:

$$\alpha = \frac{\pi}{\lambda}(n_L - n_R) \quad (eq. 5)$$

The resultant optical rotation, which is nothing more than the differences between the refractive indices n_L and n_R for the left and right circularly polarized light components in the medium, is a function of circular birefringence. By convention, if the medium rotates the plane of polarization clockwise when looking towards the light source, the medium is named dextrorotatory, whereas if it turns the plane of polarization anticlockwise, it is classed as laevorotatory (Tullius, 2017).

1.4 MAXWELL'S EQUATIONS

Maxwell's equations are a set of four different equations that, together with the Lorentz force law, describe the basis for classical electromagnetism, optics, and electric circuits. These expressions give an analytical model to describe how electric and magnetic fields are generated by charges, currents, and changes in the electromagnetic fields. They are basic, then, to understand all topics related to electromagnetism, plasmonics amongst them:

$$\nabla \cdot D = \rho_{ext} \quad (eq.6)$$

$$\nabla \cdot B = 0 \quad (eq.7)$$

$$\nabla \times E = -\frac{\delta B}{\delta t} \quad (eq.8)$$

$$\nabla \times H = J_{ext} + \frac{\delta D}{\delta t} \quad (eq.9)$$

When reading the equations as a whole, we have all parameters in electromagnetics related. D is the dielectric displacement, E the electric field, H the magnetic field, and B the magnetic induction. The value ρ_{ext} is an external charge density, and J_{ext} the current density. ∇, which appears in all equations, is the operator gradient.

Equation 6 is known as Gauss's law, and it relates the distribution of electric charge concerning the existing electrical field. Equation 7 is Gauss's law for magnetism, and it states that the magnetic field B has divergence equal to zero, meaning that magnetic monopoles do not exist, and the fundamental entity with magnetism is the magnetic dipole. Equation 8 is Faraday's law of induction, and it explains how a magnetic field interacts with an electric circuit to create a force. In other words, it defines electromagnetic induction. Finally, equation 9 is Ampère's circuital law, which relates an integrated magnetic field in a loop to the electric current that passes through this same loop.

The problem with these equations is that they do not represent many other phenomena that can happen in media, such as diffraction, refraction, or scattering phenomenon, or how to consider these and their effect on the behaviour of electromagnetic waves. To correct this, constitutive equations are necessary.

The constitutive equations express the magnitudes D and B as a function of E and H. these equations are as follows (Mayer, 2007):

$$D = \varepsilon_0 \varepsilon_r E \quad (eq.10)$$

$$B = \mu_0 \mu_r H \quad (eq.11)$$

In these two expressions, the values of ε_0 and μ_0 are respectively the electric and magnetic permittivity of the vacuum.

This work will need to adapt the equations to account for the chirality of the medium. The constitutive equations are adjusted, so they characterize the vector field of the system (Kelly et al., 2018), which arises from the chirality of itself. The equations used will be then (Monticone et al., 2017):

$$\mathbf{D} = \varepsilon_0 \varepsilon_r \mathbf{E} + i\xi^T \mathbf{B} \quad (\text{eq. } 12)$$

$$\mathbf{H} = \frac{\mathbf{B}}{\mu_0 \mu_r} + i\xi^T \mathbf{E} \quad (\text{eq. } 13)$$

These equations are the basis used in the mathematical simulations done to confirm the experimentation and presented in the following chapters. They are used to create the frame in which the simulations work and to specify the light behaviour.

These simulations are done by using a Finite Element Modelling software, COMSOL. As they state on their website, 'COMSOL Multiphysics® is a general-purpose simulation software for modelling designs, devices, and processes in all fields of engineering, manufacturing, and scientific research. We used this program to obtain the spatial distribution of the chiral electromagnetic fields that arise from the microstructured gold shurikens.

This software simulates an incident plane-polarized light beam on the structures, which has the previously designed properties according to the material. These properties are, namely, the refractive index n and the extinction coefficient k, which gives information about the amount of attenuation of the electromagnetic wave when propagating through the experimental material. For all the studied wavelengths. When the program computes all the input gives the results both as tabulated data when simulating, for example, the Reflectance spectra, or by maps when simulating the electromagnetic fields or the chirality. Chapter 5 is dedicated to COMSOL, explaining thoroughly how we prepared and programmed the needed simulation in all cases.

We will be using it to check the experimental results previously presented. Simulations will be made at angles of incidence of 0º, 15º, 25º, and 40º, and with y and x polarized light, which corresponds to the long and short axis, respectively.

In Figure 2, there is an example of an Electrical Field Map, an Optical Chirality Map, and a Magnitude Map, all of which simulated using this software.

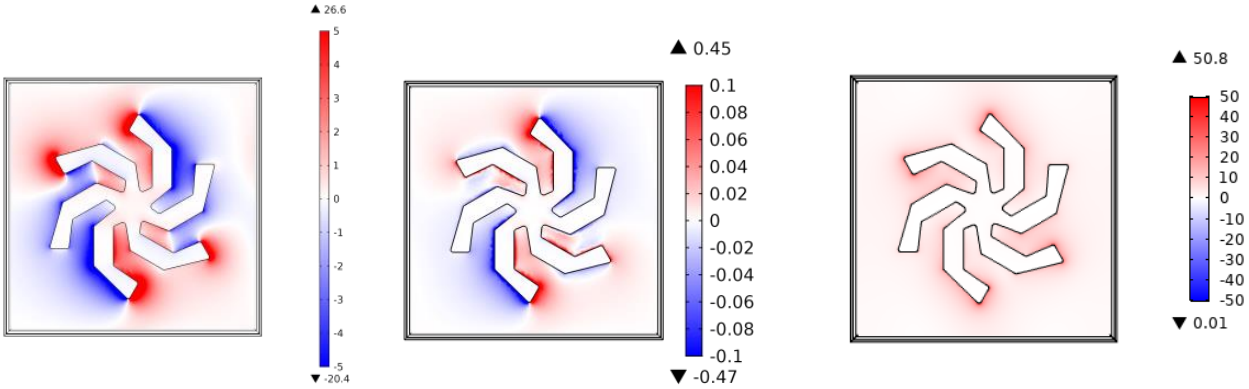

Figure 2. Examples of an Electrical Field Map, an Optical Chirality Map, and a Magnitude Map, in that order, of the simulations done with COMSOL.

1.5 SUPERCHIRAL FIELDS

Superchiral fields are evanescent electromagnetic fields that rise from chiral nanostructures or, in the case studied in this work, as well as microstructures. It is well known that there is a different interaction of differently polarized light with planar chiral nanostructures (Reichelt et al., 2006), and that gives rise to OR effects previously explained.

What are superchiral fields at their origin? There is a mismatch between the helical pitch of circularly polarised light and the relatively small size of chiral molecules such as proteins. Superchiral fields are more sensitive to the higher-order structure of proteins than ordinary circular dichroism spectroscopy because of the smaller mismatch between the helical pitch of the near superchiral fields and the length of the chirality of these higher-order structures (ibid).

A circularly polarised wave has a helicity that is dependent on the wavelength of the light so that the circularly polarised field rotates a full 360º in one wavelength. This is larger than the regular size of chiral molecules (which is around the tens of nanometres), so the circularly polarised field undergoes a slight perceptible twist over the distance of molecular dimensions (Mason, 1982).

In recent years, it was discovered and recognized that an enhanced dissymmetry should happen if the field lines were reoriented over a shorter distance than the wavelength, ideally close to the size of molecules (Tang & Cohen, 2010). When this occurs, the spatial scale of molecular chirality and the chirality of the light will match, enhancing greatly the signal we get from the experimental work.

It was seen as well that these chiral interactions require a time – even pseudoscalar to describe the chirality of the electromagnetic fields. It was the year 1964 when Lipkin introduced a series of conserved quantities to describe electromagnetic waves in a vacuum (Lipkin, 1964). Since then, it has been realized that one of these quantities with a time–even pseudoscalar is the optical chirality referred to in equation 1.

This optical chirality quantity measures the degree to which the electric and magnetic field vectors, E and B, wrap around a helical axis at each point in space. When we are discussing circular dichroism, the dissymmetry factor named ‘g’ is a dimensionless value that measures the enantioselectivity of a system (Choi & Cho, 2012):

$$g = \frac{A_L - A_R}{\frac{1}{2}(A_L + A_R)} \quad (\text{eq. } 14)$$

The subscripts L and R refer to left- and right- CPL, respectively. This dissymmetry factor, g, was explained as to include the optical chirality parameter, C (Tang & Cohen, 2010):

$$g = g_{CPL}\left(\frac{cC}{2U_e\omega}\right) \quad (eq.\,15)$$

Where g_{CPL} the dissymmetry factor under circularly polarised light, c is the speed of light, C is the optical chirality, U_e is the local electric energy density, and ω is the angular frequency. Equation 7 shows that, not like circular dichroism, this magnitude of the dissymmetry factor, g, is dependent on the optical chirality, C, and not only governed by the chirality of the matter being analyzed. Because the field vectors of the light rotate entirely once per unit of wavelength constantly for CPL, the quantity $\frac{cC}{2U_e\omega}$ equals 1. That's why, to increase the dissymmetry factor is necessary an increase of the optical chirality C, which will lead to a rise in the mentioned quantity, which will then be greater than 1. When this is the case, the fields generated are known as superchiral fields. The most common and easiest way to enhance the optical chirality C is through the use of plasmonic nanostructures (Hendry et al., 2010; Schäferling, Dregely, Hentschel, & Giessen, 2012). These structures create strong electric and magnetic fields near the structures.

1.6 PLASMONS and PLASMONIC RESONANCES

If we look at metals from an electromagnetic point of view, metals can be considered plasmas (Murray & Barnes, 2007). Due to the nature of the metallic bond, there are free electrons in any metal substrate or sample. These free electrons are collectively known as the electron cloud or are referred to as the electron sea model. When some light beam irradiates this cloud, the energy transmitted excites the electrons so that it causes a collective oscillation. This collective oscillation is then known as being the quasiparticle plasmon.

The interest for plasmons and plasmonics rises from the fact that plasmons can manipulate light at the nanoscale of the structures and substrates used (Brongersma & Shalaev, 2010). Recently, there has been a lot of interest and research in plasmonic science. This is because of their use in biosensing (Anker et al., 2008), amongst other areas of science, including nanoscale lasers, plasmon-assisted photolithography, or plasmon – enhances solar energy harvesting (Chen, Shao, Woo, Wang, & Lin, 2012).

This plasmon can then be detected and characterized; it resonates at a specific frequency (dependant on different variables, as will be explained further in this chapter). This detected resonance is known as the plasmonic resonance and the resulting peak as the plasmonic peak.

We can differentiate between two basic types of plasmons: localized, known as Mie plasmons, or delocalized, known as well as Bragg plasmons (Kelf, Sugawara, Baumberg, Abdelsalam, & Bartlett, 2005).

Localized Mie plasmons are confined in a specific space and geometry on a surface. It can be said that, in a sense, they are trapped modes. For example, in (Kelf, 2006) it is shown how these resonances are occurring in a metallic nanovoid. Under certain conditions, when having two different plasmon modes, they can interact and give rise to what is referred to as a Fano resonance (Maurer, Adam, & Lévêque, 2015). This is a resonance characterized by an asymmetric profile in the extinction spectrum. It is a feature typical of quantum systems (Luk'Yanchuk et al., 2010), but it has a characteristic shape that can be found when working in plasmonics, hence referring to this kind of resonances as Fano resonances. The Fano resonance will be explained in detail in the following sections.

Delocalized Bragg plasmons, or surface plasmons, are electromagnetic waves coupled to charge fluctuations (Kelf et al., 2006). The Bragg plasmon is a plasmonic resonance that gives a peak that is dependent on the angle of the incident light, as the plasmonic peak position is affected by it. We can find this kind of behaviour when having a periodic metallic grating (Epstein, Dolev, Bar-Lev, & Arie, 2012). When having a metal and a dielectric on top, the surface plasmons can propagate freely between them (Kelf et al., 2005). The energy of these plasmons directly depends on the direction of propagation of the surface plasmon (ibid).

Plasmons can become localized if the field fluctuations become spatially pinned and disconnected from each other (Kelf et al., 2005), turning them from being Bragg plasmons to Mie plasmons. By changing the specificities of the metal structures used, then, we can tune how much of Mie or Bragg plasmon do we want.

We will be most interested in the biosensing application. As (Govorov & Fan, 2012) puts it, 'plasmonic nanocrystals (in our case, nanostructures) strongly interact with chiral molecular shells through electric and magnetic fields and in this way acquire new chiro – optical properties'.

1.7 SURFACE PLASMONS POLARITONS

Surface plasmon polaritons (SPP) are excitations with an electromagnetic origin that exist and propagate along with a metal–dielectric interface, such as a metal with a protein bonded on top of it. These electromagnetic surface waves happen because of the coupling between the electromagnetic field and the oscillating plasma of the metal (Maier, 2007). The combined excitation of a surface plasmon and an electromagnetic wave is called then a surface plasmon polariton (Jack, 2016) and is graphically represented in Figure 3.1.

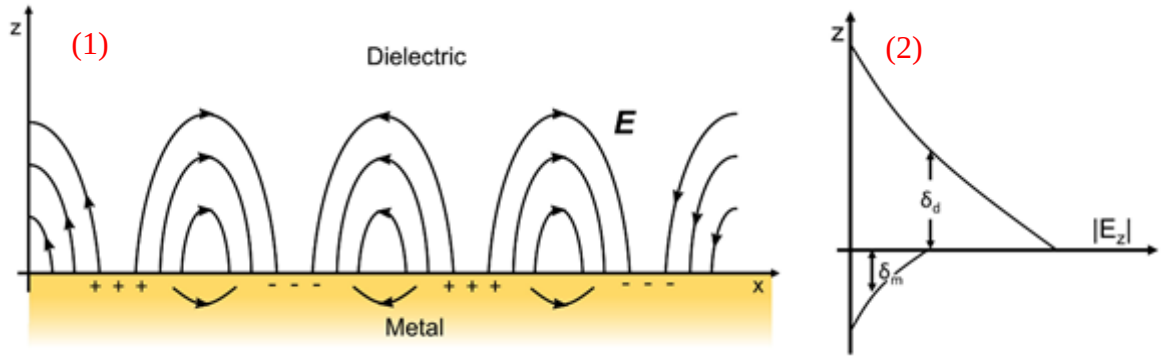

Figure 3. (1) Schematic representation of metal charge distribution and the occurring electric fields in both the metal and dielectric due to surface plasma oscillations (surface plasmon polaritons). (2) Graphic representing the exponential decay of the fields with distance.

The collective plasmonic oscillation of the surface charges, which have been explained in the previous section, excites the surface plasmon polaritons with a different frequency from that of the bulk plasma of the metal. Generally, the surface plasmon polariton frequency is lower than the bulk plasma frequency of the metal to be excited at lower energies (Tullius, 2017). This can be mathematically explained with the equation for the resonance frequency of the SPP:

$$\omega_{spp} = \frac{\omega_p}{\sqrt{2}} \quad (\text{eq. } 16)$$

The first one is the propagation along the metal surface in the x-direction. It will gradually attenuate because of ohmic losses that mainly occur due to the absorption of the metal. That is why the internal damping of the metal limits the propagation length of this surface plasmon polariton we are working with and, therefore, depends on the dielectric constant of the metal and the incident wavelength of light. In contrast to this propagation, we have field components perpendicular to the interface between metal and dielectric. Those exhibit exponential decay as the distance from the metal surface increases (Figure 3.2). This near–field protrudes into both materials, but the field decay in the dielectric material usually is more extensive. On the other hand, in the metal, the field is equivalent to the skin depth of the metal. Resultant from the surface-bound, non – radiative origin of SPPs confinement of light at the metal surface creates large field intensities at SPP frequencies (Jack, 2016).

When the surface plasmon polariton is excited, it propagates along the metal surface. As a result of the propagating wave, there is a rise of non – propagating evanescent fields that extend perpendicular to the surface into both the metal and the dielectric, which have already been discussed. The size and distance that these fields extend into both the metal and the dielectric depend on the two interfaces' relative permittivity and decreases exponentially with the distance from the interface.

This distance that the evanescent fields cover can be understood as penetration depths, δm, and δd, for the metal and dielectric, respectively. For example, with gold and water as the metal and dielectric, the penetration depths with incident light at 630 nm are 29 nm for δm and 162 nm for this same wavelength (Homola, Yess & Gauglitz, 1999). It can be seen that the penetration depth for the dielectric is much larger than for the metal, and as they decay exponentially are much more concentrated near the interface.

1.8 METAMATERIALS and PLASMONS

A metamaterial is an engineered material for it to have unique properties not found in nature (Karimullah et al., 2015). They have been applied to different uses, such as creating negative refractive index media, broadband circular polarisers, or superchiral electromagnetic fields for ultrasensitive characterization of biomaterials (Abdulrahman et al., 2012) (Tullius et al., 2015). This last case is the one we are interested in most in the work presented here. Reason for that being that evanescent EM fields rising from chiral nanostructured metamaterials can significantly enhance the sensitivity of a chiroptical measurement (Hendry, Mikhaylovskiy, Barron, Kadodwala, & Davis, 2012). We will want to design and fabricate structures that comply with this to detect and characterize proteins. In the chapter on Fabrication, there is a detailed explanation of the process of creating these metamaterials and their properties and how the structures were engineered to get the desired properties, which can be dependent on several factors.

The materials that will be used in this work are metamaterials fabricated by us in the JWNC facility at the University of Glasgow, following the discussed procedure in the chapter before.

Plasmonic metamaterials will be the focus of the current study. Several types of materials can be used in this particular wavelength, such as are metal nitrides, graphene, conducting oxides, and others (Zhong, Malagari, Hamilton, & Wasserman, 2015). There are only a few metals that support plasmonic resonances, and noble metals are the ones that work best (Pendry, n.d.) for these purposes. The metal we chose to work with is gold. For a metal to support a plasmon resonance, some conditions have to be complied with. This element has a significant negative permittivity, which is relevant in the plasmonic studies that we do as it enables the metal to support plasmonic resonances (Park, 2014).

These materials will have, as well, a specific structure (shuriken type structure) and a definite size (0.75, 1, and 2 micrometres). Because of the very small size of the structures, they will be ordered in an array. The arrays used in this work are 0.5 by 0.5 centimetres. Each array, then, will contain millions of structures. The distance between one point of one structure and the same exact point of the immediately adjacent structure is known as pitch. This is a defining variable used to characterize the structures and the whole array. This study used a pitch of 1.5 in all structures (implying that there will be half a structure size space between structures). All the fabrication processes will be detailed explained further in the work.

The most important thing about the structures studied is that they are chiral. A review of chiral metamaterials' importance can be found at (Wang, Zhou, Koschny, Kafesaki, & Soukoulis, 2009). When we have chiral metamaterials, that is, we have one structure and its enantiomer, we can see different effects happening or different results depending on the structure used. These structures will be referred to as being Left Handed or Right Handed. The chirality of the metamaterials and their different interaction with light is central to this study.

1.9 DARK AND BRIGHT MODE COUPLING

We will be working with structures that can raise resonance modes that are of utmost importance to explain the effects. The optical modes that arise in the interface between the structured metal and the dielectric are known as plasmonic modes, resulting from the plasmonic resonances interacting with the Surface Plasmon Polaritons. When the separation between particles or structures in an array of a metamaterial is small enough, there is an overlap of these plasmonic modes (Rodier, 2019), and the strong near–fields that are rising interaction between them leads to the appearance of individual particle plasmon modes to form a new set of coupled modes delocalized over the whole structure. It has been previously demonstrated that this coupling can be understood as a coupling between dipolar or quadropolar plasmonic resonance modes (Schäferling, 2017). These two modes that appear are symmetric and antisymmetric, respectively, considering the oscillation of the surface plasmons and how they interact. The symmetric mode will be of lower energy, and the anti–symmetric mode of higher energy (Park, 2014). This symmetric mode corresponds to a dipolar moment, whereas the other one has a pole of higher magnitude like is a quadrupole. That is the reason why this mode has no interaction with light and is often "invisible" in experiments and simulations, but it can interact with the symmetric mode to produce Fano resonances as described in reference (Park, 2014). For these reasons, the symmetric dipolar mode is often referred to as the bright mode and the antisymmetric mode as the dark mode. It is this Fano shape-like spectra that we are primarily interested in, and it will be explained in detail in the following section.

In this work, we will have evidence of the coupling between these two modes and how we can tune this in order to get desired shape spectra and properties.

1.10 INTERFERENCES: THE FANO RESONANCE

There is a basic interference phenomenon of relevance to this work: the Fano. This effect results from the coupling between the bright and dark plasmonic modes (Rodier, 2019), and so it is essential when studying these kinds of systems. It has a very characteristic spectra profile that we can identify in our own experimental work, and so we relate this effect with our work.

The first one to describe this kind of resonance was Ugo Fano, and he described it as a coupling between two modes: a discrete one and a continuous one in a paper in the mid – 90s of the last century (Fano, 1965). When having frequencies that are far from the characteristic resonant frequency of the plasmonic system, the background scattering process (which is the continuum process) dominates.

But, as the system comes closer to this characteristic resonant frequency, the background scattering amplitude slowly changes with energy while the resonant scattering amplitude displays important changes in both phase and amplitude. When reaching the resonant frequency, this phase change brings with it destructive and constructive interference phenomena between the two states, discrete and continuum, over an extremely narrow spectral range. It gives a very characteristic line shape instead of a more typical Lorentzian spectrum, as can be seen displayed in Figure 4. We can observe in that Figure the appearance of a second resonance due to the interference between states, which can be understood as a splitting.

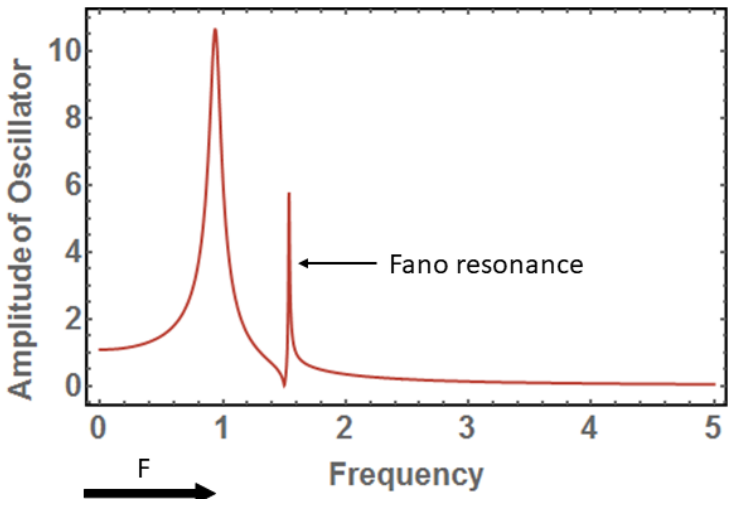

Figure 4. Spectrum displays a typical Fano resonance line shape showing the coupling between two resonance modes. The Figure is taken from (Rodier, 2019).

.

In the plasmonic spectroscopy that is central to this work, the continuous mode is generated by the background (a surface wave), whereas the discrete mode rises from the hotspot (a localized mode). To explain this, in other words, we can assign them to be a strong bright mode and a weak dark mode (localized) (Miroshnichenko, Flach, & Kivshar, 2010). For the interferences, and more specifically the Fano resonance, to occur, these modes have to be overlapping at a frequency spectra (Limonov, Rybin, Poddubny & Kivshar, 2017). This condition is satisfied in a plasmonic material as different resonances occur for all eigenmodes of structures and spectrally overlap in similar positions (Verellen, Sonnefraud, Sobhani, Hao, Moshchalkov, Van Dorpe, Nordlander & Maier, 2009). Thus, the bright mode can be excited by the incident beam of an electromagnetic wave, not like the dark mode that cannot be directly excited with this beam. But this dark mode can be indirectly excited by the near field arising from the bright mode (Luk'Yanchuk et al., 2010). The field generated by this indirectly excited dark mode will interfere with the bright mode generated field. This interference phenomenon can either enhance or diminish the signal, which is controlled by the phase of each field (Giannini, Francescato, Amrania, Phillips & Maier, 2011).

What will be demonstrated later in this work is that we get, both experimentally and by computer simulations, spectra that show this typical shape, which will lead us to conclude that we are dealing with an interference phenomenon.

1.11 DEPENDENCE OF PLASMONIC RESONANCES

The plasmonic resonance position depends on several factors (Haes & Van Duyne, 2002) of the properties of the substrate and sample used. They all relate to the nature of the structures, the characteristics, and the specificities of the metamaterials in the experiment.

- SIZE: the peak position is directly dependent on the structure size. Typically, the bigger the structure, the redder shifted the peak appears. This is because the chiral near-fields that are created by the interaction between the structure and the incident light change, being of lower energy as the structure becomes bigger (therefore, the red–shift) (Peng, McMahon, Schatz, Gray, & Sun, 2010). A good reference that explains how the resonances are affected by the size of the plasmon is (Kravets et al., 2014).
- PITCH: the pitch is the distance between one point of one structure and the exact same point of the adjacent structure. The pitch can be tuned when designing the structures, affecting the plasmonic peak. This effect will not be studied here.
- SHAPE: the shape of the used structure will affect the properties of the plasmonic peak (Mayer & Hafner, 2011). Different shapes will give rise to different plasmonic resonances, and therefore, different near electromagnetic fields on top of the mentioned structure. This effect will not be studied here.

1.12 SYMMETRY

The concept of symmetry is fundamental in many fields. Chemistry is one of them and is something largely studied. In this work, symmetry will be relevant in the last chapter of results, SPLITTING ANGLE DEPENDENCE.

There are objects (like molecules or the objects we experimented on in this work, shurikens) that have internal symmetry. Symmetry can be categorized, basically, in dependence on what elements of symmetry we find in them (Atkins et al., 2006). Those are five different items, which are tabulated in Table 1.

Symmetry operation	Symmetry elements	Symbol
IDENTITY	ALL THE SPACE	E
ROTATION	ROTATION AXIS	C_n
REFLEXION	PLANE	σ
INVERSION	INVERSION CENTRE	i
ROTATION + REFLEXION	IMPROPIOUS ROTATION AXIS	S_n

Table 1. Items of symmetry that can be found in objects.

For this work, we will mainly be interested in two of these items of symmetry: the rotation symmetry axis and the inversion centre. A rotation respect a symmetry axis consists in rotating the object (from this point, all the examples will be explained using the structures we work with in the last chapter of results: shurikens) a certain number of degrees (which are generally denominated as $360º/n$) and the shuriken appearing without changes, being identical as previous the rotating happened. We then can characterize a rotation axis, C_n, by which this rotation occurs. We are working with six armed shurikens on the case exposed here, so the structure will be C_6 since we can rotate the object six times, and every time the shuriken will be the same. A schematic of this can be seen in Figure 5.

Figure 5. Diagram showing the properties of a C_6 axis. If we turn the structure clockwise or anticlockwise, taking the yellow dot as an axis entering the image six times, every time we get the same exact structure.

The inversion centre is the symmetry operation by which each point of the object is connected to an identical point by drawing a line that passes through the centre of the structure and is at an equal distance from it. Our shurikens have an inversion centre. A schematic of this can be seen in Figure 7.

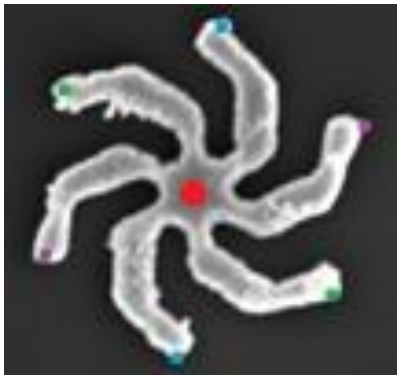

Figure 7. Diagram showing the properties of an inversion point (red, in the centre of the image). If we take a blue point and apply the operation of the point of inversion, we get the other blue point. The same goes for the green and purple points.

Each object or molecule can be defined by a term that comprises each and every one of its symmetry properties and is called a symmetry point group. These point groups are characterized by the symbol deduced from the diagram of Schoenflies. This notation is used to specify the point group of an object in three dimensions. This diagram can be found in Figure 8. As can be seen, it provides an easy way to determine to which point group an object pertains.

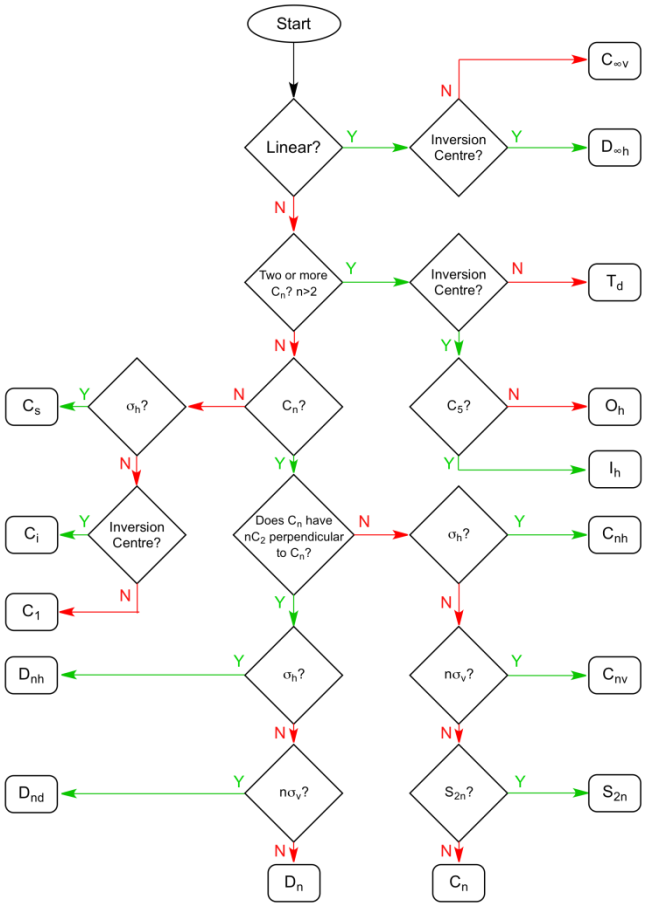

Figure 8. The diagram to determine the symbol of Schnoeflies for a chiral object. At each point, you have two options for determining some property of the object, being those yes or no, which makes it very useful and easy to use in determining the symmetry of any object or molecule.

A table of characters resumes all the symmetry elements we find in each group. In these tables, shown in Table 2 an example of it, we find several elements, listed below:

- **Name of the point group**: the name of the group according to the diagram in Image 6, designated by the symbol of Schoenflies.
- **Symmetry elements**: all the elements that pertain to the group
- **Symmetry labels, irreducible representations**: names given to every type of symmetry.
- **Linear Functions**: functions that can be applied to each type of symmetry. When we find (x, y, z) terms in this column, the resonance is active in the IR because it is a resonance affecting the dipolar moment of the object. This is what interests us most since we are working with IR light in this work.
- **Quadratic Functions**: functions that can be applied to each type of symmetry. When we find (xx, yy, zz, xy, yz and xz) terms in this column, the resonance is active in Raman spectrometry.
- **Additional functions**: these functions, such as the shown cubic functions in the example Table 2, give us more information about the resonances. Because these functions won't be used in this work, we won't further discuss them.
- **Numbers in the table** represent the effect of every symmetry element on every symmetry label.

As an example of a table of characters, we'll take the one corresponding to the point group D_{4d}, shown in Table 1.

D_{4d}	E	$2S_8$	$2C_4$	$2(S_8)^3$	C_2	$4C'_2$	$4\sigma_d$	linear functions, rotations	quadratic functions	cubic functions
A_1	+1	+1	+1	+1	+1	+1	+1	-	x^2+y^2, z^2	-
A_2	+1	+1	+1	+1	+1	-1	-1	R_z	-	-
B_1	+1	-1	+1	-1	+1	+1	-1	-	-	-
B_2	+1	-1	+1	-1	+1	-1	+1	z	-	z^3, $z(x^2+y^2)$
E_1	+2	$+(2)^{½}$	0	$-(2)^{½}$	-2	0	0	(x, y)	-	(xz^2, yz^2) $[x(x^2+y^2), y(x^2+y^2)]$
E_2	+2	0	-2	0	+2	0	0	-	(x^2-y^2, xy)	$[xyz, z(x^2-y^2)]$
E_3	+2	$-(2)^{½}$	0	$+(2)^{½}$	-2	0	0	(R_x, R_y)	(xz, yz)	$[y(3x^2-y^2), x(x^2-3y^2)]$

Table 1. Table of characters for the point group D_{4d}. Circled red is the point group, and circled blue are the symmetry elements. Circled green are the irreducible representations.

In that table, we find the point group (circled red), the symmetry elements (circled blue), the functions, the quadratic functions, and the additional functions (here, cubic functions), titled already on the table. Circled green are the irreducible representations, starting each with a letter: A, B, or E. These are a fundamental type of symmetry of the group.

The letter A is related to the principal symmetry function C_n, meaning that the object is symmetric regarding this axis. Letter B indicates that the function changes sign with this same symmetry function applied. Subindeces 1 and 2 represent, respectively, that the function is symmetric in regards to a C_2 operation applied or that the function changes sign: it is then an asymmetric function.

Letter E means that the resonance related to this point group is double degenerated; it exists in two dimensions. We can find as well a T, meaning that we will have a triple degenerated resonance existing in three dimensions.

The linear functions and the quadratic functions contain information about the characteristics that this type of symmetry exhibits. This is, as has already been explained if they are active in the IR or Raman spectroscopy.

It is important now to dedicate the end of this section to explain how to read a characters table to understand its utility better.

The one-dimensional irreducible representations in a table of characters can only have the numbers 1, -1, or 0. When a specific symmetry operation is applied, which number exists depends on how the basic function of these operations behaves. Character +1 applies when the basic function remains unchanged with the applied operation, character -1 when it reverses, character 0 when the function undergoes other changes.

1.13 THE AMIDE RESONANCE in the IR

Amide resonances give structural information about a protein, so amide vibrational spectroscopy is a valuable technique for characterizing protein structure (DeFlores, Ganim, Nicodemus, & Tokmakoff, 2009). Specifically, they give us information about the protein configuration to see how much of the primary, secondary, tertiary, or quaternary structure they have (Gallagher, 1997).

The amide bond is formed between two amino acids. This bond is also known as a peptide bond. Figure 9 is taken from Gallagher, 1997, and shows the nature of this bond.

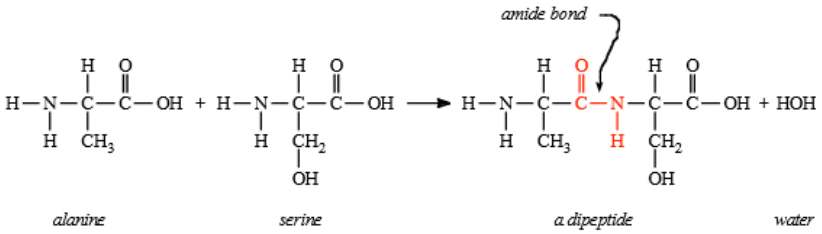

Figure 9. Nature of the amide or peptide bond, the example is showing the bonding between two aminoacids: alanine and serine.

A dipeptide is the name that receives two amino acids linked by the amide bond. The structure of a protein is the result of a series of amide bonds and subsequent folding of the protein.

The primary structure of proteins is the genetic sequence of amino acids, represented as a string of the mentioned amino acids (Ibid., 1997). The secondary structure includes $\alpha-$ helices and $\beta-$ sheets, structures that allow the amides to hydrogen bond very efficiently (Ibid., 1997) and a structure known as random coil structure. Finally, tertiary structure is found when different elements of secondary structure pack together to create a three-dimensional structure.

The elements of the amide bond have specific and well-known resonances. They are known as amide I and amide II. Amide I is the most studied protein vibration, as DeFlores states in his paper of 2009. This vibration is composed basically of peptide carbonyl stretch and is sensitive to secondary structure. Some studies found that $\beta-$ sheets have a strong absorption band at $1610-1640\ \mathrm{cm}^{-1}$ and a weaker band at $1680-1690\ \mathrm{cm}^{-1}$. On the other hand, $\alpha-$ helices and random coil structures have bands at $1640-1650\ \mathrm{cm}^{-1}$ and $1650-1660\ \mathrm{cm}^{-1}$, respectively (De Campos Vidal & Mello, 2011).

The amide II resonance comes from the NH bend and the CN stretch, as can be found as well in this DeFlores paper of 2009. This resonance appears at a region around$1450\ \mathrm{cm}^{-1}$.

As will be seen, the plasmonic peaks obtained from the one-micrometre structure correlate with the amide I band region. The project's initial goal was to study the use of this plasmonic peak in the amide region to develop a method to easily detect this resonance. It changed once we became aware of a splitting that was found. Its origins and its consequences will be the main topic of this work.

1.14 BIBLIOGRAPHY

Abdulrahman, N. A., Fan, Z., Tonooka, T., Kelly, S. M., Gadegaard, N., Hendry, E., … Kadodwala, M. (2012). Induced chirality through electromagnetic coupling between chiral molecular layers and plasmonic nanostructures. *Nano Letters*, *12*(2), 977–983. https://doi.org/10.1021/nl204055r

Anker, J. N., Hall, W. P., Lyandres, O., Shah, N. C., Zhao, J., & Van Duyne, R. P. (2008). Biosensing with plasmonic nanosensors. *Nature Materials*, *7*(6), 442–453. https://doi.org/10.1038/nmat2162

Brongersma, M. L., & Shalaev, V. M. (2010). The case for plasmonics. *Science*, *328*(5977), 440–441. https://doi.org/10.1126/science.1186905

Chen, H., Shao, L., Woo, K. C., Wang, J., & Lin, H. Q. (2012). Plasmonic-molecular resonance coupling: Plasmonic splitting versus energy transfer. *Journal of Physical Chemistry C*, *116*(26), 14088–14095. https://doi.org/10.1021/jp303560s

Choi, J. S., & Cho, M. (2012). *Limitations of a superchiral field*. *063834*, 1–22. https://doi.org/10.1103/PhysRevA.86.063834

De Campos Vidal, B., & Mello, M. L. S. (2011). Collagen type I amide I band infrared spectroscopy. *Micron*, *42*(3), 283–289. https://doi.org/10.1016/j.micron.2010.09.010

Deflores, L. P., Ganim, Z., Nicodemus, R. A., & Tokmakoff, A. (2009). Amide I ## II # 2D IR Spectroscopy Provides Enhanced Protein Secondary Structural Sensitivity Amide I ′ - II ′ 2D IR Spectroscopy Provides Enhanced Protein Secondary Structural Sensitivity. *Spectroscopy*, (18), 3385–3391. https://doi.org/10.1021/ja8094922

Epstein, I., Dolev, I., Bar-Lev, D., & Arie, A. (2012). Plasmon-enhanced Bragg diffraction. *Physical Review B - Condensed Matter and Materials Physics*, *86*(20), 1–5. https://doi.org/10.1103/PhysRevB.86.205122

Gallagher, W. (1997). FTIR Analysis of Protein Structure. *Biochemistry*, (1958), 662–666.

Geddes, C. D.; Lakowicz, J. R. J. Fluoresc. 2002, 12, 121

Govorov, A. O., & Fan, Z. (2012). Theory of chiral plasmonic nanostructures comprising metal nanocrystals and chiral molecular media. *ChemPhysChem*, *13*(10), 2551–2560. https://doi.org/10.1002/cphc.201100958

Govorov, A. O., Fan, Z., Hernandez, P., Slocik, J. M., & Naik, R. R. (2010). Theory of circular dichroism of nanomaterials comprising chiral molecules and nanocrystals: Plasmon enhancement, dipole interactions, and dielectric effects. *Nano Letters*, *10*(4), 1374–1382. https://doi.org/10.1021/nl100010v

Govorov, A. O., Gun'Ko, Y. K., Slocik, J. M., Gérard, V. A., Fan, Z., & Naik, R. R. (2011). Chiral nanoparticle assemblies: Circular dichroism, plasmonic interactions, and exciton effects. *Journal of Materials Chemistry*, *21*(42), 16806–16818. https://doi.org/10.1039/c1jm12345a

Haes, A. J., & Van Duyne, R. P. (2002). A nanoscale optical biosensor: Sensitivity and selectivity of an approach based on the localized surface plasmon resonance spectroscopy of triangular silver nanoparticles. *Journal of the American Chemical*

Society, *124*(35), 10596–10604. https://doi.org/10.1021/ja020393x

Hendry, E., Carpy, T., Johnston, J., Popland, M., Mikhaylovskiy, R. V., Lapthorn, A. J., … Kadodwala, M. (2010). Ultrasensitive detection and characterization of biomolecules using superchiral fields. *Nature Nanotechnology*, *5*(11), 783–787. https://doi.org/10.1038/nnano.2010.209

Hendry, E., Mikhaylovskiy, R. V., Barron, L. D., Kadodwala, M., & Davis, T. J. (2012). Chiral electromagnetic fields generated by arrays of nanoslits. *Nano Letters*, *12*(7), 3640–3644. https://doi.org/10.1021/nl3012787

Jack, C. (2016). *CALUM THESIS: Chiroptical Spectroscopy of Biomolecules Using Chiral Plasmonic Nanostructures*. (July).

Karimullah, A. S., Jack, C., Tullius, R., Rotello, V. M., Cooke, G., Gadegaard, N., … Kadodwala, M. (2015). Disposable Plasmonics: Plastic Templated Plasmonic Metamaterials with Tunable Chirality. *Advanced Materials*, *27*(37), 5610–5616. https://doi.org/10.1002/adma.201501816

Kelf, T. A., Sugawara, Y., Baumberg, J. J., Abdelsalam, M., & Bartlett, P. N. (2005). Plasmonic band Gaps and trapped plasmons on nanostructured metal surfaces. *Physical Review Letters*, *95*(11), 1–4. https://doi.org/10.1103/PhysRevLett.95.116802

Kelf, T. A., Sugawara, Y., Cole, R. M., Baumberg, J. J., Abdelsalam, M. E., Cintra, S., … Bartlett, P. N. (2006). Localized and delocalized plasmons in metallic nanovoids. *Physical Review B - Condensed Matter and Materials Physics*, *74*(24), 1–12. https://doi.org/10.1103/PhysRevB.74.245415

Kelly, C., Khosravi Khorashad, L., Gadegaard, N., Barron, L. D., Govorov, A. O., Karimullah, A. S., & Kadodwala, M. (2018). Controlling Metamaterial Transparency with Superchiral Fields. *ACS Photonics*, *5*(2), 535–543. https://doi.org/10.1021/acsphotonics.7b01071

Kravets, V. G., Schedin, F., Pisano, G., Thackray, B., Thomas, P. A., & Grigorenko, A. N. (2014). Nanoparticle arrays: From magnetic response to coupled plasmon resonances. *Physical Review B - Condensed Matter and Materials Physics*, *90*(12). https://doi.org/10.1103/PhysRevB.90.125445

Lipkin, D. M. (1964). Existence of a new conservation law in electromagnetic theory. *Journal of Mathematical Physics*, *5*(5), 696–700. https://doi.org/10.1063/1.1704165

Luk'Yanchuk, B., Zheludev, N. I., Maier, S. A., Halas, N. J., Nordlander, P., Giessen, H., & Chong, C. T. (2010). The Fano resonance in plasmonic nanostructures and metamaterials. *Nature Materials*, *9*(9), 707–715. https://doi.org/10.1038/nmat2810

Maurer, T., Adam, P. M., & Lévêque, G. (2015). Coupling between plasmonic films and nanostructures: From basics to applications. *Nanophotonics*, *4*(1), 363–382. https://doi.org/10.1515/nanoph-2014-0015

Mayer, K. M., & Hafner, J. H. (2011). Localized surface plasmon resonance sensors. *Chemical Reviews*, *111*(6), 3828–3857. https://doi.org/10.1021/cr100313v

Miroshnichenko, A. E., Flach, S., & Kivshar, Y. S. (2010). Fano resonances in nanoscale structures. *Reviews of Modern Physics*, *82*(3), 2257–2298.

https://doi.org/10.1103/RevModPhys.82.2257

Monticone F, Alù A. Metamaterial, plasmonic and nanophotonic devices. Rep Prog Phys. 2017 Mar;80(3):036401. doi: 10.1088/1361-6633/aa518f. Epub 2017 Feb 6. PMID: 28166060.

Murray, W. A., & Barnes, W. L. (2007). Plasmonic materials. *Advanced Materials*, *19*(22), 3771–3782. https://doi.org/10.1002/adma.200700678

Park, W. (2014). Optical interactions in plasmonic nanostructures. *Nano Convergence*, *1*(1), 1–27. https://doi.org/10.1186/s40580-014-0002-x

Pendry, J. B. (n.d.). *Metamaterials and the Control of Electromagnetic Fields*. 1–11.

Peng, S., McMahon, J. M., Schatz, G. C., Gray, S. K., & Sun, Y. (2010). Reversing the size-dependence of surface plasmon resonances. *Proceedings of the National Academy of Sciences*, *107*(33), 14530–14534. https://doi.org/10.1073/pnas.1007524107

Reichelt, M., Koch, S. W., Krasavin, A. V., Moloney, J. V., Schwanecke, A. S., Stroucken, T., … Zheludev, N. I. (2006). Broken enantiomeric symmetry for electromagnetic waves interacting with planar chiral nanostructures. *Applied Physics B: Lasers and Optics*, *84*(1–2), 97–101. https://doi.org/10.1007/s00340-006-2211-4

Rodier, M. (2019). *Plasmonic spectroscopy of biomacromolecules with chiral metamaterial*. (July).

Schäferling, M., Dregely, D., Hentschel, M., & Giessen, H. (2012). Tailoring enhanced optical chirality: Design principles for chiral plasmonic nanostructures. *Physical Review X*, *2*(3), 1–9. https://doi.org/10.1103/PhysRevX.2.031010

Smart, A. G. (2011). A mirror gives light an extra twist. *Physics Today*, *64*(6), 16–17. https://doi.org/10.1063/1.3603909

Tang, Y., & Cohen, A. E. (2010). *Optical Chirality and Its Interaction with Matter*. *163901*(April), 1–4. https://doi.org/10.1103/PhysRevLett.104.163901

Tullius, R. (2017). RYAN THESIS: High-Throughput Biosensing using Chiral Plasmonic Nanostructures. *PhD Thesis*. Retrieved from http://theses.gla.ac.uk/8657/1/2017tulliusphd.pdf

Tullius, R., Karimullah, A. S., Rodier, M., Fitzpatrick, B., Gadegaard, N., Barron, L. D., … Kadodwala, M. (2015). "superchiral" Spectroscopy: Detection of Protein Higher Order Hierarchical Structure with Chiral Plasmonic Nanostructures. *Journal of the American Chemical Society*, *137*(26), 8380–8383. https://doi.org/10.1021/jacs.5b04806

Wang, B., Zhou, J., Koschny, T., Kafesaki, M., & Soukoulis, C. M. (2009). Chiral metamaterials: Simulations and experiments. *Journal of Optics A: Pure and Applied Optics*, *11*(11). https://doi.org/10.1088/1464-4258/11/11/114003

Zhong, Y., Malagari, S. D., Hamilton, T., & Wasserman, D. (2015). Review of mid-infrared plasmonic materials. *Journal of Nanophotonics*, *9*(1), 093791. https://doi.org/10.1117/1.jnp.9.093791

CHAPTER 2: FABRICATION PROCESS

2.1 INTRODUCTION

The fabrication of metamaterials is a crucial part and of this thesis. Some developments on new fabrication methods and uses for it can be found in (Karimullah et al., 2015), such as the plastic template metamaterials creation process, or the existence of inverse structures, with a solid metal part and a void on top of it. There are different types of fabrication and can be found in (Murray & Barnes, 2007), but here we will centre on the one we used in the JWNC. What are and what is the practical use of plasmonic metamaterials has already been explained before, and this chapter will be centred to explain in detail everything involved in the fabrication of these materials, starting from the bare substrate until we have in our hands the final structures. This involves three different steps: preparation of the substrate, the lithograph use and the subsequent development of the substrate to get the structures. This will be explained both for conductive and non – conductive substrates, discussing their differences and what these imply in the process of fabrication. A good review to read about the nanofabrication and characterisation in detail can be found elsewhere (Fu, Fang, & Xu, 2011).

Specially, we will be interested in fabricating micromaterials that work in the IR. These materials will be bigger than those used in the visible region of light (Tullius et al., 2017) and will be fabricated to have specific properties, as will be explained. They can support plasmonic resonances that are directly dependent on the plane of polarised incident light, as explained in (Wu et al., 2016). The outcome of this is that we can modulate the properties of the resonances by changing the initial properties of the incident light.

There is also explained the process to prepare the designs using different pieces of software, such as L–Edit, Beamer and Belle. L–Edit is used to draw the designs, and Beamer and Belle to convert the design file into a file that the e–beam lithograph VB6 UHR EWF, from the manufacturer Vistec (currently named Raith), can read and understand and therefore write on the previously submitted substrate.

By doing the two processes (the hands-on fabrication and the design), we end up having the desired structures.

2.2 THE PROCESS

As has previously been said, the whole fabrication process is quite complex and can be affected by several factors such as the temperature, which plays a crucial role. Here is a step–by–step explanation of the process.

The points of L – Edit and Beamer/Belle refer to the design and preparation of the structures we want to be written on the substrate. Afterwards, all the steps refer to the substrate preparation and, finally, about getting the structures.

- **L – Edit**

  The program used to design the figures that are to be written is L- Edit. This software enables the user to draw the desired figures and easily modulate their size and pitch, the distance between the centres of two consecutive structures (both in the vertical and horizontal axis). Figure 1 shows the interface of the mentioned program. There is an example of some of the structures designed on that same image, the shurikens 1 micrometre sized and with 1.5 micrometres of the pitch.

  The use of L - Edit is simple: we start by designing one structure (in the shown case, a shuriken). Then, we scale it to the desired size and replicate it the number of times we want in the vertical and horizontal axis to get the array size (in my case, 0.5 by 0.5 centimetres), and with the pitch we want. The pitch is the distance between the centre of one structure to the centre of the following structure, both in the vertical and horizontal axis. In our case, the pitch is a factor of 1.5, meaning that if the structure is of one micrometre, the separation between structures is 0.5 micrometres, meaning that the total pitch is 1.5 micrometres.

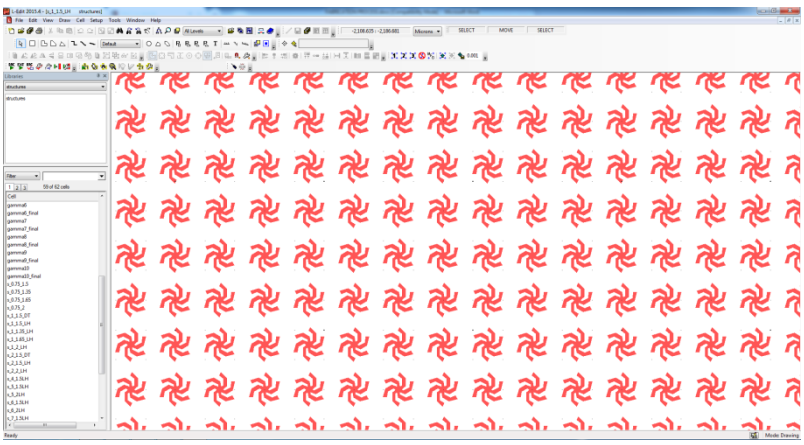

Figure 1. L – Edit interface with 1-micrometre shuriken, pitch 1.5 micrometres

- **Beamer / Belle**

  Once the design is exported from L – Edit as a .gds file, Beamer is used to converting it to a .vep file. This type of file is the one used and read by the software Belle, which is used afterwards. This .vep file is then transferred to the software Belle, which allows us to prepare how the arrays of structures have to be arranged on the substrate and specify what kind of substrate will be used. In Belle, we decide and specify to the e–beam lithograph which doses to use and other settings such as the beam step size and the VRU, as explained afterwards. Figures 2 and 3 are an example of these programs being used. In Figure 2, we see how we, by the use of boxes, tell the program how we want the .vep file to be in terms of geometric properties. In Figure 3, we find the final layout of the structures inside a big square, blue in the Figure, which represents the substrate.

  Figure 2 shows Beamer. We can see how it works with a flowchart: on the first step, we import the .gds file created by L–Edit to then extract the array and finally convert it into a .vep file.

  Figure 3 shows Belle. Belle permits us to organise the arrays on how they should be placed on the substrate when fabricated. There can be seen two arrays of 0.5 by 0.5 centimetres on the image. We can define as well the size and material of the substrate. In our case, we used two by two centimetres silicon substrates and 2.5 by 2.5 centimetres quartz or fluorite windows.

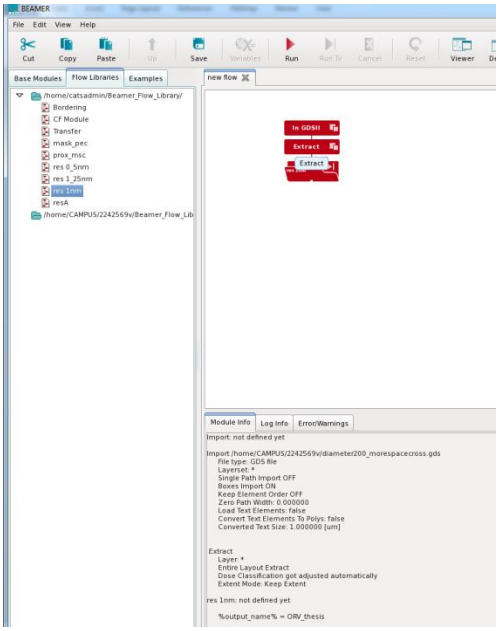

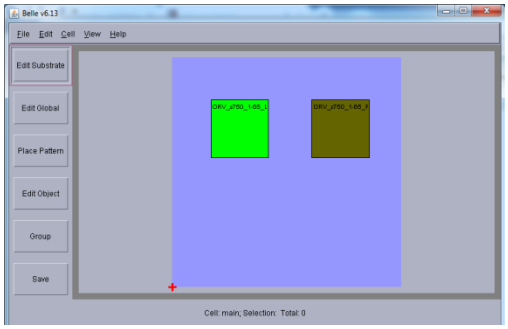

Figure 3. Belle interface with two different arrays

face

- **Substrate preparation**

  The substrate preparation is the same for all cases, with an additional step in the end in a specific case, as will be explained.

  We start by cleaning the substrate. This is done firstly with three organic solvents: acetone, methanol and IPA. This ensures that there are no residues on the sample, as is standard procedure in the JWNC. When the solvents have been applied, we then sonicate the substrate with an ultrasonic water bath. This bath agitates the surface and allows us to eliminate solid particles attached to the substrate. Finally, we plasma clean the substrate for five minutes at 100W. Using the plasma cleaner, we make sure we get rid of any organic residues that might have been left.

  Once the substrate is thoroughly cleaned, we add a layer of resistance to it. This resist has to be of around 300 nanometres of thickness. To achieve so, we use a 2010 8% PMMA at a velocity of 2500 rpm for one minute using a spin – coater. In this label, 2010 is a code regarding the molecular weight of the molecule solved. The percentage refers to the concentration at which the molecule is dissolved. The use of PMMA as a resist is used widely in nanofabrication (Meunier, 2015). Once this is finished, we bake the substrate for 10 minutes at 180 centigrade degrees in order to harden the resist. To check the thickness and make sure it was around 300 nanometres, we used Dektak. This is a stylus profiler: having a tiny and precise tip, it gives us the height profile of the substrate we want to analyse, so we can make sure the height of the resist is correct (Chen, 2015).

  Before placing the substrate in the e – beam lithograph, it is essential for the substrate to be conductive. When using p – doped silicon substrates, they are already conductive. Suppose the substrate is not conductive, as in the cases of using quartz or fluorite windows, after the spin–coating of the resist layer, we have to add a thin layer of 10 nanometres of aluminium. This is done with Plassys, a piece of equipment that evaporates the desired amount of metal homogeneously. The conduciveness of the substrate is vital to avoid charging of this in the lithograph, as will be explained in the next section. Our group had used titanium previously, as this is another metal that can be used (Abdulrahman et al., 2012). Both metals can be used, as they both have the adhesion property we are looking for at this instance.

- **VB6**

  This is an e – beam lithograph tool. It focuses a high energy electron beam onto the substrate, ‘drawing’ the previously submitted design. By doing this, the areas of the resist where the beam has incised change its properties, having a lesser solubility than the non–irradiated resist by the electron beam. This will be important when doing the development, explained after. The process that undergoes an e–beam exposure is quite complex, and it can be found in the second chapter of (Stepanova & Dew, 2014). In this chapter of the reference, there are explained the critical principles of the e – beam lithography, together with a detailed explanation of the interaction between relevant parameters to take into account when using the equipment.

- **Development**

  If the sample has an aluminium layer on top of it, the first thing is to remove it. This can be achieved by using CD26. CD26 is an alkaline, corrosive liquid containing tetramethylammonium hydroxide. We leave the sample in a CD26 bath for 1 minute at room temperature. Then we can proceed to the actual development, using a one minute and a half bath in MIBK 2.5:1 at 25 centigrade degrees. MIBK stands for methyl isobutyl ketone and is a colourless liquid solvent. This ketone dissolves the less soluble resist (the area that has been exposed to the beam), leaving the normal solubility PMMA untouched.

  When this process has finished, the arrays can already be seen, etched on the resist. They are, at this step, holes in the resist.

- **Metallisation**

  We stick 100 nanometres of gold thickness in the structures. To stick the gold on the substrate, we add previously to the gold 10 nanometres of titanium to be the adhesion layer before. This needs to be done because, if not, the gold would not stick properly and would be easily taken off the substrate.

  To add those two different layers of metal, now the adhesion layer and the gold layer, we used Plassys, the piece of equipment that evaporates the metal layers (in our case, 10nm Ti and 100nm Au) homogeneously. The vacuum within Plassys is routinely of the order of 10^{-7} Pa. After the vacuum is achieved, an electric current passes through the metal (Ti and Au), so it evaporates homogenously and gets to the sample, where it reattaches. Thus, we get our sample with a homogeneous layer of metal.

- **Lift-off**

  After the metal has been deposited on the sample, the only thing remaining is to take out all the remaining gold that is not on the structures. To do so and using the fact that this gold is sitting on a layer of resist, not as the one in the structures (which is sitting directly on to the substrate as the resist there has been ripped off when doing the development), we put the sample in an acetone bath at fifty centigrade degrees for two hours. The acetone dissolves the resist, so the gold on top easily comes out. Finally, we are left with a silicon substrate with the gold microstructures on top of it.

  In Figure 4, there is a schematic of the whole process.

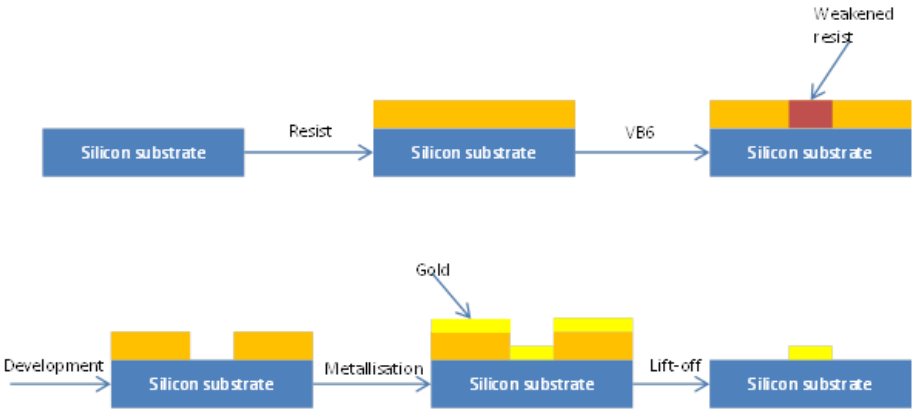

Figure 4. Schematic of the fabrication process.

2.3 FABRICATION AND THE PROXIMITY EFFECT

The proximity effect is the phenomenon that explains why the fabricated structures tend to be wider than expected in the initial design.

When designing and fabricating nanostructures, the main goal is to achieve structures with high resolution, high density, high sensitivity and high reliability (Stepanova & Dew, 2014). A combination of several factors can achieve these results: quality of the beam, resist, substrate and developer, and the process conditions (such as the dose). However, some factors can go against this goal: they relate to the proximity effect.

This happens because of the interactions of the electron beam with the resist and substrate. When we have the proximity effect, it causes the resist outside the designed pattern to receive a non-zero dose. The contributions in these areas are due to electron forward scattering and backscattering. The process related to forward scattering happens because of electron-electron interactions, deflecting the primary electron by a slight angle, broadening the initial electron beam slightly into the area outside the pattern (Tseng, Chen, Chen, & Ma, 2003). The backscattering process originates from the collision with a heavy particle, like a substrate nucleus, and the electron is then scattered on a broader angle into the non-pattern resist. Then, the idea to summarise is that electrons writing a design cause deterioration of the nearby resist.

Other effects can affect the fabrication, such as the collapse of the pattern due to swelling and capillarity forces and fluctuations in the sizes of features (which is known as the line edge roughness) (Stepanova & Dew, 2014). These will not be covered in this work. All these errors result in fabrication differences, between LH and RH structures or between the same structures fabricated at different times. This kind of errors are typical, then, when nanofabricating (Jack, Karimullah, Leyman, et al., 2016), and the goal is to minimise them and always take note of them to understand the results better.

2.4 RESIST OPTIMIZATION

The resists used in the James Watt Nanofabrication centre for our purposes are made of poly (methyl methacrylate) (PMMA for abbreviation). This molecule can be seen in Figure 5.

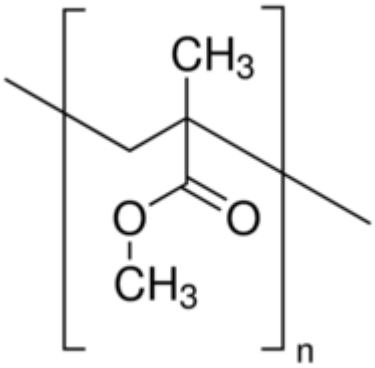

Figure 5. PMMA molecule. Taken from https://www.sigmaaldrich.com/catalog/product/aldrich/445746?lang=en&region=GB

Initially, our group used a bilayer of resist. This was composed of a layer of 2010 8% on top of a layer of 2041 4%. This bilayer had, overall, a thickness of around 300 nanometres. Both layers were spin-coated at a velocity of 5000 rpm. We decided to test if a monolayer could be used instead to simplify the process. To that end, we prepared three samples: one with the already mentioned bilayer, another with a monolayer of 2010 8% PMMA and the last one with a monolayer of 2041 4% PMMA. The monolayers were spin-coated at a velocity of 2500 rpm. All three had the same thickness, measured with Dektak, around 300nm. We submitted the same design in VB6 on all three samples and processed them with the same procedure afterwards. They showed no appreciative differences, meaning that a simple monolayer worked well instead of using a bilayer, as shown in Figure 6. Therefore we decided to use a monolayer of 2010 8% on our fabrication. The gammadions used in this experiment were an old group design, already prepared.

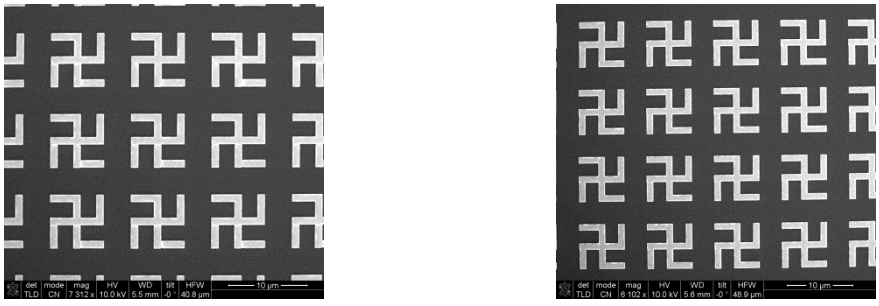

Figure 6. SEM images of the same structures using a substrate with a bilayer (left) or a monolayer 2010 8% (right). There cannot be observed any significant differences. The scale is in both cases around 10 micrometres, being the left image a bit bigger than the right.

2.5 THE DOSE TEST

A dose test is a trial of the electron beam dosage that is needed to fabricate the structures. It is an optimisation process; the goal is to find the best dosage to use is. It is necessary to do this process every time we are fabricating a new structure.

There are three main settings when doing a dose test: the dose, the beam size and the VRU. These are defined below.

- DOSE: the dose refers to the amount of energy per a given area of the sample. It is a number that relates to the number of electrons delivered. The more electrons that are delivered by the e–beam lithograph, the higher the dose.
- BEAM STEP SIZE: the beam step size is the distance by which it steps the beam when filling in a shape. (JWNC, n.d.)
- VRU: the VRU is a multiplier of the beam step size. The following equation relates them.

$$\text{Beam Step Size} = \text{VRU x Resolution}$$

  The resolution is the address grid and represents the accuracy to which the VB6 will place the beam, and thus the accuracy to which it will place a shape (ibid).

A dose test starts by creating a design with several identical arrays, smaller versions of the desired array we want to fabricate. We assign each one with a different dose, all around the dose we believe best. Figure 7.1 shows a dose test example, with doses ranging from 100 to 500. The image is taken from the Belle software set up, a program explained previously in this chapter. Image 7.2 shows the dose finally used, of 500. The beam step size was 64na, and the VRU was 25.

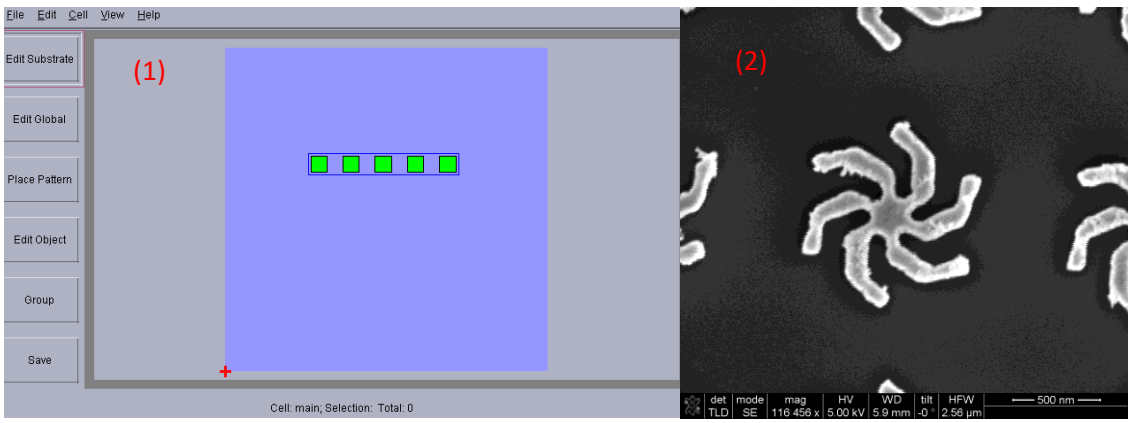

Figure 7. 7.1 shows an image of the Belle set up to do the dose test with shurikens 1 micrometre sized. 7.2 shows an SEM image with the dose that we finally went with, of 500.

2.6 SEM

Scanning Electron Microscope, SEM allows us to see structures in the micro and nanoscale, otherwise impossible to characterise with optical techniques. This spectrometer gives us high-resolution images by scanning an electron beam focussed on the sample's surface being analysed. The spectrometer needs to work under vacuum conditions.

The instrument used in this work, the FEI Nova 630 NanoSEM, is capable of seeing features up to 5 – 10 nm. When the beam arrives at the surface, it penetrates the sample to a depth of a few microns. The signal we receive generated from the primary electron beam-sample interaction depends directly on the depth at which this interaction happens. However, the primary electron beam collides inelastically with the substrate at the surface, which results in the ionisation of the constituent atoms. This phenomenon generates secondary electrons, which have energy significantly lower than that of the primary beam. Electrons can also collide elastically, in which case they are known as backscattered electrons. This process occurs at greater depths in the sample, and a factor that is important here is the density of the sample. This gives us more imperfect resolution images, the reason why secondary electrons is the method of analysis customarily used.

For the sample to provide high-resolution images in an SEM spectrometer, it has to be conductive and avoid such a build-up of charge in small areas, leading to distortion in the structure itself a process which can be similar to the proximity effect.

The resolution limit of the FEI Nova NanoSEM 630 is ~5 nm at ten keV, well below the size of our structures.

2.7 THE STRUCTURES

Metamaterials with plasmonic properties can be easily fabricated using the methods presented here. The different architectures can be constructed because the size of the metal blocks can be tuned over multiple length scales (Henzie, Lee, Lee, Hasan, & Odom, 2009).

We fabricated several different structures, in order to have a significant scope of possible uses, until finally deciding on which ones to use. Other works of Prof. Kadodwala group have worked with several other structures for this and other uses(Paterson, Karimullah, Williamson, Kadodwala, & MacLaren, 2015)(Jack, Karimullah, Tullius, et al., 2016). Here will be a brief description of the processes to get the different structures we initially worked with and explained is the reason for our final decision. From here on, every time we refer to a shuriken size in micrometres, it will mean the distance edge to edge of the structure in a straight line, unless specified otherwise.

When we first planned the Mid IR project, we knew that the structures needed to be bigger than when working in the visible range (in that range, the group works with structures with a size of around 400 nm). To that end, we designed structures ranging from 10 to 5 micrometres. We prepared shurikens and gammadions. These structures are chiral and had been previously used in the visible range with good results.

We designed both shurikens and gammadions, but we finally went for the shurikens in order to simplify the project. Of these, we fabricated the 9µm and 6µm (having done the correspondent dose test previously to find the most suitable dose values). Nevertheless, we saw no plasmonic peak. That led us to think that we were fabricating too large structures, even for the Mid IR region we were working at. We then prepared smaller structures, that is, of 4µm and 2µm. With these, we did see a plasmonic peak. With the shurikens of 4µm, we only saw half a peak, confirming that the peak was, indeed, much more to the left side of the region than the spectrometer was designed to observe (to higher wavelengths; lower wavenumbers).

The 2µm shuriken, though, gave us a clear plasmonic peak, around 800 wavenumbers (wavelength = 12.5 micrometres). That confirmed definitely that to work in the Mid IR, we needed, in fact, bigger shurikens than the ones we use on the visible (around 400nm of size), but not as big as we initially thought. All the spectra for these different sizes can be found in Figures 8.1 to 8.4.

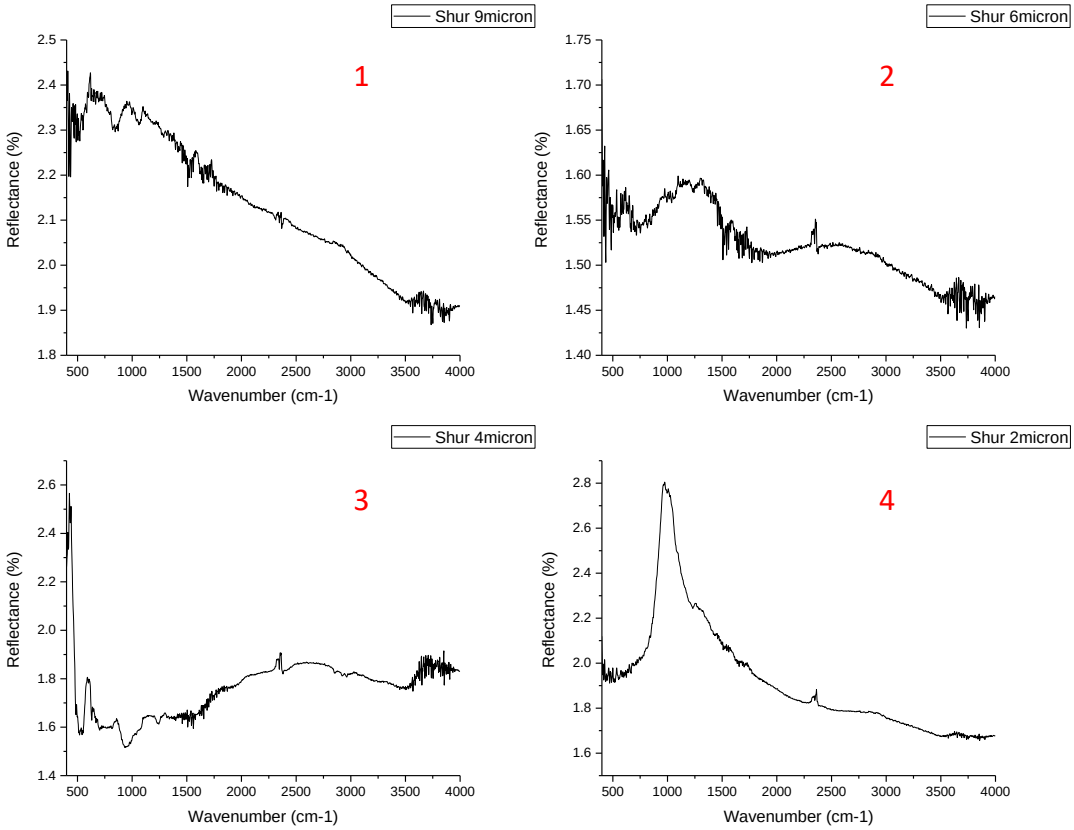

Figure 8. Spectra of the different fabricated shurikens. (1) is the 9 micrometres shuriken, (2) the 6 micrometres shuriken, (3) the 4 micrometres shuriken and (4) the 2 micrometres shuriken.

As can be observed, for (1) and (2), there is no definite peak, but only noise (on the edges, water, and the noise at around 2400 wavenumbers is originated by the CO_2). The great inclination of (1) is due to the silicon background.

At (3), however, we can appreciate the peak appearing on the left edge of the graph, at precisely 400 wavenumbers. This peak becomes clear at (4), the shuriken sized 2 micrometres.

Because the peak of the 2µm shuriken is very close to the edge and, therefore, has more noise, we fabricated (using the same dose, as the size was very similar and we did not expect any differences due to the dose settings) shurikens of 1µm. This gave a prominent and definite peak at around 1500-1600 wavenumbers (wavelength = 6.25 micrometres). In Figure 9, an SEM picture of this first 1µm shuriken can be seen, together with the spectrum collected.

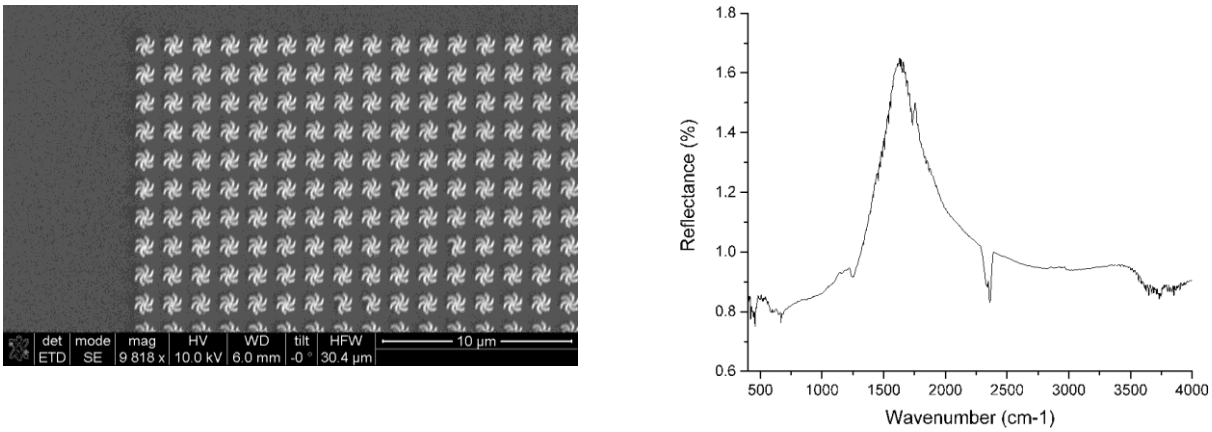

Figure 9. SEM image of shurikens of 1-micrometre size and its correspondent reflectance spectra, at around 1500 cm^{-1}.

This spectrum now showed an evident and definite peak and was far away from the edge enough not to get affected by the noise IR spectrum have at the limit.

After doing some experiments with the 1μm shuriken, we designed and fabricated a shuriken that was 0.75μm in size. This gave us a plasmonic peak of around 2300 wavenumbers (wavelength = 2.73 micrometres). As shown in Figure 10, the spectrum collected from this shuriken showed a much broader peak. This is because of the exponential nature of the wavenumber scale. We will see that, as well, the results are affected and can be explained because of this exact reason.

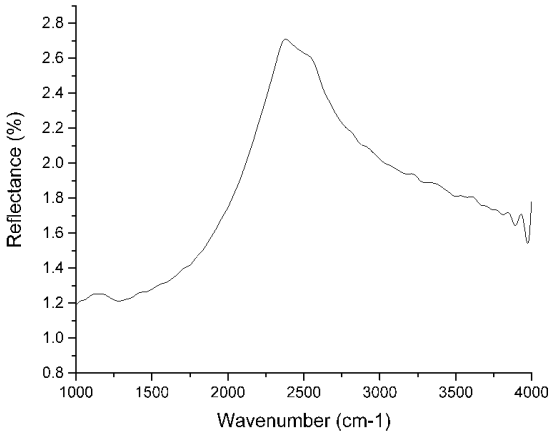

Figure 10. Example of the spectrum collected of the shuriken 0.75 micrometre sized, with a broad plasmonic peak around 2300 cm^{-1}.

As said previously, we got as well structures that were of a 2μm size. These showed a thinner plasmonic peak around 800 wavenumbers (wavelength = 7.85 micrometres), as can be seen in Figure 8.4. Taking into consideration the three different plasmonic peaks from the three different structures (0.75μm, 1μm and 2μm), we clearly observe how the plasmonic peak position is dependent on the shuriken structure size.

The pitch used in all structures was of a factor of 1.5 in respect to the shuriken size. The pitches, then, could be easily calculated and are tabulated in Table 1. SEM images for the shurikens fabricated can be found in Figure 11.

SHURIKEN SIZE	THEORETICAL PITCH	ACTUAL PITCH (measured on an SEM image)
0.75 μm	1.125 μm	1.134 μm
1 μm	1.5 μm	1.489 μm
2 μm	3 μm	2.974 μm

Table 1. Tabulated is the theoretical and actual pitch of the structures fabricated.

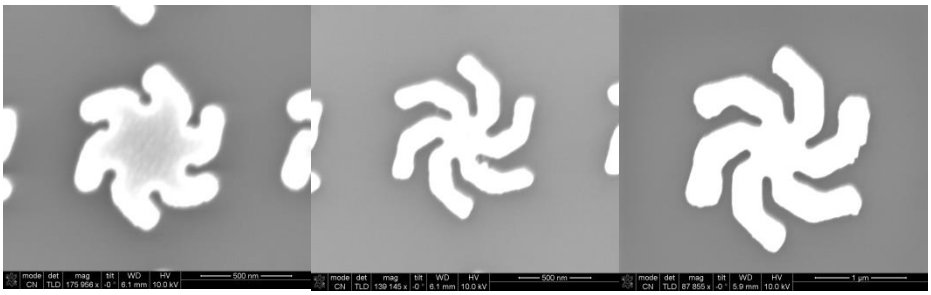

Figure 11. SEM images of the three different sized shurikens fabricated. 1, 0.75 μm. 2, 1 μm. 3, 2 μm. Note that, in the image corresponding to the shuriken of 2 μm, the neighbouring shurikens are not seen to have a clear image of the structure itself.

We chose to work with the shurikens one micrometre sized, the reason being that these shurikens showed a resonance coincident with the amide resonances. As explained in previous chapters, this region was the one we were interested in studying, so the selected shurikens fitted perfectly with our experimental interest. We as well designed the shurikens with a pitch of factor 2 (so designing a space that was of the same width as the structures). In this case, the dose used and all the settings were the same. When deciding which structures and designs to use, we decided on pitch 1.5 for all the structures we would use. This was because the closer the structures are, the stronger the interaction we were expecting to see.

2.8 AXIS OF THE SHURIKENS

One important point to make about the structures is the defining axis of it because this gives us information on the symmetry of the structure. They are known as the long and short axis, as shown in Figure 12. We call the long axis the axis that covers more structure from end to end, and the short axis the one that covers less structure from end to end. In Figure 11, we can see how the red line (long axis) goes from the limit of one arm to the limit of the opposite arm, while the blue line (short axis) cuts the arm at the edge at the central point approximately, giving it less route along the arm of the structure.

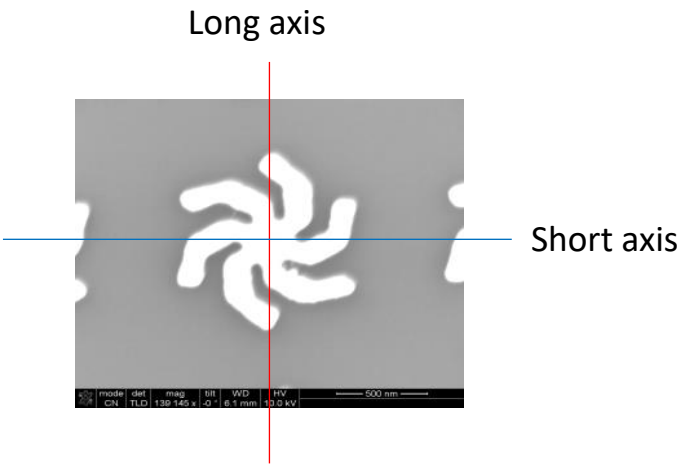

Figure 12. SEM image of an example shuriken. The blue and red lines represent the short and long axis, respectively.

When working with plane polarised light, we would expect to see different behaviour regarding if we are placing the structure with one axis along with the light or the other (Adato et al., 2009). Because we will be working with non-polarized light, we will not take into account this effect.

2.9 BIBLIOGRAPHY

Abdulrahman, N. A., Fan, Z., Tonooka, T., Kelly, S. M., Gadegaard, N., Hendry, E., … Kadodwala, M. (2012). Induced chirality through electromagnetic coupling between chiral molecular layers and plasmonic nanostructures. *Nano Letters*, *12*(2), 977–983. https://doi.org/10.1021/nl204055r

Adato, R., Yanik, A. A., Amsden, J. J., Kaplan, D. L., Omenetto, F. G., Hong, M. K., … Altug, H. (2009). Ultra-sensitive vibrational spectroscopy of protein monolayers with plasmonic nanoantenna arrays. *Proceedings of the National Academy of Sciences*, *106*(46), 19227–19232. https://doi.org/10.1073/pnas.0907459106

Chen, Y. (2015). Nanofabrication by electron beam lithography and its applications: A review. *Microelectronic Engineering*, *135*, 57–72. https://doi.org/10.1016/j.mee.2015.02.042

Fu, Y., Fang, F., & Xu, Z. (2011). Nanofabrication and Characterisation of Plasmonic Structures. *Nanofabrication*. https://doi.org/10.5772/26612

Henzie, J., Lee, J., Lee, M. H., Hasan, W., & Odom, T. W. (2009). Nanofabrication of Plasmonic Structures. *Annual Review of Physical Chemistry*, *60*(1), 147–165. https://doi.org/10.1146/annurev.physchem.040808.090352

Jack, C., Karimullah, A. S., Leyman, R., Tullius, R., Rotello, V. M., Cooke, G., … Kadodwala, M. (2016). Biomacromolecular Stereostructure Mediates Mode Hybridization in Chiral Plasmonic Nanostructures. *Nano Letters*, *16*(9), 5806–5814. https://doi.org/10.1021/acs.nanolett.6b02549

Jack, C., Karimullah, A. S., Tullius, R., Khorashad, L. K., Rodier, M., Fitzpatrick, B., … Kadodwala, M. (2016). Spatial control of chemical processes on nanostructures through nano-localised water heating. *Nature Communications*, *7*, 1–8. https://doi.org/10.1038/ncomms10946

JWNC. (n.d.). *Resolution, VRU and Beam Step Size on the VB6*.

Karimullah, A. S., Jack, C., Tullius, R., Rotello, V. M., Cooke, G., Gadegaard, N., … Kadodwala, M. (2015). Disposable Plasmonics: Plastic Templated Plasmonic Metamaterials with Tunable Chirality. *Advanced Materials*, *27*(37), 5610–5616. https://doi.org/10.1002/adma.201501816

Meunier, M. (2015). *off process Electron beam lithography using a PMMA / P (MMA 8 . 5 MAA) bilayer for negative tone lift-off process*. *061602*(May 2016). https://doi.org/10.1116/1.4935129

Murray, W. A., & Barnes, W. L. (2007). Plasmonic materials. *Advanced Materials*, *19*(22), 3771–3782. https://doi.org/10.1002/adma.200700678

Paterson, G. W., Karimullah, A., Williamson, S. D. R., Kadodwala, M., & MacLaren, D. A. (2015). Electron energy loss spectroscopy of a chiral plasmonic structure. *Journal of Physics: Conference Series*, *644*(1). https://doi.org/10.1088/1742-6596/644/1/012005

Stepanova, M., & Dew, S. (2014). Nanofabrication: Techniques and principles. In *Nanofabrication: Techniques and Principles* (Vol. 9783709104). https://doi.org/10.1007/978-3-7091-0424-8

Tseng, A. A., Chen, K., Chen, C. D., & Ma, K. J. (2003). Electron beam lithography in nanoscale fabrication: Recent development. *IEEE Transactions on Electronics Packaging Manufacturing*, *26*(2), 141–149. https://doi.org/10.1109/TEPM.2003.817714

Tullius, R., Platt, G. W., Khosravi Khorashad, L., Gadegaard, N., Lapthorn, A. J., Rotello, V. M., … Kadodwala, M. (2017). Superchiral Plasmonic Phase Sensitivity for Fingerprinting of Protein Interface Structure. *ACS Nano*, *11*(12), 12049–12056. https://doi.org/10.1021/acsnano.7b04698

Wu, W., Yu, Z., Wang, S., Williams, R. S., Liu, Y., Sun, C., … Williams, R. S. (2016). *Midinfrared metamaterials fabricated by nanoimprint lithography Midinfrared metamaterials fabricated by nanoimprint lithography*. *063107*(2007), 1–4. https://doi.org/10.1063/1.2450651

CHAPTER 3: EXPERIMENTAL PROCESS

3.1 INTRODUCTION

This chapter will explain the experimental setup and process followed to get the results explained later in this work: SPLITTING ANGLE DEPENDENCE.

Understanding how the experiment was prepared and carried is crucial and relevant to understanding later the results. That is why an entire chapter is dedicated to the experimental process.

We will start by studying the instrument used, the Fourier Transform Infrared Spectrometer, and how we optimized it to have the best settings possible for our experimental goals. In the study section, we will be analyzing all the essential parts of the instrument and the basics of its function and operation. It will justify the importance of using this kind of spectrometer. When discussing the optimization we performed on the spectrometer, we will discuss each possible setting and why we finally decided on which one. These settings go from the aperture we work with to purge the sample chamber and decide the gain or scanner velocity. All of the final settings will be justified.

We will then talk about the experimental set up itself. There, will be underlined the importance of the alignment of our substrate, or at which angle in respect of the incident beam of light the sample was placed. Because we will be looking at features such as chirality and symmetry, we always have to make sure that we have a properly aligned substrate to get the results of the structures as we want them. The experimental procedure will be explained both for when working in the air, meaning that we do not have anything adsorbed on the substrate and we are working in an air medium or working once the adsorbed protein is on top of the gold structure.

Finally, we will reflect on Reflectance spectroscopy and how we use it and its importance in this experimental work.

3.2 THE FTIR

Infrared light gives us information about the chemical bonds of matter and is a valuable tool for studying the structure of proteins, especially of their secondary structure (Garidel & Schott, 2006). The reason is that the light from this region excites and is absorbed by the chemical bonds, as long as when vibrating, they change their dipole moment. This fact gives us information about the structure of the biomolecule, usually a protein, being analyzed. Specifically, it can give us information about the amide resonances discussed in the THEORY chapter, and this, identifying the amide resonances (Kong & Yu, 2007), will be one of the things that will interest us most.

The Fourier Transform Infrared (FTIR) spectroscopy brought with it significant improvements in the quality of spectra (ibid), and thus this is the technique that will be used here. All absorption spectroscopy (amongst them, FTIR, but also ultraviolet-visible spectroscopy, the one mainly used by our group) have the same goal: to measure how the intensity of light changes and behaves after getting in touch with a sample from the initial incident light. Mainly, to do this, most spectrometers shine a monochromatic beam of light (with one just wavelength) directly at the sample, and then a detector collects the outcoming beam.

The spectrometer we used in the experiments presented in this work is a Bruker Tensor 27 FTIR for the Mid Infrared region. We performed reflectance measurements, and to that end, used a reflectance mount. The exact procedure to make these experiments will be explained in the following sections.

The FTIR spectrometer does not work the usual way spectrometers do. Instead of shining a monochromatic beam at the sample, FTIR shines a beam with several frequencies at once and measures how much of this multifrequency beam is absorbed by the sample. After doing that, the beam changes to different frequencies to give us a second data point. This same process will be done several times rapidly. After this is done, a computer algorithm (the Fourier transform) takes all the data collected and works backwards to deduce the sample absorbs' wavelengths. We start with the raw data, called an interferogram, and we get the final spectra with all the wavelengths analyzed (Skoog, 1992).

This type of spectrometer consists of an interferometer that modulates the light to reduce the order of the frequencies measured in the detector. This piece of equipment divides the beam of light from the source into two components using a beam splitter (an optic material that transmits approximately 50% of light and reflects the other 50%). Those two beams reflect onto two different mirrors (typically, one of the movable, so the distance the beam of light runs changes respect the other, but in this case, both of them are movable in order to occupy less space) perpendicular to the original beam. This creates a pattern of interference, a combined wave that results from two waves, has constructive and destructive interference. This is called a Michelson interferometer (Barth, 2007). Figure 1 shows a schematic of how the Michelson interferometer is.

The light that arrives at the detector has a lesser frequency than the one initially emitted. Both frequencies (original and detected) are directly proportional, related by a very small number (in the order of 10-100, depending on the wavelength of the light), making the final frequency much smaller, and therefore, able to be detected by the detector. Therefore, instead of measuring the light absorption for each frequency, this spectrometer, as a dispersive instrument, measures it for each mirror position and then obtains the final frequency spectrum through a Fourier transform (Skoog, 1992).

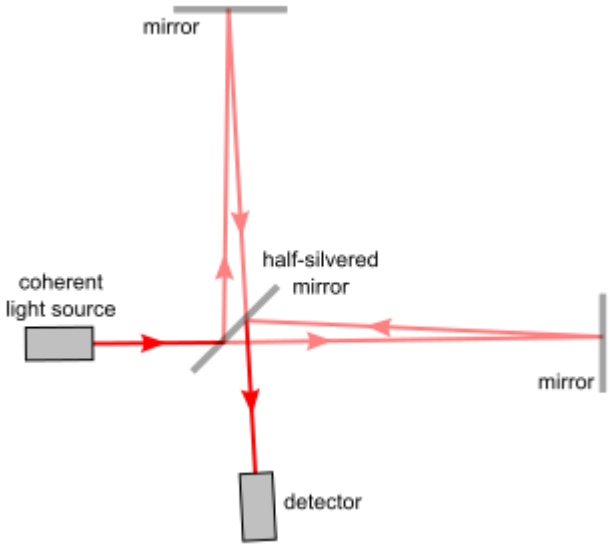

Figure 1. Michelson interferometer. It was taken from Wikipedia.

The FTIR has several setting options to change to get the desired experiment. Firstly, we will discuss the source setting used. The source of the FTIR is one already in the spectrometer for everyday use, a Globar lamp. It is a thermal lamp based on a thin silicon carbide rod (5 to 10 mm) and between 20 to 50 mm in length. This rod is then electrically heated up to 1,000 to 1,650 °C. When combined with an interference filter, it emits light in the IR region. Before arriving at the sample, this beam generated by the source passes through a beamsplitter, which, in our case, is a KBr beamsplitter. Despite the availability of several optical filters, we chose not to use any because we needed all the light coming from the source to get to the sample. Another essential variable to select is the aperture.

The aperture setting relates directly to the beam size we will see onto the sample. Therefore, it is crucial to find the aperture that gives a beam the same size as our arrays in order for it to be entirely covered by the light. In our case, the correct aperture was 3 millimetres. Regarding the detector used, the FTIR can operate with different detectors. The one we used is a deuterated lanthanum α alanine doped tri-glycine sulphate (DLaTGS). This detector is pyroelectric, a thermal detector. They create an electric signal due to a change in temperature in their chip, caused by light absorption. DLaTGS is a pyroelectric material, and so it can be

used as such. It has a high level of performance. It is the most common detector when working with mid-IR spectroscopy. The scanner velocity is the velocity at which the FTIR works and does the scans. The best scanning velocity depends on the detector. We used the most negligible scanner velocity possible, which was 2.2 kHz. By this, the scans took longer but were of better quality. Finally, we can as well set the desired gain. The gain measures the ability of a system to increase the power of a signal from the input to the output port. We have two different kinds of gains in our spectrometer we can module. We can change both the sample and the background measurements gain.

3.3 REFLECTANCE SPECTROSCOPY

As has been explained in the first section of this chapter, we are working with an FTIR spectrometer, and as will be seen, we will be using a Reflectance measurement mount. In this section, we will take a closer look to what is the basis for Reflectance measurements.

When a beam of incident light of any type arrives at a substrate, it can undergo different processes: it can transmit, be absorbed or reflected. All these effects combined amount to the intensity of the initial light we are working with, as in equation 17:

$$I = I_t + I_{ab} + I_r \quad (\text{eq. } 17)$$

Because reflectance depends on the wavelength and the polarisation of light, we will be changing both these items. The wavelength we chose by deciding to work in the Mid – IR. The reason for this has already been mentioned: it will be helpful when analyzing amide vibrations. The polarisation, we will be taking measurements at both axes of polarisation: x and y.

This is a kind of spectra that can be taken from the gold microstructures used here (Tullius, 2017). The angle of incidence is the one we are experimenting with, being it 15, 25 or 40 degrees. Reflectance happens in our experiments when some of the incident light goes back at an angle from the irradiated structures. The angle it comes back is equal to the angle of incidence. A diagram of this can be found in Figure 2.

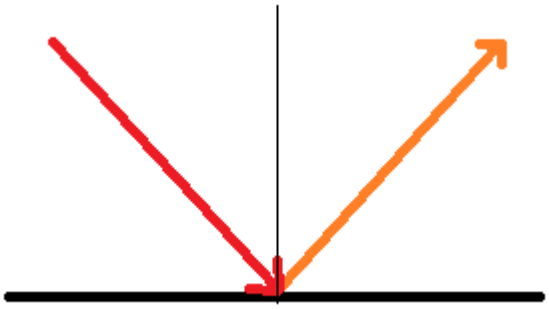

Figure 2. The diagram shows the angles of incidence, the angle between red beam and normal black line to the surface, and the angle of reflection, the angle between the orange and the normal.

The mirror used to collect the reflected beam of light was then placed at the same angle as the mirror used to guide the initial beam to collect as much light as possible. This mirror sends it to the detector after the light is collected.

The spectrometer automatically subtracts the background from the sampled signal, which is why the background measurement has to be taken first.

To put it simply, and taking into account that the used instrument works with Fourier transforms, which makes it all more complex, the reflectance can be mathematically understood as follows in equation 18:

$$\text{Relative Reflectance} = \frac{I_{microstructure}}{I_{background}} \quad (\text{eq. } 18)$$

We will be taking Reflectance measurements in the experiments discussed in the last chapter of the current work because they are fit to show the differential behaviour between LH and RH structures we were looking to see, but as well this kind of measurements are simple and easy to work with, avoiding more complications in the experimental setup.

3.4 THE FTIR, OPTIMISATION

However, before using it, we needed to set it up and optimize it. We first optimized all the possible settings that the software demanded us to find which conditions the spectrometer functioned best. We then checked that purging the chamber made a difference in the results. Finally, we optimized the experimental setup to find the optimal position of all parts for our experiments.

One important thing was to check that the light beam was not polarised. In theory, the spectrometer itself did not polarise the light. Source, beamsplitter and interferometer were non-polarized. However, the windows between the source and the sample chamber and sample chamber and detector were of sodium chloride, NaCl, and these kinds of windows are a bit polarising. A schematic of the spectrometer can be found in Figure 1. So, the first window light would cross between the light source and sample chamber, would polarise the light. To know precisely the amount of polarisation we would have in our experiments, we checked it by rotating one window in respect of the other, from 0^o to 90^o. First, we did this without any mount or sample in the chamber. The starting point was with both windows aligned at 0^o and then rotating the window between the sample chamber and detector at different angles. Results of this can be found in Table 1. The signal intensity corresponds to that of the interferometer.

As can be observed, the intensity does decrease when rotating the mirrors, meaning that there is indeed a bit of polarisation. We calculated the exact amount of this polarisation and the efficiency of the windows as a polarising device.

ANGLE	SIGNAL INTENSITY (approx. values)
0^o	1120
30^o	1000
45^o	970
60^o	940
90^o	910

Table 1. Results of the signal intensity with angle variation. The decrease observed is because of a slight polarisation.

From the table, we make the following calculations, equations 19 and 20:

$$\text{Light lost} = 1120 - 910 = 210 \quad (\text{eq. } 19)$$

$$\text{Percentage of light lost: } \frac{210}{1120} * 100 = 18.75\% \quad (\text{eq. } 20)$$

The window efficiency as a polarising device can be calculated by applying Malus law for polarisers, equation 21:

$$I = I_0 \cdot (\cos\Theta)^2 \quad (\text{eq. } 21)$$

As the light initially comes non-polarised, as it goes through the first window acting as a polariser with an α efficiency, it has an average of all the angles the light comes in at and can be deduced as follows in equation 22:

$$I = \alpha I_0 \int_0^{2\pi} (\cos\Theta)^2 dx /_{2\pi} = \frac{\alpha I_0}{2\pi} \int_0^{2\pi} \frac{1}{2}\cos(2x) + \frac{1}{2} dx = \frac{\alpha I_0}{2\pi}\left(\int_0^{2\pi} \frac{1}{2}\cos(2x) + \int_0^{2\pi} \frac{1}{2} dx\right)$$
$$= \frac{\alpha I_0}{2\pi}\left(\frac{1}{4}\int_0^{2\pi} 2\cos(2x) + \int_0^{2\pi} \frac{1}{2} dx\right) = \frac{\alpha I_0}{2\pi}\left(\frac{1}{4}\int_0^{2\pi} 2\cos(2x) + \int_0^{2\pi} \frac{1}{2} dx\right)$$
$$= \frac{\alpha I_0}{2\pi}\frac{1}{2}2\pi = \frac{\alpha I_0}{2} \quad (\text{eq. } 22)$$

Then, as the light goes through the first slightly polarising window, it is the resulting equation 23:

$$I_1' = \frac{\alpha}{2} I_0 \quad (\text{eq. } 23)$$

The rest of the light intensity remains non-polarised, equation 24:

$$I_1'' = \left(1 - \frac{\alpha}{2}\right) I_0 \quad (\text{eq. } 24)$$

We repeated this same experiment, rotating the windows but with the reflectance mount and a sample in place, to see whether this affected the polarisation. Table 2 shows the results for this setting.

ANGLE	SIGNAL INTENSITY (approx. values)
0º	20
30º	20
45º	20
60º	20
90º	20

Table 2. Results of the signal intensity with angle variation and the sample put. The magnitude of the intensity is very small and unchanging.

So, as can be seen, there is no polarisation at all once the sample is in place that is meaningful. Hence, we consider that we do not have any practical polarisation for our experiments.

To optimize each one of the set parameters of the FTIR, we took measurements for all of them at all the different options. Here is a recollection of these experiments and the conclusions we arrived at, which are the best parameters to use.

- **APERTURE SETTING**: our arrays are (both the LH and RH) 0.5cm by 0.5cm squares. The aperture that best matches the beam to this array is 3mm, and this is, then, the aperture that we will be using in all of the experiments. To know which aperture we would use, we just put the substrate under the beam and changed the aperture setting until finding one that was the desired size. We have to note here that the beam is circular, whereas, as said, the array is a square. This meant that we would always get some silicon signal from the substrate (Basu, Lee, & Zhang, 2009) due to the difference in shape between array and light beam.

- **SCANNER VELOCITY**: 2.2 kHz for the scanner velocity, the spectrometer gave us several options, ranging from 10 kHz to 2.2 kHz. We selected to use the latter, as the slower the scans are made, the better results, with less noise, we would get.

After all, settings were optimized, we checked if purging the chamber improved the results. The purging was made with dry air in order to reduce to its minimal content of gaseous water in the chamber atmosphere. As can be observed in Figure 3, it did improve the results, even if it was not yet perfect, as there is still some noise due to some residual water that we could not get rid of. The content of carbon dioxide varied from background to sample measurements. That is the reason why we could see a peak in most cases because of this compound. This proves again that the purging is not perfect.

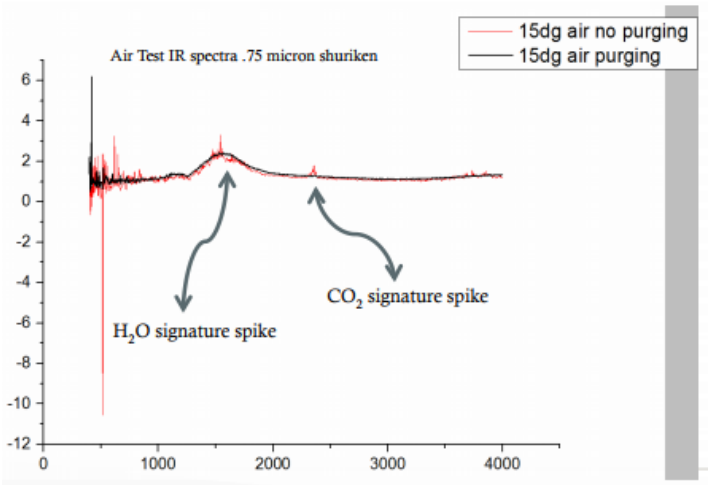

Figure 3. Compared spectra showing the improvements in the resultant spectra by purging the chamber.

Once the FTIR settings were optimized, we searched which way was best to do the experiment.

As explained in the section before, the FTIR reflectance mount uses a mirror system in order to direct the light on to the sample. From an angle of 15º to 90º, these two mirrors are movable in respect of the vertical, perpendicular to the sample. In theory, they would be able to move from 0º to 90º, but because of the own size of the mirrors, it is not possible to put both of them at an angle minor of 15º at the same time, being 15 the minimum possible for both of them at one exact moment.

To find the angle at which the experiment gave us the best results, this is, the highest intensity possible and the lesser signal to noise ratio, we repeated the same kind of measurement over all the angles, in intervals of 5º up to 60º, and then from 10º to 10º up until reaching the maximum, 90º.

We found that we obtained the best results (highest intensity, as well as good shape resolution of the spectrum) between the angles of 15 and 50 degrees. Nevertheless, as well, we noticed something else: the peak position that we were getting was shifting with the angle. This meant angle dependence for the peak position. We investigated further this phenomenon, as will be explained in the results chapter.

3.5 EXPERIMENTAL SET UP AND PROCEDURE IN AIR

Here, we use the term 'in the air', meaning that the sample is laying on a dry medium, sitting on the mount, as will be explained, without anything else than air on top of it.

The FTIR, as shown in Figure 1 and explained in the previous sections, has a sample compartment. In this, we can select which mount to use, being easy to remove one and put another. The piece used in all experiments is that of reflectance. A more detailed image of this piece in Figure 4. We 3D printed a new piece to put the sample on top that fitted the reflectance mount, schematics shown in Figure 5, and the green piece in Figure 3. The old one was not working for us because of how the sample was put. It used a clamp system to hold in position the sample, which made it very difficult to remove it and put it again, making sure that it was perfectly flat and that it was not scratched or damaged in any way.

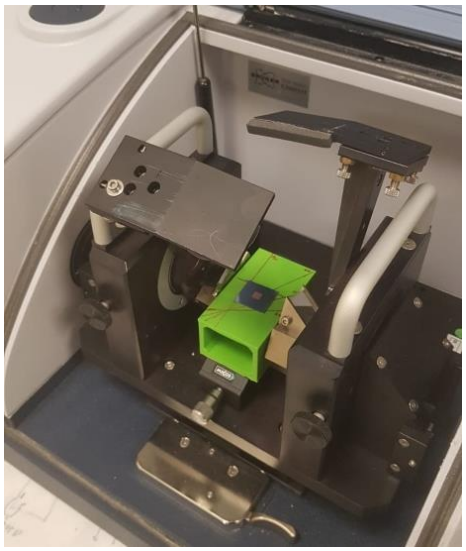

Figure 4. Image of the experimental set up used in the reflectance experiments. The green part is the 3D printed mount specifically designed for the experiments and can be seen as well red lines drawn in order to align the sample properly.

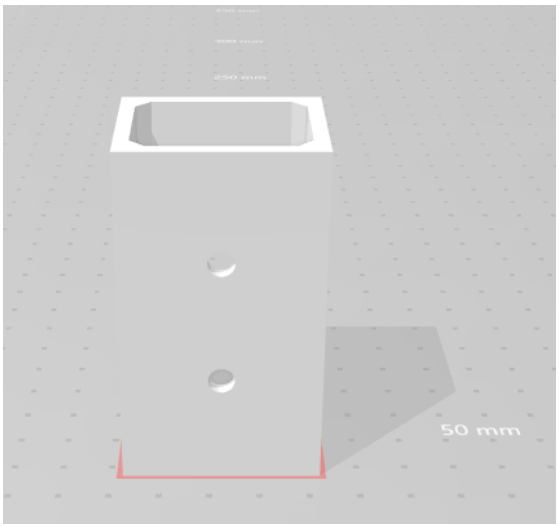

Figure 5. Schematics of the piece we 3D printed in order to place the sample on top, designed by Dr Affar Karimullah.

We used the same background to measure reflectance spectra at the same angle at different sample positions. The background in all cases was cleaned and bare silicon, without structures on it. This was done with the optimized settings explained before and during 10 minutes (with a 30 minutes purge done before), which were 161 measurements taken. After, the FTIR normalized all different spectra taken of one exact set of angle concerning this silicon background. In the paper (Tame et al., 2013), they follow a similar process, but their background with which they normalize is a piece of bare glass.

To do each one of the measurements, we put the sample with the arrays facing up and making sure we had the desired alignment with the lines we previously draw on the mount at different position angles to act as a reference. These lines can be seen in Figure 3, in red. We then closed the lid and waited for a 30-minute purge with dry air. This was done in order to get rid of as much vapour water as possible in the atmosphere and to normalize and make constant the concentration of different gases present.

Once the background was taken, we proceeded with the sample measurements. We moved the substrate in order to place the structured array just so the beam completely covered it. Because the beam was circular, and the array was a square, we always had as well a little bit of the background silicon. Any signal coming from it would be removed by the background experiment taken previously. When we had made sure that the array was directly under the beam, we closed the lit and purged, same as we did with the background. After the 30 minute purge, we started a 30-minute measurement, 483 measurements taken.

Once this was done, we moved to measure the next experiment: it is doing a different angle or using a different alignment.

3.6 EXPERIMENTAL SET UP AND PROCEDURE WITH CYSTEINE

When doing experiments with a biomolecule, as we will be using the amino acid cysteine in the last chapter of this work, we need to add some steps in the section described in the section before the experimental setup procedure in air. The main difference in respect to this experiment is that an existent monolayer of cysteine will be adsorbed on top of the gold microstructures.

Cysteine is an enantiomeric molecule with D and L versions of itself. It has as well a sulphur atom in its structure, a necessary condition for the amino acid to adsorb on the gold surface of the structure. A representation of the amino acid structure can be found in Figure 6. Other works have already studied this amino acid (Haes, Hall, Chang, Klein, & Van Duyne, 2004).

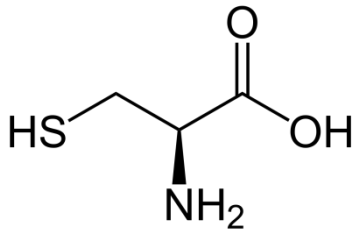

Figure 6. Schematic of the cysteine amino acid structure. As can be seen, it has a sulphur atom at the end of a chain, a condition necessary in order to adsorb onto a gold surface.

We start by already having the clean sample spectrum with its background, by the process just described previously. To add the aminoacid monolayer adsorbed onto the shuriken array, we leave overnight the substrate in a 1mM cysteine solution that we previously prepared by dissolving 0.034 grams of the desired enantiomer, or the racemic, of cysteine in 30mL of distilled water. The reason for leaving it all night long is to assure the complete adsorption of the aminoacid onto the gold structure, so we end up having the complete monolayer of the biomolecule, which we need to do the following experimentation.

The procedure to take Reflectance measurements of the structure, now with protein adsorbed, is the same as the one with the cleaned structure and is similar to those used in other references such as (Tullius et al., 2015). First, we have to take the background signal. We did so using the silicon near the array, so it had undergone the solution process the same as the array itself, so it had cysteine adsorbed without having a structured surface. The settings of the FTIR were the same, and we took the measurement of the background for 10 minutes, or 161 spectra collected, after purging for 10 minutes. After the background was taken, we took then the structured array spectrum. To this end, we purged the chamber for 30 minutes with dry air after placing the substrate in the correct position under the beam and then took spectra for 30 minutes, or 483 spectra collected.

As in the experimental procedure when taking air measurements, a crucial aspect was that of the alignment. We made sure that the sample was aligned correctly by using the red lines drawn on the mount that can be seen in Figure 4 and laying down the sample in the exact position for the light beam to cover it. The importance of the beam size has already been explained before in this chapter, as it was circular and the array was a square.

In these experiments, we use propanethiol as a control. To prepare the monolayer of this molecule adsorbed onto the surface, the procedure was the same, leaving it overnight in the solution which we had prepared. To prepare this solution, we dissolved 0.036 grams into 30 mL of distilled water to have a 1mM solution. This was of the same concentration, then, as the cysteine solutions. We selected this molecule as a control because of its simplicity in the structure and because it has a thiol group, which is necessary for the adsorption to take place onto the gold surface.

3.7 SIMULATIONS WITH COMSOL

To confirm the experimental results, we computationally simulated the experiments to see if we got results that would correlate with the experimental ones.

We used the software COMSOL. It is not an easy program to use to program a specific experiment, and there are a lot of variables that we have to take into accounts, such as the dielectric medium and its properties, the geometry of the whole structure or the materials used in the different layers. These simulations were, of course, electromagnetically in their origin and purpose. We wanted to simulate the arising electromagnetic fields from the structure to see if they were coherent with the experimental results.

Thus, these simulations proved a valuable tool to test the data we were processing from the laboratory.

COMSOL Multiphysics is a piece of software that allows several types of simulations, such as aerodynamical ones, acoustics, heat transfer or chemical engineering. So, it has a wide range of uses, and so it is applied in very different fields.

In our case, we will be mainly interested in simulating electromagnetic fields. These include the electromagnetic field maps, optical chirality maps and magnitude maps, which all relate to the near evanescent fields appearing on the structure when light is incident.

The first step to prepare the simulation is to know which elements and materials we will be using and where they are with respect. For instance, in our cases (with or without amino acid), the elements were, in descending order, of material layers: air (amino acid), gold and silicon. The amino acid cysteine was added in the simulations where it was needed, so when the goal was to simulate the structures with the dielectric material. Then, the only change from working with or without amino acid is in the material section of the programming, where we specify if we have or not a dielectric material.

Once we had established the materials and the order in which we put them, we had to define their properties, such as the dielectric constant of the materials used.

While doing this, the program demands defining the geometry and the mesh. The mesh is the geometrical pattern that we divide the whole geometry in for the program to calculate everything needed and program afterwards easily.

Once the simulation is programmed, the next thing to do is to program the calculations we need to run in COMSOL. This means precisely telling what kind of results we need so the program knows what to do.

All of these will be applied in the next chapter, results.

3.8 BIBLIOGRAPHY

Skoog, D. A., Holler, F., Nieman, T., (1992). Principios de análisis instrumental, McGrawHill, 410–432

Barth, A. (2007). Infrared spectroscopy of proteins. *Biochimica et Biophysica Acta - Bioenergetics*, *1767*(9), 1073–1101. https://doi.org/10.1016/j.bbabio.2007.06.004

Basu, S., Lee, B. J., & Zhang, Z. M. (2009). Infrared Radiative Properties of Heavily Doped Silicon at Room Temperature. *Journal of Heat Transfer*, *132*(2), 023301. https://doi.org/10.1115/1.4000171

Garidel, P., & Schott, H. (2006). Fourier-Transform Mid-infrared Spectroscopy for Analysis and Screening of Liquid Protein Formulations Part 2: Details Analysis and Applications. *BioProcess International*, *1*, 48–55.

Haes, a. J., Hall, W. P., Chang, L., Klein, W. L., & Van Duyne, R. P. (2004). A Localised Surface Plasmon Resonance Biosensor: First Steps toward an Assay for Alzheimer's Disease. *Nano Letters*, *4*(6), 1029–1034. https://doi.org/10.1021/nl049670j

Kong, J., & Yu, S. (2007). Fourier Transform Infrared Spectroscopic Analysis of Protein Secondary Structures Protein FTIR Data Analysis and Band Assignment. *Acta Biochimica et Biophysica Sinica*, *39*(8), 549–559. https://doi.org/10.1186/1479-5876-10-117

Tame, M. S., McEnery, K. R., Özdemir, Ş. K., Lee, J., Maier, S. A., & Kim, M. S. (2013). Quantum plasmonics. *Nature Physics*, *9*(6), 329–340. https://doi.org/10.1038/nphys2615

Tullius, R. (2017). RYAN THESIS: High-Throughput Biosensing using Chiral Plasmonic Nanostructures. *PhD Thesis*. Retrieved from http://theses.gla.ac.uk/8657/1/2017tulliusphd.pdf

Tullius, R., Karimullah, A. S., Rodier, M., Fitzpatrick, B., Gadegaard, N., Barron, L. D., … Kadodwala, M. (2015). “superchiral” Spectroscopy: Detection of Protein Higher Order Hierarchical Structure with Chiral Plasmonic Nanostructures. *Journal of the American Chemical Society*, *137*(26), 8380–8383. https://doi.org/10.1021/jacs.5b04806

Zhong, Y., Malagari, S. D., Hamilton, T., & Wasserman, D. (2015). Review of mid-infrared plasmonic materials. *Journal of Nanophotonics*, *9*(1), 093791. https://doi.org/10.1117/1.jnp.9.093791

CHAPTER 4: ULTRASENSITIVE ENANTIOMERIC DETECTION OF BIOMOLECULAR VIBRATIONS WITH CHIRAL INFRARED NANOPHOTONICS

This chapter is based on a paper written last year and currently being reworked.

4.1 SUMMARY

Chirally sensitive vibrational circular dichroism (VCD) spectra derived from the dichroic absorption of circularly polarized infrared light are highly incisive probes of the structure and dynamic properties of biomolecules. Despite its obvious advantages, the widespread application of VCD is inhibited by its significant limitations. Specifically, it requires large amounts of material, 10-100 mg, and routinely necessitates the use of heavy water (D_2O) as a solvent. Here we show that chiral plasmonic nanostructures with resonances in the IR can be used to enantioselectively detect vibrations, at monolayer levels (~ 1 picogram), of adsorbed amino acids D-, L-and racemic cysteine. The phenomenon is based on asymmetric changes in the optical properties of the chiral nanostructures induced by the interaction of superchiral near fields with biomolecular vibrations. Since the effect relies on monitoring the extremely intense optical response of the nanostructure, rather than the weak molecular response directly, solvent constraints could be lifted and data acquisition times shortened by a factor of 100. Our work presages the use of chiral nanophotonic platforms for the development of VCD spectrometers on a chip for ultrasensitive analytical and biosensing applications including determination of absolute configuration. This chapter has been based on a paper we presented to JACS and was not accepted.

4.2 INTRODUCTION

Readily accessible vibrational spectra of molecules, which typically span the 600 – 4000 cm^{-1} region, provide distinct fingerprints of chemical structure, as has been explained throughout this thesis. They are more information rich and provide greater structural detail than techniques reliant on electronic excitations such as UV/visible absorption and fluorescence. For chiral molecules, structural incisiveness can be amplified by utilizing the chirally sensitive, vibrational optically active (VOA) techniques of Raman optical activity (ROA) (Barron, 2015) and vibrational circular dichroism (VCD) (Batista, Blanch and Bolzani, 2015). These techniques have found many applications in the study of static and dynamic structural properties of biomaterials. Despite these advantages VOA techniques have different shortcomings. Specifically, concerning sensitivity and, in the case of VCD, sampling in aqueous environments in which an intense background of IR absorption by water overlaps the signal from biomolecules. Nanophotonic approaches—in which intense electromagnetic (EM) nearfields with subwavelength localization generated around plasmonic structures are used to enhance responses—are utilized in both surface enhanced Raman Scattering (SERS) (Zong et al., 2018; Langer et al., 2020) and surface enhanced IR absorption (SEIRA)

(Neubrech et al., 2017; Adato and Altug, 2013). As well as noble metals, graphene plasmons have been used to enhance response in the mid IR region (Rodrigo et al., 2015). More recently, effective vibrational spectra have been obtained from molecules adsorbed on to arrays of dielectric nanostructures that have sharp resonances spanning a required spectral range (Tittl et al., 2018). In this case spectra are derived from changes in reflectance caused by the coupling between optical modes and molecular vibrations.

To date nanophotonics had only limited impact in VOA techniques, with only a few studies illustrating the potential of surface enhanced Raman optical activity (SEROA) (Pour, Bell and Blanch, 2011) and surface enhanced resonance Raman (SERROA) demonstrating mirror image spectra for enantiomers (Pour et al., 2015). In this chapter we present a novel optically active nanophotonic phenomenon in which biomolecules are detected by the changes they induce in the reflectance behaviour of chiral plasmonic nanostructures. The effect is derived from an asymmetry in the coupling between inherently chiral optically dark and bright modes *via* chiral near fields, mediated by vibrational modes of biomolecules. Using this effect, chiral discrimination is achieved at the single monolayer level (an effective sensitivity ~0.1 pg mm^{-2}) of adsorbed L/D-cysteine. This compares with the 10 – 100 mg of L/D-cysteine required to obtain VCD and ROA spectra in the solution phase (Kaminski, Kudelski and Pecul, 2012). Although, this proof-of-concept study uses molecular vibrations in the mid-IR spectral region, it is a generic effect that is extendable to wavelength regions such as THz and μ-wave.

The fundamental concept of the proposed work relies on a chiral plasmonic structure possessing spectrally overlapping dark and bright modes that have the potential to couple. Also, of equal importance, is that the spectral envelope of the IR modes overlaps with a useful (biological) spectral region, specifically that spanning the amide I and II molecular vibrational bands in the 1400 – 1800 cm^{-1} region. These vibrational bands are highly sensitive to the secondary structure of biomolecules and are used as fingerprint regions in ROA and VCD^2 (Blanch and Barron, 2010; Kurouski, 2017). The scaling relationship between size and the positions of resonances facilitates the tailoring of structures that have modes that overlap the mid-IR region. The criteria for ensuring overlapping bright and dark modes that are coupled are less straightforward than simply manipulating dimensions. Previous work has shown that plasmonic multi-armed "cross"-like structures, which have C_{2v} and C_{6v} symmetry, and display resonances in the visible to near-IR region, have spectrally overlapping bright (dipole) and dark (quadrupole) modes (Verellen et al., 2011). In these systems the level of coupling can be manipulated using experimental geometry, with higher levels observed for off-normal incidence.

4.3 RESULTS

Shuriken properties

The gold plasmonic nanostructure we have used in this study is a chiral version of the achiral six-armed cross, which belongs to the C_6 point group and which we refer to as a shuriken. The decision of using this structure came after several experiments, with which we concluded this was the best option. This process has been explained in the experimental process chapter. The left and right-handed forms of the shuriken structure have been fabricated on to silicon substrates, with the process being explained in chapter 2 of this thesis. They have a final thickness of 110 nm, comprising 100 nm of gold and 10 nm of the sticking layer, a lateral dimension (arm to arm length) of 1.0 μm and are arranged in a square lattice with a periodicity of 1.5 μm, see figure 1. This structure was specifically designed to exhibit a resonance in the amide I and II band region.

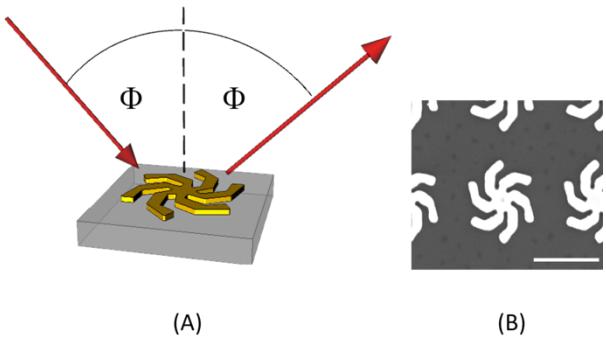

Figure 1. (**a**) A schematic illustrating the experimental geometry, where Φ is the scattering angle of the IR beam. (**b**) An electron micrograph of the shuriken structure. The scale bar indicates 1 μm.

Two experimental configurations were used to collect unpolarized IR spectra: transmission spectra were collected with the light striking the substrate at normal incidence; or reflectance spectra were collected at a range of angles (15°, 25° and 40°) with respect to the surface normal. as explained before, a peak appeared at increasing angles. The absolute positions of the peak vary between samples, associated with slight fabrication differences, with the main peak falling within the range 1575 to 1660 cm^{-1}. The angular dependence of the shuriken spectra is replicated by a comparable achiral six-armed cross (see Appendices) and is consistent with the behavior of smaller-sized gold six-armed crosses, which have resonances at significantly shorter wavelengths in the near IR (Verellen et al., 2011).

To validate the experimental spectra and to provide insight into the origin of the splitting that gives rise to the shoulder, electromagnetic (EM) numerical simulations have been performed using finite element method with the COMSOL Multiphysics Platform. In contrast to the experiments which used unpolarized light, in the simulations linearly polarized light was used, for computational simplicity. There is good agreement between modelled and experimental data, figure 2, albeit the shoulder being a more resolved dip in the simulated

spectra. This can be ascribed to the idealized model (see Appendices) used in the simulation not accounting for defects possessed by the real structures.

The chiral asymmetry of a near field of frequency ω can be parametrized by the optical chirality density (*C*) (Lipkin, 1964; Tang and Cohen, 2010)

$$C = \frac{1}{2}\left(\mathbf{D} \cdot \dot{\mathbf{B}} - \mathbf{B} \cdot \dot{\mathbf{D}}\right) \qquad \text{(eq. 25)}$$

where **D** is the displacement field, **B** the magnetic induction and $\dot{\mathbf{D}}$ and $\dot{\mathbf{B}}$ are their respective time-derivatives. Maps showing the distributions of electric fields with directions normal to the substrate (E_z) and *C* for 1449 (main peak) and 1632 cm^{-1} (shoulder), as a function of angle of incidence are shown in figure 3. At normal incidence, the signs of the electric fields at both frequencies display distributions that are odd with respect to inversion, consistent with the excitation of a dipole (optically bright) mode. As the angle of incidence increases, the signs of the fields at 1449 cm^{-1} retain dipolar character. In contrast, the fields at 1632 cm^{-1} evolve, displaying a symmetry that is even under inversion, being characteristic of a higher order optically dark mode. The appearance of the dip and the evolution of the symmetry properties of the near fields are consistent with a coupling between bright and dark modes for off-normal incidence.

The near fields created by the optical excitation of the LH and RH shurikens with linearly polarized light display regions of both positive and negative *C* (i.e. opposite chiral asymmetries), albeit with one handedness dominating. The near fields have $|C| \geq 1$ indicating they have chiral asymmetries greater than that of circularly polarized light. The $|C|$ of the near fields varies with the angle of incidence, with its magnitude increasing (decreasing) for the shoulder (main) peak, figure 3. This dependence of the magnitude of *C* on the coupling of bright and higher order dark modes has been observed previously (Karimullah et al., 2015; Abdulrahman, 2012).

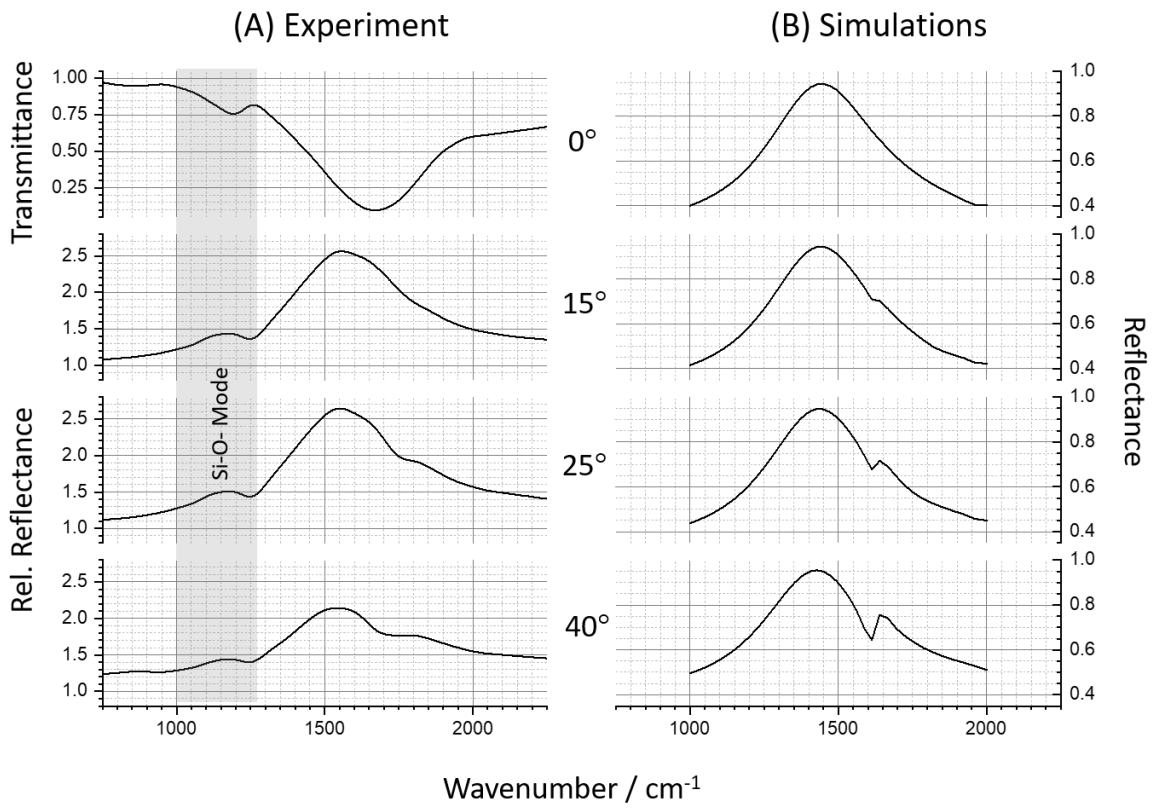

Figure 2. (**a**) IR spectra collected from LH structures as a function of angle of incidence (relative to the surface normal), Band associated with Si-O of the surface oxide layer of the silicon wafer is highlighted. (**b**) Simulated reflection spectra as a function of incidence angle.

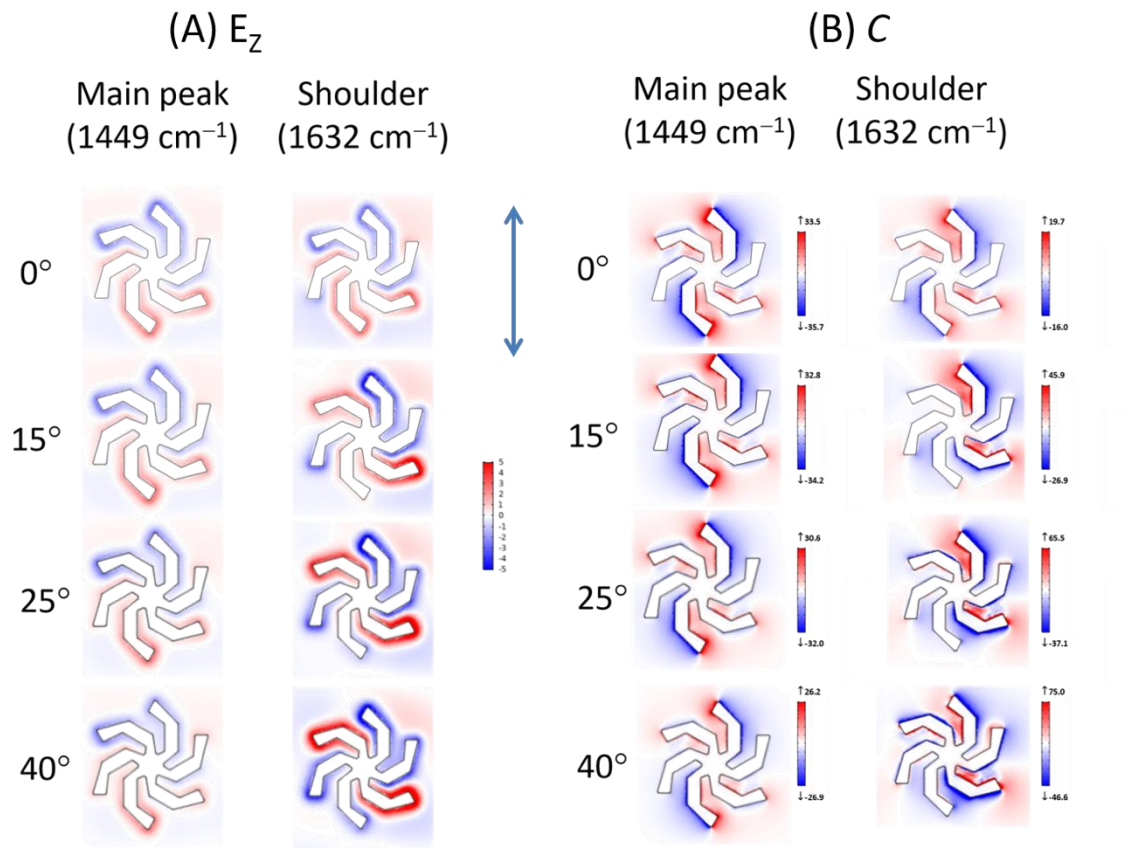

Figure 3. (**a**) The electric field (E_Z) and (**b**) C maps as a function of incident angle for the main and shoulder peaks, which are normalized to left circularly polarized. The scale bars show the maximum and values of C.

Chiral Sensitivity: Numerical Modelling

Numerical simulations have been performed with the software COMSOL to assess the sensitivity of the optical properties of the shuriken structures to the presence of chiral dielectrics, and to further confirm the initial experimental results. Reflectance spectra were modelled for light at normal and 20° incidence. Briefly, the interaction of EM fields with chiral dielectrics (such has biomaterials) can be understood through the following constitutive equations (Abdulrahman, 2012):

$$\mathbf{D} = \varepsilon_0\varepsilon_r\mathbf{E} + i\xi\mathbf{B} \quad \text{(eq. 12 in chapter 1)}$$

$$\mathbf{H} = \mathbf{B}/\mu_0\mu_r + i\xi\mathbf{E} \quad \text{(eq. 13 in chapter 1)}$$

Here, (ε_r) $\varepsilon_o$is the (relative) permittivity of free space and (μ_r) $\mu_0$is the (relative) permeability of free space. $\boldsymbol{E}$ and $\boldsymbol{H}$ are the complex electric and magnetic fields. $\xi(\lambda)$ is a wavelength dependent second rank complex tensor describing chiral molecular properties, sometimes referred to as the Pasteur coefficient, the sign of which is dependent on the handedness, and is zero for achiral media. The dispersive behavior of $|\xi(\lambda)|$ can be approximated to a Debye function (see Appendices), reaching a maximum value on resonance and falls rapidly to ~ 0 off resonance (Abdulrahman, 2012). In previous modelling studies $|\xi(\lambda)| \sim 0.1$ have been used to mimic resonant IR layers (Mohammadi Et al., 2018; Lida, 2020). Unfortunately, it is not possible to robustly model a 1 nm thick dielectric layer with a $|\xi(\lambda)| \sim 0.1$ due to computational constraint, specifically the limited number of elements that can be contained in such a thin layer. Consequently, we have used a 200 nm thick chiral layer with $|\xi(\lambda)| \sim 5 \times 10^{-4}$ to replicate the chiroptical response of Cys- lay layers, which are discussed below. This should be a realistic mimic of the 1 nm layer because it has the same height × $|\xi(\lambda)|$ value of ~ 0.1, hence the same net chiroptical response. For the off-resonance cases, it can be assumed that $|\xi(\lambda)| \approx 0$ and there is no asymmetry induced. Simulated spectra for LH and RH handed nanostructures embedded in a chiral dielectric for incident angles of 20° are shown in figure 4. The simulation show that the presence of a resonant chiral layer causes asymmetric changes in the lineshape of the plasmonic resonance, rather than a differential shift in its position. Specifically, there is an asymmetric shift in the lower wavenumber edge of the peak which is not observed on the higher wavenumber side. In addition, there are changes in the position of the dip / shoulder. This behavior is consistent with chiral vibrations causing an asymmetric change in the coupling between the dark and bright modes (Kelly et al., 2018; Tullius et al., 2017). For simplicity we have used the shifts in the peak maxima to parameterize the asymmetry. With

$$\Delta\lambda_{RH} - \Delta\lambda_{LH} = \Delta\Delta\lambda \quad \text{(eq. 26)}$$

where $\Delta\lambda_{RH/LH}$ are the shifts RH /LH structures individually induced by the presence of the layer. The asymmetry parameter, $\Delta\Delta\lambda$, for the simulations are given in figure 4. It will be subsequently used to parametrize experimental data, since it can be measured more accurately than changes in the dip region.

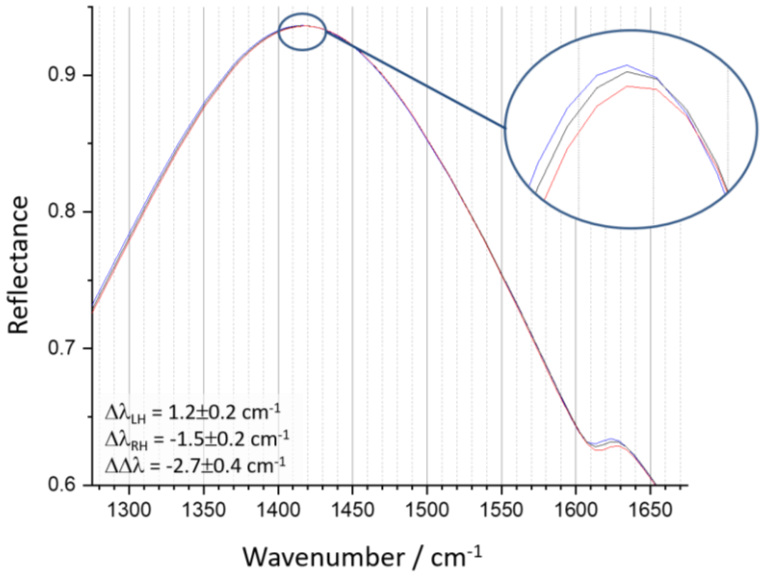

Figure 4. Simulated spectra for 20° angle of incidence. Black spectra are for an achiral dielectric on LH / RH structures, while red and blue spectra are for LH and RH structures with a chiral dielectric ($\xi = 5\times10^{-4}$) respectively. The inset shows a magnified region of the top of the peak to show the effective shift in the peak maximum. The effective asymmetry, relative to the achiral position, in the peak maxima are given in the figure.

Chiral Sensitivity Experiment

To validate the enantio-sensitivity predicted by the numerical modelling, we have studied a simple model biomolecular interface. Specifically, we have created self-assembled monolayers (SAM) of the amino acids L-, D- and racemic (Rac) cysteine [Cys = $HSCH_2CH(NH_2)CO_2H$]. It is a well-studied system that provides a facile means of creating chiral interfaces (Kuhnle, 2006). The thiol grouping of Cys deprotonates upon adsorption to form a strong S–Au bond leading to the for mation of structurally ordered air stable SAMs. The system is an ideal choice because the Cys moieties adsorbed on noble metal surfaces have vibrational bands (Marti, Methivier and Pradier, 2004) (see Appendices for band assignment) that overlap with the amide I and II bands of more complex peptides and proteins. Also previous VCD studies of non-plasmonic gold nanoparticles functionalized with thiol moieties of cysteine derivatives (Gautier and Burgi, 2006), show that the bands that overlap the plasmonic resonance exhibit strong dichroic behavior. Thus, they provide a simple well-defined air-stable system that establishes the efficacy of the postulated effect to more complex and important biomaterials. In addition to the Cys residues, we have also created SAMs using propyl thiol (PT) to act as an achiral reference. All the details of the experimental process can be found in the dedicated chapter of this work, both for the experiments in air and with the Cys adsorbed.

In figure 5 are the reflectance IR spectra collected at 15° from the surface normal, from LH and RH shurikens; (with and without Cys / PT) and the $\Delta\lambda_{RH/LH}$ and $\Delta\Delta\lambda$ values derived from

them. There is a clear asymmetry in the effects of individual enantiomeric monolayers on the optical properties of LH and RH shurikens. The $\Delta\lambda_{LH/RH}$ values have opposite signs that reverse sense when switching enantiomer, which is consistent with a chiroptical response. Consequently, as expected the L and D- enantiomer give $\Delta\Delta\lambda$ values of opposite sign but similar magnitude. As expected, monolayers of Rac-Cys and PT give no significant asymmetry.

To correlate the observed asymmetries in the resonance of the nanostructures to the chiral vibrational modes of Cys, we have also performed experiments on two other substrates with shurikens of different dimensions but retaining the square lattice. Specifically, with arm to arm separations of 0.75 and 2 μm and pitches of 1.13 and 3.00 μm, subsequently these are referred to as 0.75 and 2 μm structures. The 0.75 and 2 μm structures have resonances centered at ~ 850 and 2450 cm^{-1}, which do not overlap with vibrational bands of the Cys moiety (see Appendices for conventional IR and VCD covering these regions)[II]. The angular dependences of the resonances of these two structures are in qualitative agreement with that observed for the 1-μm structure. In both cases, a shoulder is observed for off normal incidence, which becomes more pronounced with increasing angle, consistent with coupling between bright and dark modes. This agrees with the observation made in previous studies of achiral 6-armed crosses, where such coupling was observed over a range of dimensions (Verellen et al., 2011). The introduction of L- and D-Cys monolayers induce no significant asymmetries for these structures, figure 5.

There are effects that are not accounted for in the numerical modelling, which would be expected to amplify the observed optical asymmetries. Specifically, the potential of surface enhancement to increase the cross-section for exciting certain vibrational modes of a molecule in the proximity of a metal surface (Moskovits, 1982). This effect is the basis of the surface selection rules that are routinely applied to vibrational spectra of molecular adsorbates on planar metal surfaces obtained from reflection absorption IR spectroscopy (RAIRS) and electron energy loss spectroscopy (EELS) (Moskovits, 1985). The surface selection rule is commonly rationalized in terms of image charges. Within this framework the vibrating system is considered a composite of the adsorbed molecule and its conjugate-charge image in the metal. It can be shown that molecular vibrations with transition dipoles directed parallel to the metal surface would have zero composite transition dipoles. In contrast vibrations whose transition dipoles have a component normal to metal surface would have that component reinforced in the composite system. This amplification of the transition dipole by coupling to the image charge enhances the IR response of molecular vibration by up to an order of magnitude. A previous RAIRS study of the adsorbed monolayers of the cysteine moiety shows that it has surface vibrations at 1510 and 1652 $cm^{-1.}$ that have relative reflectances of 0.05 – 0.1%. This mechanism should be differentiated from the use of near fields associated with nanoparticles for the enhancement of vibrational spectroscopic response. In the case of chiral molecules, image charge coupling amplifies the chiral transition dipole resulting in enhanced values of ξ.

4.4 DISCUSSION

The phenomenon we present for the detection of chiral vibrational modes is based on a fundamentally different philosophy to previously considered strategies for achieving enhanced VOA measurements. Recent work has focused on directly measuring vibrational spectra using chiral near fields (Lida, 2020). This strategy suffers from fundamental weaknesses which affects reliability and its potential usefulness. It is insensitive, requiring large amounts of material 100-1000 nm thick films (equivalent to ~100 -1000 layers of a compound such as cysteine). Also, it does not overcome the principal weakness of VCD, that the signals are still small compared to the water absorption, making its use in aqueous environments problematic at best. It is also highly susceptible to artefacts due to possible incorrect subtraction of the significant underlying nanostructure background signal. The backgrounds are ≥ one order of magnitude larger than the individual IR molecular response, and ≥ three orders larger than the differences. In contrast, the phenomenon reported here relies on a far simpler and more sensitive measurement, monitoring with unpolarized light, relative shifts in the large optical response of chiral nanostructure induced by chiral vibrations of single monolayers.

Another considerable advantage of using chiral nanophotonic platforms to obtain VOA spectra is the rapidity of the measurements. Even with state-of-the-art instrumentation a VCD spectrum of a chiral molecule, such as the enantiomers of cysteine shown in Appendices, take 48 hours to collect. In contrast using a nanophotonic platform containing structures with resonances spanning an appropriate range, an equivalent spectrum could be obtained in ~ 20 mins, a two order of magnitude enhancement in data acquisition time.

In conclusion, we have established the efficacy of using chiral nanophotonic platforms for enantiomeric detection of biomolecular vibrations. It is proposed that sensing is based on asymmetric changes in the coupling of bright and dark modes mediated by chiral molecular vibrations. The phenomenon reported has superior performance to conventional chirally sensitive vibrational techniques. Its sensitivity is picomole, 8-9 orders of magnitude greater than the 1-10 mmol routinely achieved with VCD and ROA, and with data acquisition times ~ 2 orders of magnitude shorter. The technique relies on an intense response from the nanostructured substrates, which can be incorporated into micro / nanofluidic cells. These environments provide short optical path length in solution (< 10 μm) and in addition, using an appropriate IR transmissive substrate, a back reflective experimental geometry can be utilized (*i.e.*, there is no requirement for light to pass through aqueous environments). Consequently, there is no need to suppress the H_2O background—which would swamp the amide I and II region—by using D_2O, simplifying and reducing the cost of analysis. The phenomenon is convergent with an array format offering the opportunity to create a "VCD" spectrometer on a chip. This would uniquely allow the pico/nanomole characterization of high value pharmacological species such as proteins, peptides and oligonucleotides. It may also provide absolute configuration of trace amounts of smaller pharmaceutically relevant molecules.

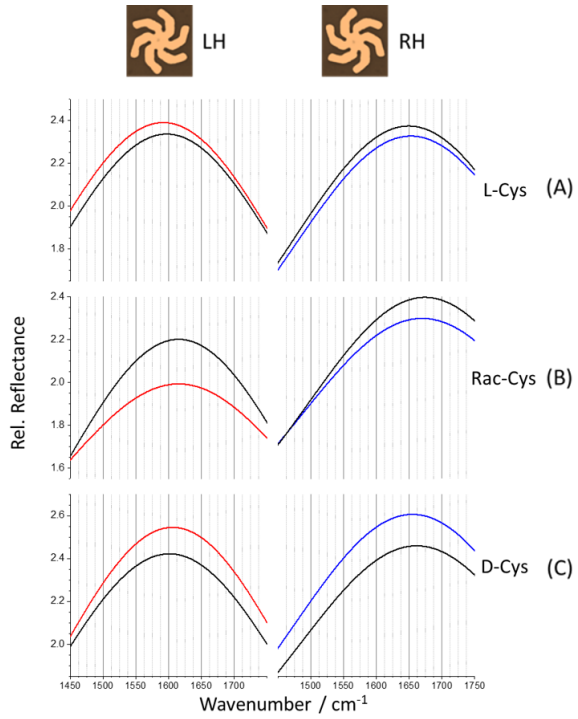

	$\Delta\lambda_{LH}$ / cm^{-1}	$\Delta\lambda_{RH}$ / cm^{-1}	$\Delta\Delta\lambda_{RH-LH}$ / cm^{-1}
2 µm (845-855 cm^{-1})			
L-Cys	-0.4±2.0	1.1±2.0	1.5±4.0
Rac-Cys	1.4±2.0	1.6±2.0	0.2±4.0
D-Cys	-3.4±2.0	-1.9±2.0	1.5±4.0
1 µm (1590–1660 cm^{-1})			
L-Cys	−6.3±2.0	3.0±2.0	9.0±4.0
Rac-Cys	-0.1±2.0	-4.1±2.0	-4±4.0
D-Cys	5.0±2.0	−6.4±2.0	−11.4±4.0
PT	-5.2±2.0	-2.7±2.0	-2.5±4.0
0.75 µm (2430-2460 cm^{-1})			
L-Cys	-10.0±2.0	-11.4±2.0	-1.4±4.0
Rac-Cys	-16.9±2.0	-14.3±2.0	2.6±4.0
D-Cys	-7.8±2.0	-8.2±2.0	-0.4±4.0

(D)

Figure 5. Experimental reflectance spectra collected at 15° with SAMs of (**a**) L-Cys, (**b**) Rac-Cys and (**c**) D-Cys. Black and blue/red spectra have been collected in the absence and presence of the adsorbed SAM respectively. (**d**) the individual shifts and asymmetries derived from the spectra in (A)-(C) are tabulated. The opposite signs of the $\Delta\lambda_{L/R}$ displayed by L- and D- Cys are highlighted in blue and red shading.

4.5 BIBLIOGRAPHY

Abdulrahman, N. A.; Fan, Z.; Tonooka, T.; Kelly, S. M.; Gadegaard, N.; Hendry, E.; Govorov, A. O.; Kadodwala, M., Induced Chirality through Electromagnetic Coupling between Chiral Molecular Layers and Plasmonic Nanostructures. *Nano Letters* **2012,** *12* (2), 977-983.

Adato, R.; Altug, H., In-situ ultra-sensitive infrared absorption spectroscopy of biomolecule interactions in real time with plasmonic nanoantennas. *Nature Communications* **2013,** *4*, 10.

Barron, L. D., The development of biomolecular Raman optical activity spectroscopy. *Biomedical Spectroscopy and Imaging* **2015,** *4* (3), 223-253.

Batista, J. M.; Blanch, E. W.; Bolzani, V. D., Recent advances in the use of vibrational chiroptical spectroscopic methods for stereochemical characterization of natural products. *Natural Product Reports* **2015,** *32* (9), 1280-1302.

Blanch, E. W.; Barron, L. D., Raman Optical Activity of Biological Molecules. In *Emerging Raman Applications and Techniques in Biomedical and Pharmaceutical Fields*, Matousek, P.; Morris, M. D., Eds. Springer: New York, 2010; pp 153-177.

Gautier, C.; Burgi, T., Chiral N-isobutyryl-cysteine protected gold nanoparticles: Preparation, size selection, and optical activity in the UV-vis and infrared. *Journal of the American Chemical Society* **2006,** *128* (34), 11079-11087.

Kaminski, M.; Kudelski, A.; Pecul, M., Vibrational Optical Activity of Cysteine in Aqueous Solution: A Comparison of Theoretical and Experimental Spectra. *Journal of Physical Chemistry B* **2012,** *116* (16), 4976-4990.

Karimullah, A. S.; Jack, C.; Tullius, R.; Rotello, V. M.; Cooke, G.; Gadegaard, N.; Barron, L. D.; Kadodwala, M., Disposable Plasmonics: Plastic Templated Plasmonic Metamaterials with Tunable Chirality. *Advanced Materials* **2015,** *27* (37), 5610-5616.

Kelly, C.; Khorashad, L. K.; Gadegaard, N.; Barron, L. D.; Govorov, A. O.; Karimullah, A. S.; Kadodwala, M., Controlling Metamaterial Transparency with Superchiral Fields. *Acs Photonics* **2018,** *5* (2), 535-543.

Kuhnle, A.; Linderoth, T. R.; Schunack, M.; Besenbacher, F., L-cysteine adsorption structures on Au(111) investigated by scanning tunneling microscopy under ultrahigh vacuum conditions. *Langmuir* **2006,** *22* (5), 2156-2160.

Kurouski, D., Advances of Vibrational Circular Dichroism (VCD) in bioanalytical chemistry. A review. *Analytica Chimica Acta* **2017,** *990*, 54-66.

Langer, J.; de Aberasturi, D. J.; Aizpurua, J.; Alvarez-Puebla, R. A.; Auguie, B.; Baumberg, J. J.; Bazan, G. C.; Bell, S. E. J.; Boisen, A.; Brolo, A. G.; Choo, J.; Cialla-May, D.; Deckert, V.; Fabris, L.; Faulds, K.; de Abajo, F. J. G.; Goodacre, R.; Graham, D.; Haes, A. J.; Haynes, C. L.; Huck, C.; Itoh, T.; Ka, M.; Kneipp, J.; Kotov, N. A.;

Kuang, H.; Le Ru, E. C.; Lee, H. K.; Li, J. F.; Ling, X. Y.; Maier, S. A.; Mayerhofer, T.; Moskovits, M.; Murakoshi, K.; Nam, J. M.; Nie, S.; Ozaki, Y.; Pastoriza-Santos, I.; Perez-Juste, J.; Popp, J.; Pucci, A.; Reich, S.; Ren, B.; Schatz, G. C.; Shegai, T.; Schlucker, S.; Tay, L. L.; Thomas, K. G.; Tian, Z. Q.; Van Duyne, R. P.; Vo-Dinh, T.; Wang, Y.; Willets, K. A.; Xu, C.; Xu, H.; Xu, Y.; Yamamoto, Y. S.; Zhao, B.; Liz-Marzan, L. M., Present and Future of Surface-Enhanced Raman Scattering. *Acs Nano* **2020,** *14* (1), 28-117.

Lida, T., Super-chiral vibrational spectroscopy with metasurfaces for high-sensitiveidentification of alanine enantiomers. Ishikawa, A., Ed. AIP: Applied Physics Letter, 2020; Vol. 117, p 101103.

Lipkin, D. M., EXISTENCE OF NEW CONSERVATION LAW IN ELECTROMAGNETIC THEORY. *Journal of Mathematical Physics* **1964,** *5* (5), 696-&.

Marti, E. M.; Methivier, C.; Pradier, C. M., (S)-Cysteine chemisorption on Cu(110), from the gas or liquid phase: An FT-RAIRS and XPS study. *Langmuir* **2004,** *20* (23), 10223-10230.

Mohammadi, E.; Tsakmakidis, K. L.; Askarpour, A. N.; Dehkhoda, P.; Tavakoli, A.; Altug, H., Nanophotonic Platforms for Enhanced Chiral Sensing. *Acs Photonics* **2018,** *5* (7), 2669-2675.

Moskovits, M., SURFACE SELECTION-RULES. *Journal of Chemical Physics* **1982,** *77* (9), 4408-4416.

Moskovits, M., SURFACE-ENHANCED SPECTROSCOPY. *Reviews of Modern Physics* **1985,** *57* (3), 783-826.

Neubrech, F.; Huck, C.; Weber, K.; Pucci, A.; Giessen, H., Surface-Enhanced Infrared Spectroscopy Using Resonant Nanoantennas. *Chemical Reviews* **2017,** *117* (7), 5110-5145.

Pour, S. O.; Bell, S. E. J.; Blanch, E. W., Use of a hydrogel polymer for reproducible surface enhanced Raman optical activity (SEROA). *Chemical Communications* **2011,** *47* (16), 4754-4756.

Pour, S. O.; Rocks, L.; Faulds, K.; Graham, D.; Parchansky, V.; Bour, P.; Blanch, E. W., Through-space transfer of chiral information mediated by a plasmonic nanomaterial. *Nature Chemistry* **2015,** *7* (7), 591-596.

Rodrigo, D.; Limaj, O.; Janner, D.; Etezadi, D.; de Abajo, F. J. G.; Pruneri, V.; Altug, H., Mid-infrared plasmonic biosensing with graphene. *Science* **2015,** *349* (6244), 165-168.

Tang, Y.; Cohen, A. E., Optical Chirality and Its Interaction with Matter. *Physical Review Letters* **2010,** *104* (16).

Tittl, A.; Leitis, A.; Liu, M. K.; Yesilkoy, F.; Choi, D. Y.; Neshev, D. N.; Kivshar, Y. S.; Altug, H., Imaging-based molecular barcoding with pixelated dielectric metasurfaces. *Science* **2018,** *360* (6393), 1105-+.

Tullius, R.; Platt, G. W.; Khosravi Khorashad, L.; Gadegaard, N.; Lapthorn, A. J.; Rotello, V. M.; Cooke, G.; Barron, L. D.; Govorov, A. O.; Karimullah, A. S.; Kadodwala, M., Superchiral Plasmonic Phase Sensitivity for Fingerprinting of Protein Interface Structure. *ACS nano* **2017**.

Verellen, N.; Van Dorpe, P.; Vercruysse, D.; Vandenbosch, G. A. E.; Moshchalkov, V. V., Dark and bright localized surface plasmons in nanocrosses. *Optics Express* **2011,** *19* (12), 11034-11051.

Zong, C.; Xu, M. X.; Xu, L. J.; Wei, T.; Ma, X.; Zheng, X. S.; Hu, R.; Ren, B., Surface-Enhanced Raman Spectroscopy for Bioanalysis: Reliability and Challenges. *Chemical Reviews* **2018,** *118* (10), 4946-4980.

APPENDICES

INFRARED SPECTROSCOPY

The template substrates were placed on the base of a specular reflection accessory (Physik Instrumente) and their reflectance spectra were measured using a Bruker Tensor 27 spectrometer equipped with a Globar lamp, a DLaTGS detector, and a KBr beamsplitter. Final spectra were produced after averaging 480 scans taken at room temperature between 400 and 4,000 cm^{-1} with 1 cm^{-1} resolution. Background spectra were acquired measuring a sample of untreated silicon substrate. The sample compartment of the spectrometer was purged with dry air for 30 minutes before each measurement to remove any possible atmospheric intrusion in the spectra.

VCD SPECTROSCOPY

L- and D-cysteine were dissolved in D_2O up to a concentration of 40 mg/mL (0.33 M). 150 µL solution was loaded into a demountable cell equipped with BaF_2 windows. A 25 µm spacer was placed in between the windows. Spectra were recorded in the region 1800-800cm^{-1} in blocks (~ 8 h measuring time per block) of 25,000 scans at a resolution of 4 cm^{-1}. Each measurement consisted in 4 blocks, which were averaged together and then subtracted by the spectrum of D_2O (Fig. S1). No other baseline correction was applied.
In order to better visualize the VCD bands populating the region 1800-1300 cm^{-1}, 10 mg/mL samples (0.083 M) were measured using CaF_2 windows separated by 100 µm spacer. Spectra of L/D-cysteine were recorded for a total of 40,000 scans (Fig. S2).

For measurements above 1800 cm^{-1}, the low pass filter was exchanged, the instrument recalibrated and 40 mg/mL (0.33 M) samples of L/D-cysteine in MilliQ H_2O (as D_2O absorbs in this region) in the 25 µm BaF_2 cell were measured for 20,000 scans (Fig. S3).

All spectra were measured on a Bruker INVENIO FT-IR spectrometer equipped with a PMA 50 VCD compartment and a nitrogen cooled MCT detector.

L/D-cysteine and D_2O were purchased from Merck. H_2O was purified in-house.

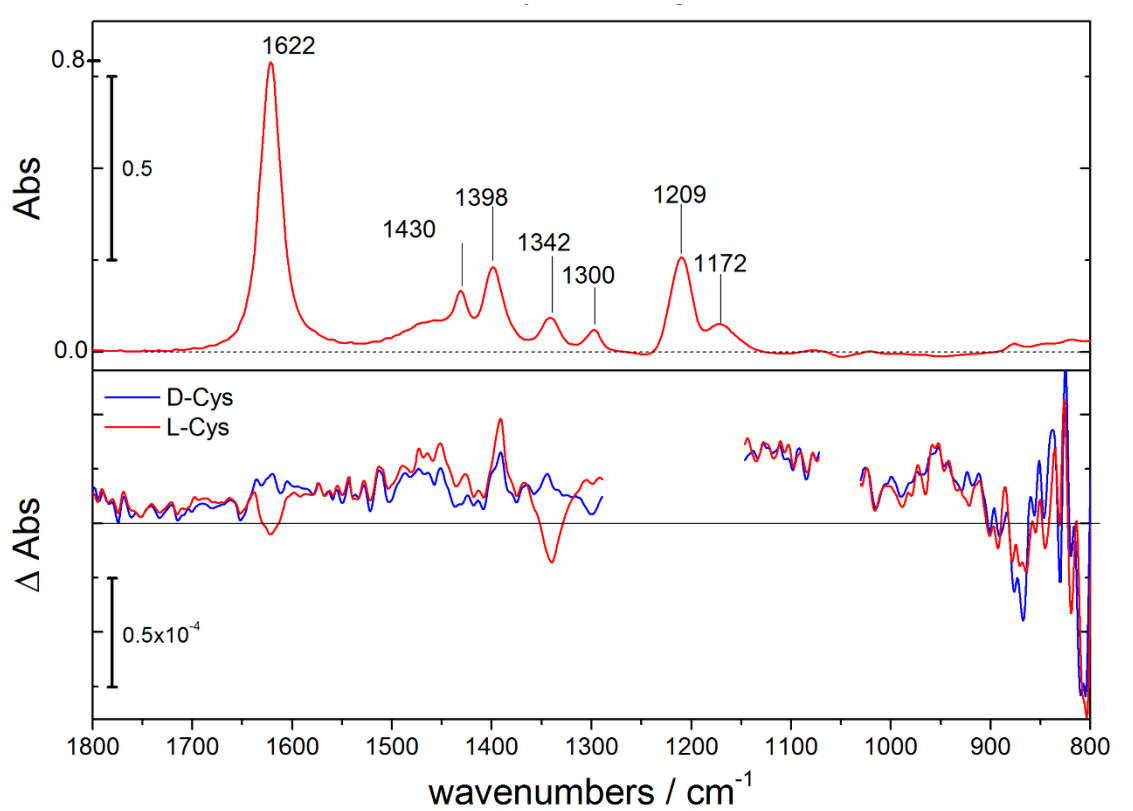

Figure S1. IR (top) and VCD (bottom) spectra of L- (red) and D-cysteine (blue) in D_2O using BaF_2 windows. The two regions removed from the spectra were extracted due to excessive background noise. The increase in baseline noise below 900 cm^{-1} was due to onset of transmission loss in the BaF_2 windows.

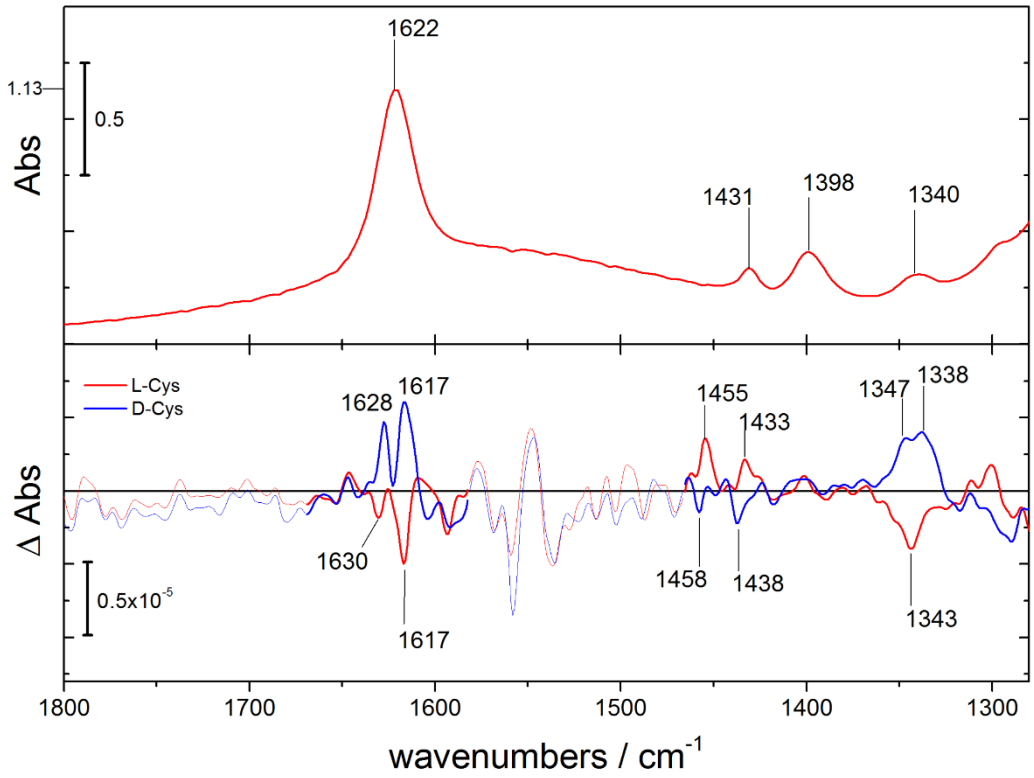

Figure S2. IR (top) and VCD (bottom) spectra of L- (red) and D-cysteine (blue) in D_2O using CaF_2 windows. The shaded regions are essentially free from signals, indicating the VCD baseline level.

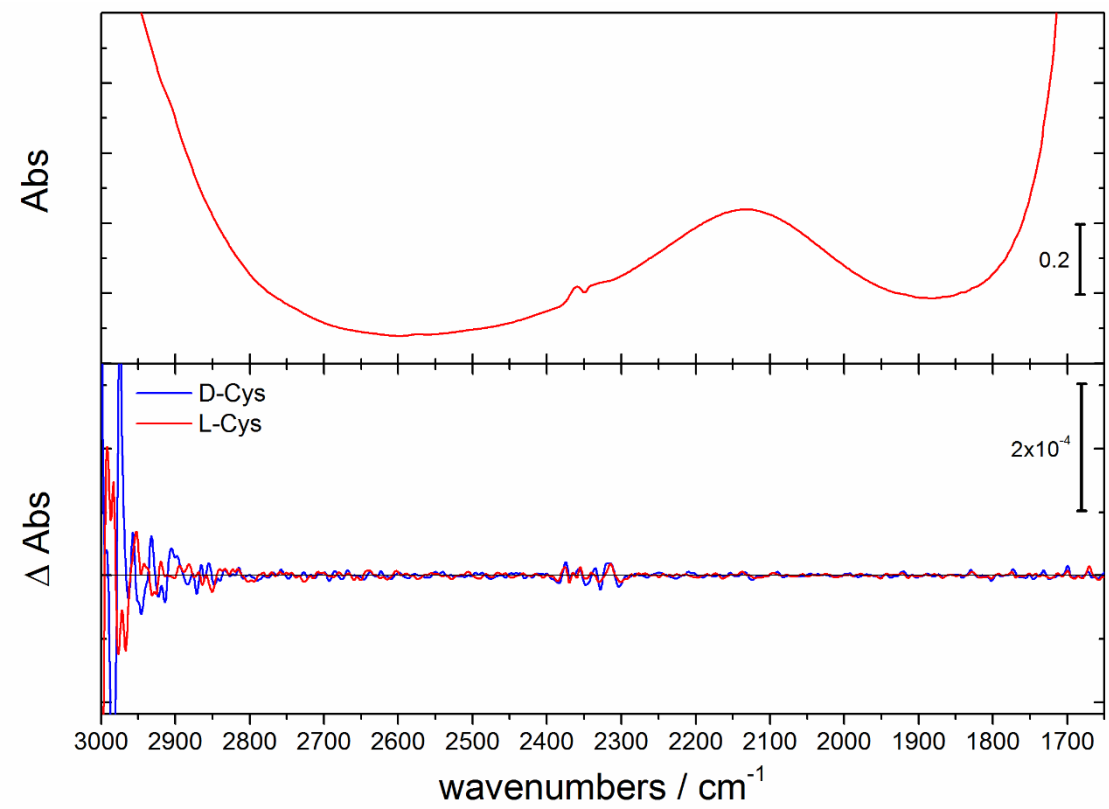

Figure S3. IR (top) and VCD (bottom) spectra of L- (red) and D-cysteine (blue) in H_2O using BaF_2 windows. The slight feature in the IR and corresponding VCD noise increase between 2300 and 2400 ccm^{-1} was due to CO_2.

SIMULATIONS

Electromagnetic (EM) simulations were performed using a commercial finite-element package (COMSOL v4.4, Wave optics module). Periodic boundary conditions were used to emulate the meta-film arrays. Perfectly matched layer conditions were used above and below the input and output ports. Linearly polarized EM waves were applied at normal incidence onto the films. COMSOL uses the finite element method to solve Maxwell's equations over a specified geometry with fields and optical chirality being measured at pre-defined surfaces above, within, and below the films.

FABRICATION

The shurikens were designed using CAD software; they were arrayed to cover a total area of 5×5 mm². The structures were fabricated on silicon wafers 25×25 mm² that were cleaned for 5 min in acetone and 5 min in isopropanol both under ultrasonic agitation before being blown dry in a stream of nitrogen. A bilayer of poly(methyl methacrylate) (PMMA) was spun to a thickness of about 200 nm and baked at 180°C for 1 hour. A 10 nm NiCr layer was evaporated as a charge conduction layer during the electron beam lithography. The pattern was exposed in a Vistec VB6 UHR EWF lithography tool. After exposing the samples, the NiCr layer was removed in a chromium etch, rinsed in water and dried in a stream of nitrogen before development in isopropyl alcohol (IPA) methyl isobutyl ketone (MIBK) (2.5:1). Prior to metal deposition, the samples were exposed for 1 minute at 60W to an oxygen plasma. 10 nm of titanium was used as an adhesion layer and followed by 100 nm of gold. The final patterns were achieved in a lift-off process by leaving the samples in acetone for about 3 hours.

PASTEUR PARAMETER

The Pasteur coefficient (ξ) is given by,

$$\xi = 4\pi n_c i \frac{\mu_{12} \cdot m_{12}}{3} \left(\frac{1}{\hbar\omega - \hbar\omega_0 + i\Gamma} + \frac{1}{\hbar\omega + \hbar\omega_0 + i\Gamma} \right) \qquad \text{(eq. 1)}$$

where $\boldsymbol{\mu}_{12}$ and $\mathbf{m}_{21}$ are the electric and magnetic dipolar matrix elements for the molecular transition and n_c is the density of molecules in the film. The molecular resonance broadening, Γ, can be estimated to be $\Gamma_{12} = \hbar\omega_0 \frac{FWHM_{mol}}{2 \cdot \lambda_{mol}}$. Eq. (1) only provides an approximation for ξ since interactions between molecular dipoles are ignored. However, the general form of Eq. 1 is valid even for a dense molecular film with strongly interacting molecules.

MODEL SHURIKEN STRUCTURE

Idealized shuriken structure used in numerical simulations is shown below.

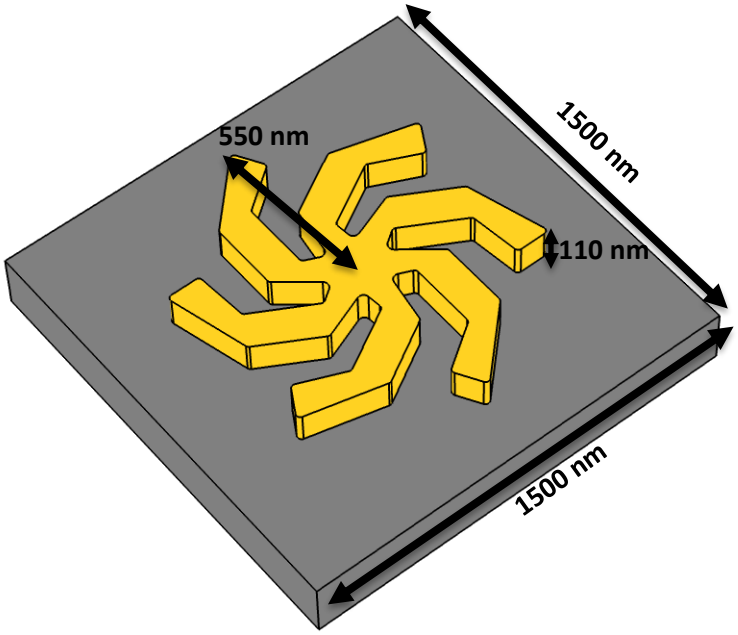

Figure S4. A Schematic of the idealized RH shuriken structure used in the numerical simulations.

Position / cm^{-1}	**Assignment**
1652	$\delta_{as}(NH_3^+)$ $\upsilon_{as}(COO^-)$
1510	$\delta_s(NH_3^+)$
1423	Sciss (CH_2)
1396	$\upsilon_s(COO^-)$
1340	Wag (CH_2
1216 1130	Rock (NH_3^+)
1061 900	υ(CN)

Table S1. Assignments of IR active vibrational bands of adsorbed (S)-cysteine moiety. Assignments taken from Mateo Marti et al., reference 24 in the main text, for adsorbed cysteine moieties on Cu(110). Bands will are shifted relative to the free molecules.

DETERMINING $\Delta\lambda_{L/R}$

The values of $\Delta\lambda_{L/R}$ have been derived from positions obtained by fitting peak maxima of the plasmonic resonances with a Gaussian function. Data obtained for 0.75, 1 and 2 μm structures are shown in figures S2, S3 and S4 respectively. The IR spectra shown are collected in air from shurikens with and without cysteine SAMs. The spectra displayed are unsmoothed and the average of 6.

SUPPLEMENTARY DATA

Shurikens

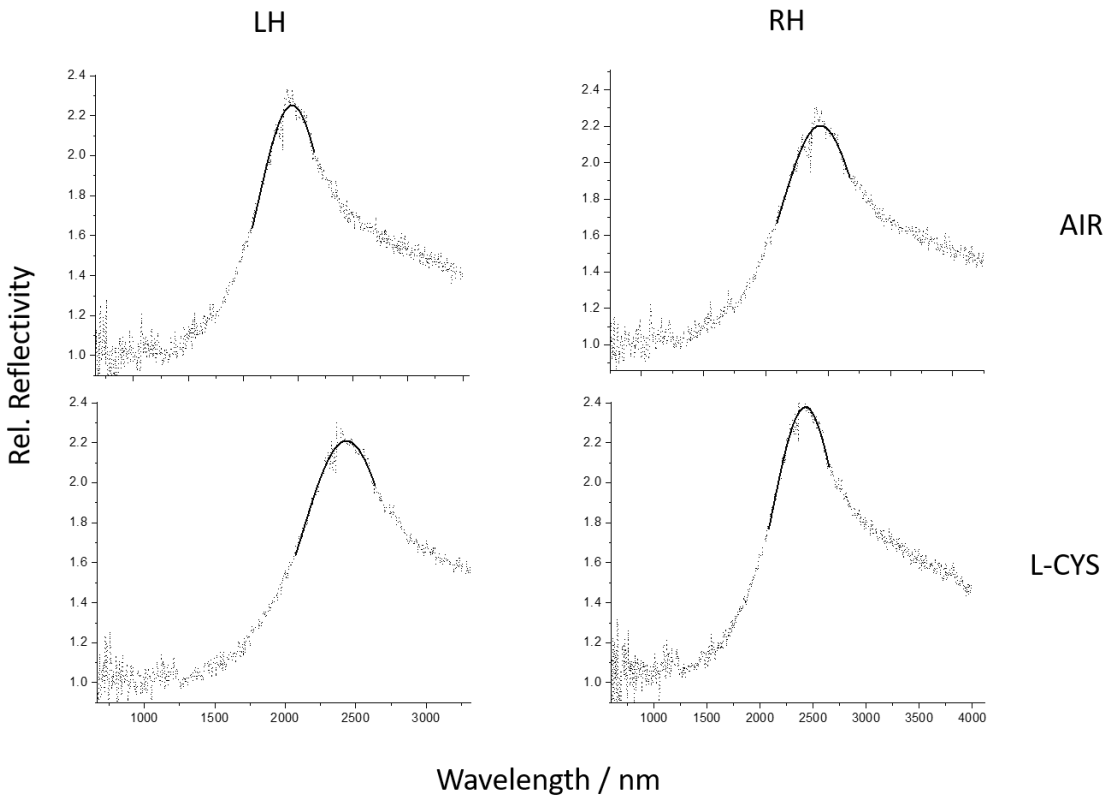

Spectra for 0.75 μm shuriken (dotted lines) and the Gaussian fits to the peak maxima are shown in solid black for L-cys.

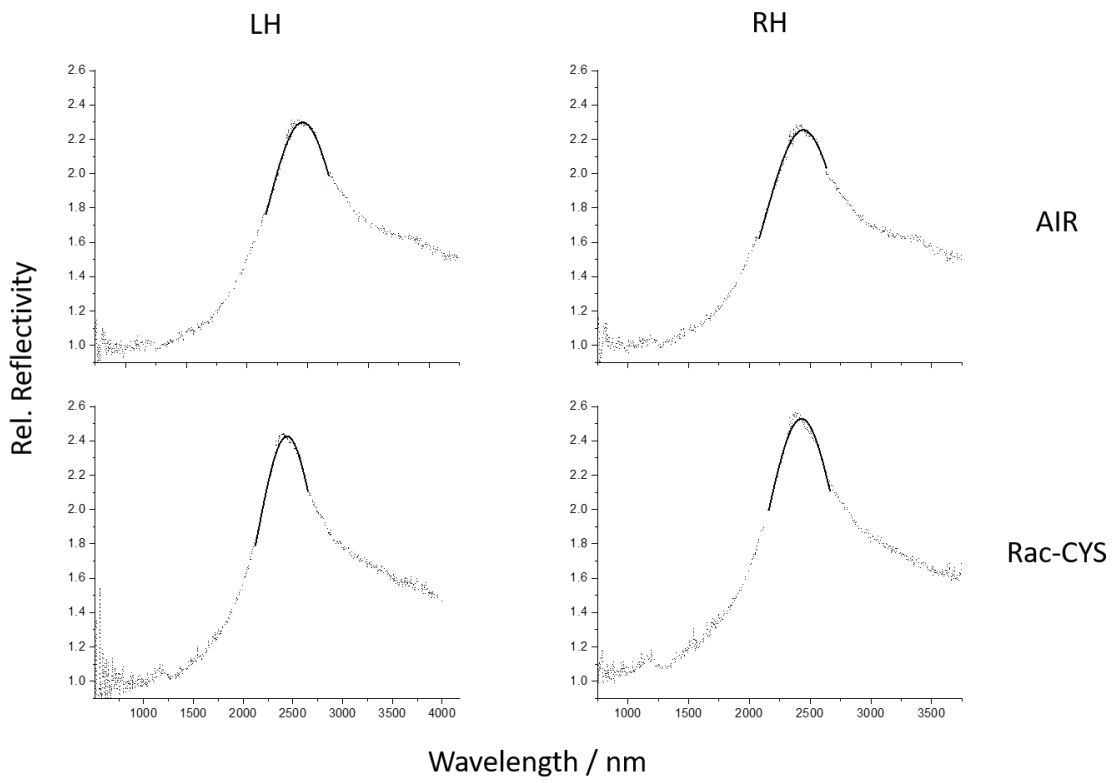

Figure S5. Spectra for 0.75 μm shuriken (dotted lines) and the Gaussian fits to the peak maxima are shown in solid black for Rac-cys

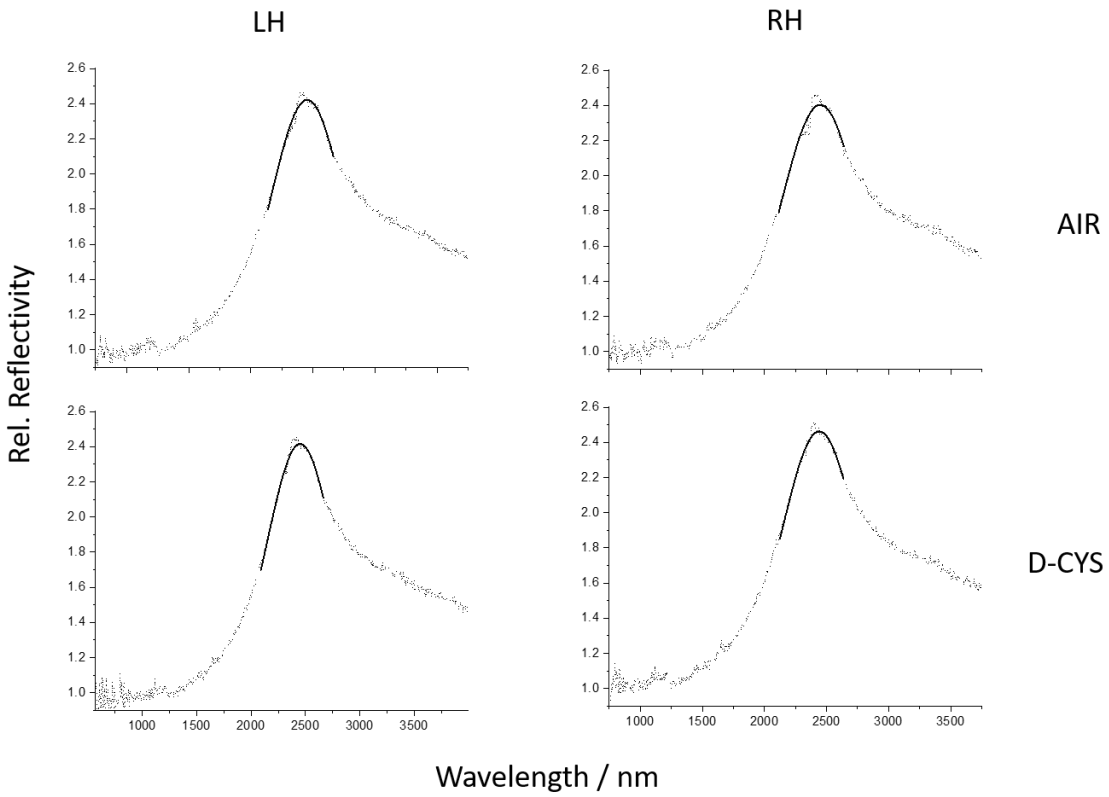

Figure S6. Spectra for 0.75 μm shuriken (dotted lines) and the Gaussian fits to the peak maxima are shown in solid black for D-cys.

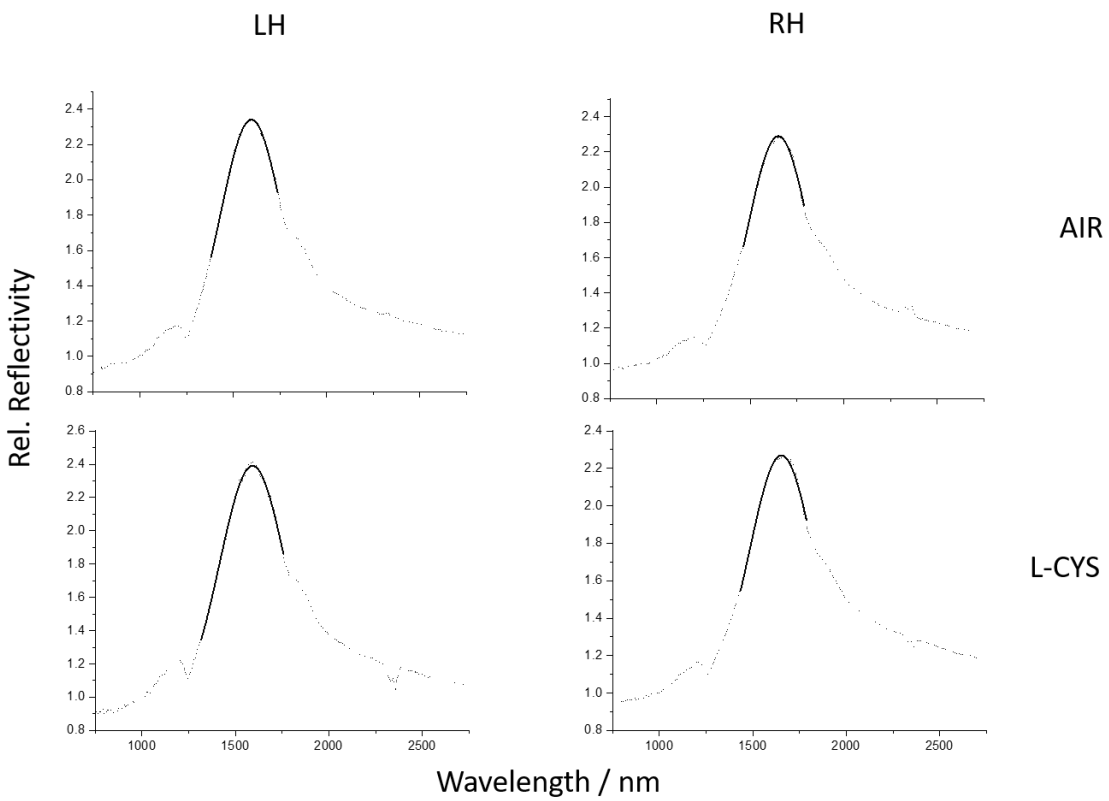

Figure S7. Spectra for 1.0 μm shuriken (dotted lines) and the Gaussian fits to the peak maxima are shown in solid black for L-cys.

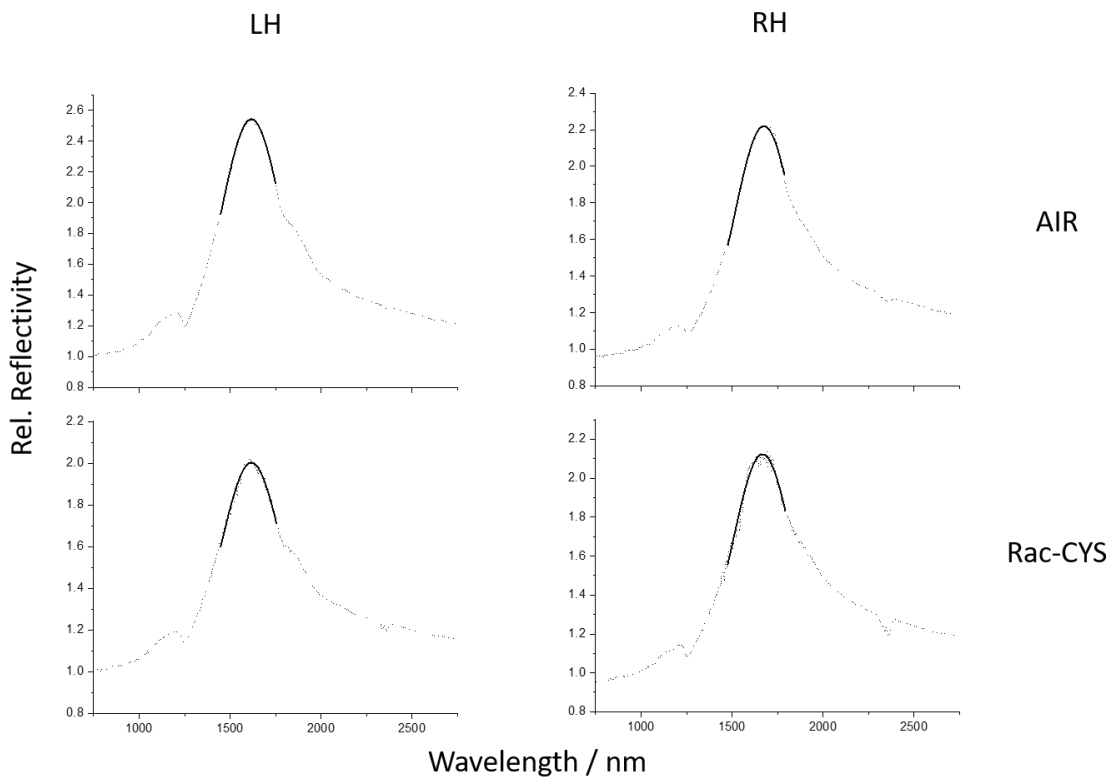

Figure S8. Spectra for 1.0 μm shuriken (dotted lines) and the Gaussian fits to the peak maxima are shown in solid black for Rac-cys.

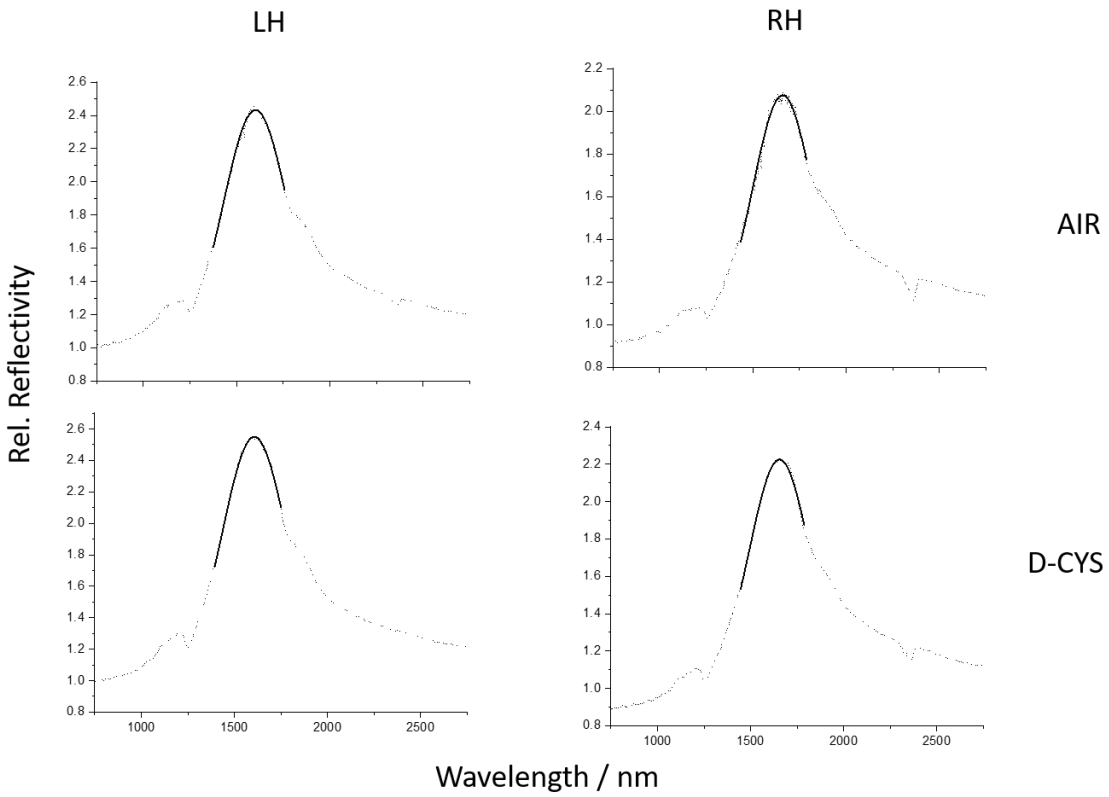

Figure S9. Spectra for 1.0 μm shuriken (dotted lines) and the Gaussian fits to the peak maxima are shown in solid black for D-cys.

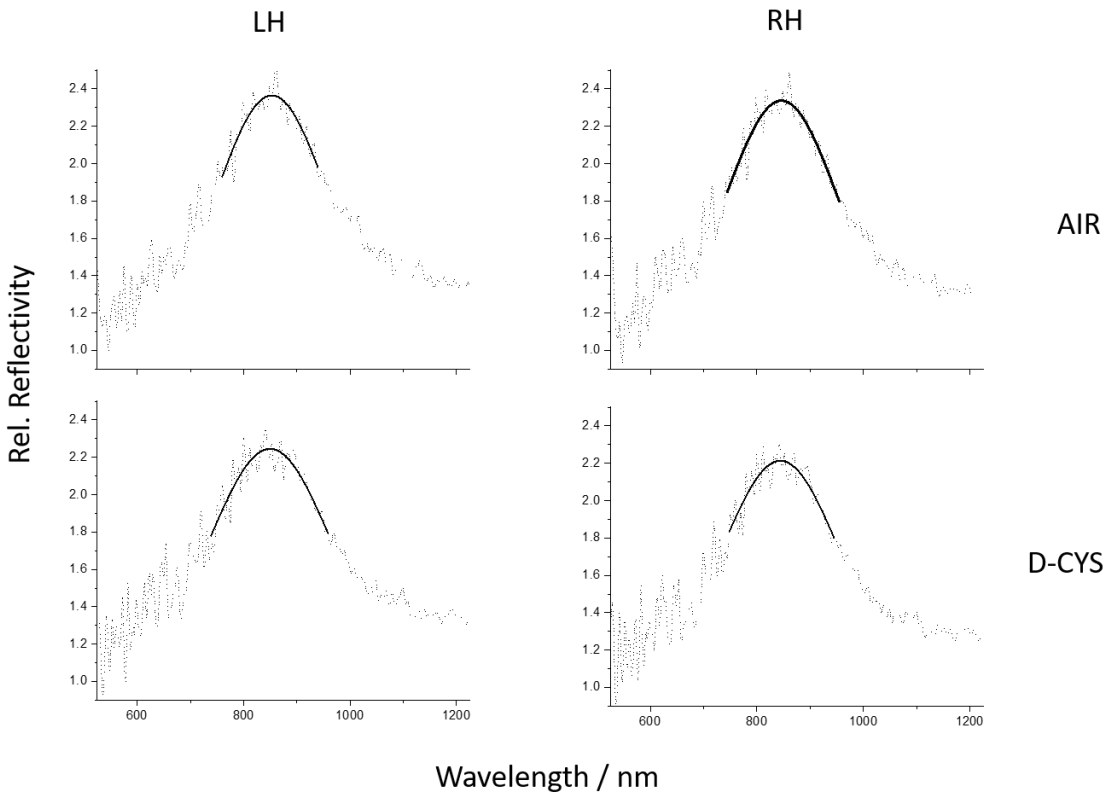

Figure S10. Spectra for 2.0 μm shuriken (dotted lines) and the Gaussian fits to the peak maxima are shown in solid black for D-cys..

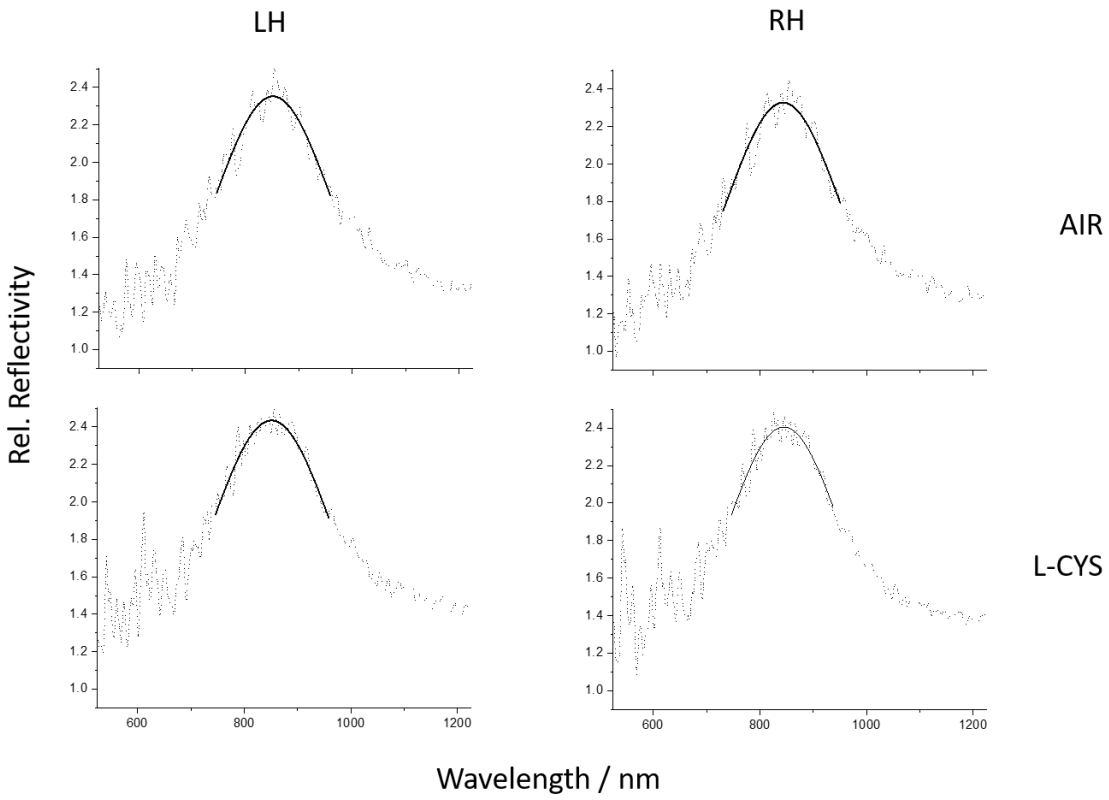

Figure S11. Spectra for 2.0 μm shuriken (dotted lines) and the Gaussian fits to the peak maxima are shown in solid black for L-cys..

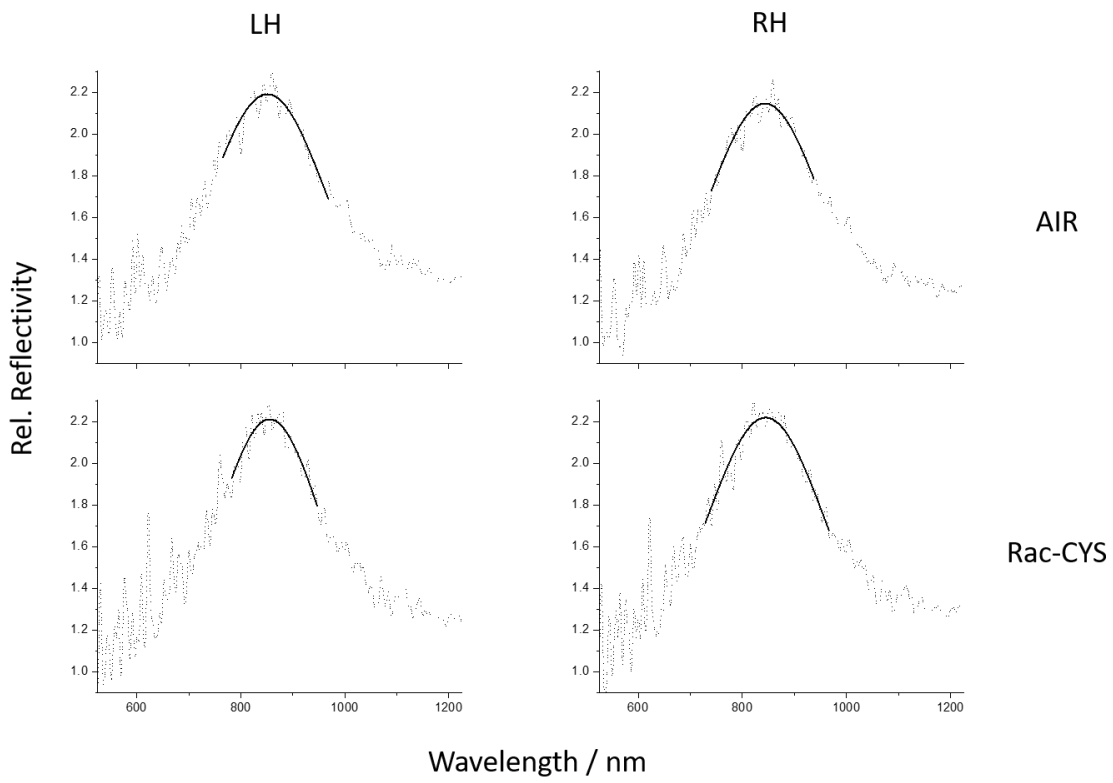

Figure S12. Spectra for 2.0 μm shuriken (dotted lines) and the Gaussian fits to the peak maxima are shown in solid black for Rac-cys.

Achiral Cross

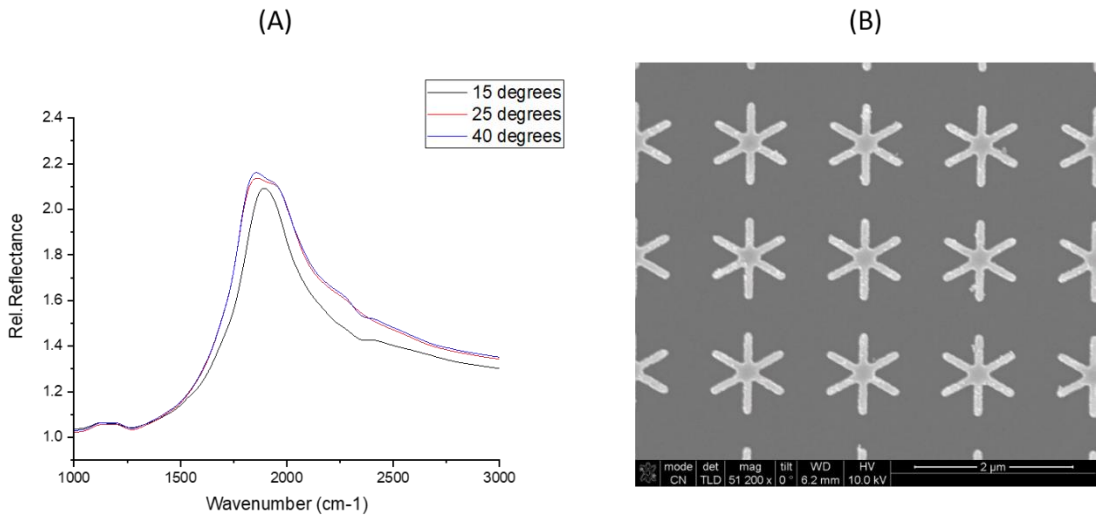

Figure S13. (a) Spectra collected from achiral cross at 15, 25 and 40°, which show qualitatively similar behavior to the Shuriken. (b) SEM image of the achiral cross.

Angle dependency of 0.75 and 2 μm Shuriken

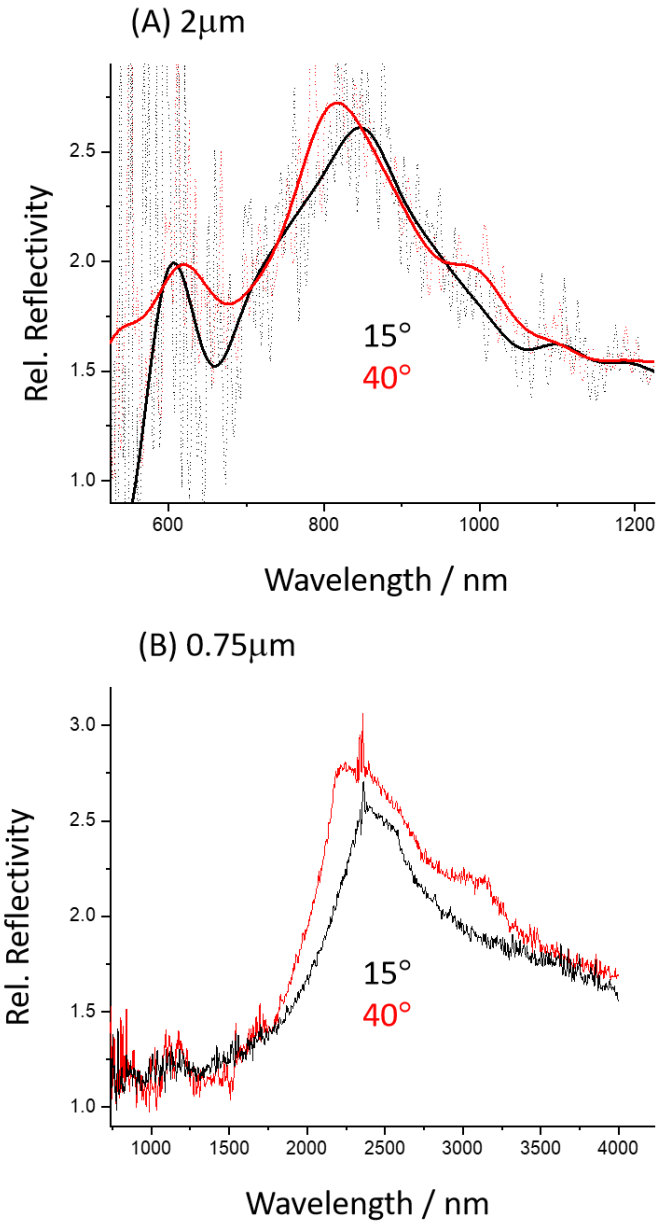

Figure S14. (a) Spectra for 2 μm LH shuriken, collected at 15° (Black) and 40° (Red) angle of incidence, raw (single spectrum not average of 6 as is the case in figure 4s) and smoothed are dotted and solid lines respectively. (a) Spectra for 0.75 μm LH shuriken, collected at 15° (Black) and 40° (Red) angle of incidence. Both structures show the development of a shoulder at higher wavenumber.